

INFORMATION TO USERS

This manuscript has been reproduced from the microfilm master. UMI films the text directly from the original or copy submitted. Thus, some thesis and dissertation copies are in typewriter face, while others may be from any type of computer printer.

The quality of this reproduction is dependent upon the quality of the copy submitted. Broken or indistinct print, colored or poor quality illustrations and photographs, print bleedthrough, substandard margins, and improper alignment can adversely affect reproduction.

In the unlikely event that the author did not send UMI a complete manuscript and there are missing pages, these will be noted. Also, if unauthorized copyright material had to be removed, a note will indicate the deletion.

Oversize materials (e.g., maps, drawings, charts) are reproduced by sectioning the original, beginning at the upper left-hand corner and continuing from left to right in equal sections with small overlaps.

Photographs included in the original manuscript have been reproduced xerographically in this copy. Higher quality 6" x 9" black and white photographic prints are available for any photographs or illustrations appearing in this copy for an additional charge. Contact UMI directly to order.

ProQuest Information and Learning
300 North Zeeb Road, Ann Arbor, MI 48106-1346 USA
800-521-0600

UMI[®]

University of Alberta

**Development of 3D Magnetic Resonance Angiography for
the Detection of Vascular Pathology**

by

Osama Al-Kwif



A thesis submitted to the Faculty of Graduate Studies and Research in partial fulfillment
of the requirements for the degree of MASTER OF SCIENCE
in
MEDICAL SCIENCES - BIOMEDICAL ENGINEERING

Edmonton, Alberta

Spring 2001



**National Library
of Canada**

**Acquisitions and
Bibliographic Services**

**395 Wellington Street
Ottawa ON K1A 0N4
Canada**

**Bibliothèque nationale
du Canada**

**Acquisitions et
services bibliographiques**

**395, rue Wellington
Ottawa ON K1A 0N4
Canada**

Your file Votre référence

Our file Notre référence

The author has granted a non-exclusive licence allowing the National Library of Canada to reproduce, loan, distribute or sell copies of this thesis in microform, paper or electronic formats.

The author retains ownership of the copyright in this thesis. Neither the thesis nor substantial extracts from it may be printed or otherwise reproduced without the author's permission.

L'auteur a accordé une licence non exclusive permettant à la Bibliothèque nationale du Canada de reproduire, prêter, distribuer ou vendre des copies de cette thèse sous la forme de microfiche/film, de reproduction sur papier ou sur format électronique.

L'auteur conserve la propriété du droit d'auteur qui protège cette thèse. Ni la thèse ni des extraits substantiels de celle-ci ne doivent être imprimés ou autrement reproduits sans son autorisation.

0-612-60407-1

Canada

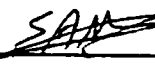
University of Alberta

Library Release Form

Name of Author: Osama Al-Kwif
Title of Thesis: Development of 3D Magnetic Resonance Angiography for the Detection of Vascular Pathology
Degree: Master of Science
Year this Degree Granted: Spring 2001

Permission is hereby granted to the University of Alberta Library to reproduce single copies of this thesis and lend or sell such copies for private, scholarly, or scientific research purposes only.

The author reserves all other publication and other rights in association with the copyright in the thesis, and except as hereinbefore provided, neither the thesis nor any substantial portion may be printed or otherwise reproduced in any material from whatever without the author's prior written permission.



Osama Al-Kwif

Box 60238 Univ. of Alberta


Edmonton, AB T6G 2S5

Date: Oct 23, 2006

University of Alberta

Faculty of Graduate Studies and Research


The undersigned certify that they have read, and recommend to the Faculty of Graduate Studies and Research for acceptance, a thesis entitled **Development of 3D Magnetic Resonance Angiography for the Detection of Vascular Pathology** by **Osama Al-Kwafi** in partial fulfillment of the requirement for the degree of **Master of Science in Medical Sciences - Biomedical Engineering**.



Dr. Alan Wilman (Supervisor)



Dr. Richard E. Snyder



Dr. Ashfaq Shuaib

Date: *Oct. 23rd, 2000*

ABSTRACT

The objective of this thesis was to develop time-of-flight (TOF) and contrast enhanced magnetic resonance angiography (MRA) at a three Tesla field strength. Prior to this work, MRA was not available on the 3T scanner. All techniques were developed from scratch. During this work different advanced techniques that already exist in the literature were adopted to optimize the performance of the pulse sequences at 3T. Flow phantom and in-vivo experiments in volunteers are presented to support the importance of each technique used.

In-vivo TOF MRA results at different field strengths, 1.5 and 3T, are presented to study the effect of increasing the field strength on the blood signal and on the blood-to-background contrast. These studies were performed under the same conditions and demonstrated the high impact of field strength on image quality in TOF MRA.

Contrast enhanced 3D MRA with its ability to obtain high resolution images with a short acquisition time was also developed. A comparison among different phase encoding methods is introduced for sampling k -space, and an experimental contrast curve is designed to study the effectiveness of these methods on image quality when a contrast agent is used. A computer simulation under the same conditions was used to support the experimental results.

The advantages of using contrast agent over the other MRA techniques were explained, and T1 measurements were performed on the same sample at 1.5 and 3T field strengths to study the variations in contrast-enhanced T1 times with field strength. Lastly, a triggering mechanism for a 3D contrast-enhanced sequence with centric phase encoding was fully developed and tested on the flow phantom.

ACKNOWLEDGEMENT

First and foremost I would like to acknowledge the efforts of my supervisor, Dr Alan Willman, whose scientific experience and guidance has made my years in Biomedical Engineering worthwhile. His sincere help and encouragement enabled me to accomplish this work with strong confidence. I greatly appreciate the investment of time by my supervisory committee members and their valuable feedback, Dr. Richard Snyder and Dr. Ashfaq Shuaib.

The staff at the NMR facility deserves great praise. Dr. Chris Hanstock, and Dan Gheorghiu, who overcame all the technical difficulties. Also a special thanks to my soccer team members and the permanent volunteers in our facility: Atiyah, Nick, Jim, Kim, Steve, and Keith.

Most importantly, I must thank my parents, Mohammad and Thana, who have supported me in every aspect of my life. I also appreciate the support from my brothers Ammar, Imad and sisters, Mouna, Hanan. Finally, I have to praise the patience and support of my wife Rana, who let me go at night to keep working on my research. Her faith in me, helped me overcome all the challenges over these years.

TABLE OF CONTENTS

	Page
Chapter 1: Introduction and Background	
1.1 Introduction	1
1.2 Fundamentals of Nuclear Magnetic Resonance	2
1.2.1 Quantum Mechanical Description of NMR	2
1.2.2 Classical Mechanical Description of NMR	5
1.2.3 Spin Relaxation Times and Bloch Equation	11
1.2.3.1 Longitudinal Relaxation T1 (Spin-Lattice)	12
1.2.3.2 Transverse Relaxation T2 (Spin-Spin)	14
1.3 Spatial Encoding	15
1.3.1 Slice Selection	16
1.3.2 Frequency Encoding	17
1.3.3 Phase Encoding	19
1.3.4 RF Excitation Pulses	21
1.4 Imaging Principles	23
1.4.1 2D Fourier Transform Sequence	24
1.4.2 Sampling Requirements in 2DFT Imaging	26
1.4.2.1 Field of View	26
1.4.2.2 Spatial Resolution	28
1.5 References	30
 Chapter 2: Time of Flight Angiography	
2.1 Introduction	32
2.2 Time of Flight (TOF)	33
2.3 Pulse Sequence Design	35
2.3.1 Design of 2D Time of Flight	36
2.3.1.1 Flow Compensation	38
2.3.1.2 Maximum Intensity Projection	42
2.3.2 Design of 3D Time of Flight	43
2.3.2.1 Ramp Pulse	46
2.3.2.2 Saturation Pulse	48
2.3.2.3 Multiple Overlapping Thin-Slab Acquisition	51
2.4 Comparing 2D with 3D TOF	53
2.5 Improving 3D TOF Images	55
2.5.1 Increasing the Spatial Resolution	55
2.5.2 Optimizing the Flip Angle	57
2.5.3 Adjusting TE to Produce Water/Fat Out-of-Phase	58
2.6 Comparing 1.5T with 3T using 3D TOF	59

2.6.1	3D TOF Experimental Protocol	61
2.6.2	Experimental Results for 1.5T vs. 3T	63
2.7	Conclusion	70
2.8	References	71

Chapter 3: Experimental Contrast Curve Design for Testing Different Acquisition Techniques in 3D CE MRA

3.1	Introduction	75
3.2	Data Acquisition Techniques	76
3.2.1	Sequential Encoding Technique	78
3.2.2	Centric Encoding Technique	79
3.2.3	Elliptical Centric Encoding Technique	80
3.2.4	Elliptical Sequential Encoding Technique	82
3.3	Experimental Comparison among Different Data Acquisition Techniques	83
3.3.1	Experimental Contrast Curve Design	85
3.3.2	Comparison Results	88
3.4	Conclusion	93
3.5	References	94

Chapter 4: 3D Contrast Enhanced MRA

4.1	Introduction	96
4.2	Effect of Reducing T1 via Contrast Agent	98
4.3	Measurement of T1 Reduction by Contrast Agent at 1.5 and 3T	100
4.3.1	Pulse Sequence Design	100
4.3.2	Experiments and Results	103
4.4	3D Contrast Enhanced MRA Pulse Sequence	108
4.4.1	Timing the Contrast Agent Arrival (Test Bolus)	110
4.4.2	3D CE Experimental Protocol	112
4.5	Conclusion	117
4.6	References	118

Chapter 5: Conclusion

5.1	Conclusion	121
5.2	Future Directions	123

LIST OF TABLES

Page

CHAPTER 1:

1-1	Representative value of relaxation time T1 and T2 in milliseconds for hydrogen components of different human body tissues at $B_0 = 1.5T$	13
-----	--	----

CHAPTER 2:

2-1	Representing the dephasing phenomenon due to a spread of velocities across a voxel	39
2-2	The signal measurement for comparing both 2D and 3D TOF images at the same field strength	54
2-3	Representative values of relaxation time T1 at 1.5 and 3T	59
2-4	The signal measurement for comparing 3D TOF images at different field strength (1.5 without MT and 3T)	63
2-5	The signal measurement for comparing 3D TOF images at different field strength (1.5 with MT and 3T)	64
2-6	The average measurements to SNR, C, and CNR from seven volunteers	64

CHAPTER 4:

4-1	The experimental T1 values for different Gadolinium concentrations at different field strength (1.5 and 3T)	105
4-2	Representative values of relaxation time T1 at 1.5 and 3T	106

LIST OF FIGURES

Page

CHAPTER 1:

1-1	Splitting of energy levels in an external magnetic field	3
1-2	A vector mode representation of protons in the presence of magnetic field	6
1-3	Clockwise precession of a proton's spin about the magnetic field B_0	7
1-4	Precession of the magnetization around the rotating reference frame	9
1-5	Precession of the magnetization about B_1 after applying a 90° pulse	9
1-6	Inducing electromotive force by rotating $M_{xy}(t)$ in the RF coil	11
1-7	Longitudinal magnetization regrowth after 90° and 180° RF pulses	13
1-8	M_{xy} as a function of time immediately after 90° pulse	15
1-9	Applying linear gradient field G_z with RF pulse to select one slice	17
1-10	Applying linear gradient field G_x to encode the signal in x direction	18
1-11	Applying linear gradient field G_y to encode the signal in y direction	20
1-12	Selective and hard pulse with the corresponding frequency domain	21
1-13	The FWHM of a theoretical slice profile generated from a sinc pulse	22
1-14	2D Fourier transform sequence with k -space trajectory	24
1-15	Sampling in k -space with the corresponding replications in object domain	26
1-16	Timing and amplitude parameters for phase and readout gradients	27

CHAPTER 2:

2-1	Imaging slice is experiencing many RF pulses during data acquisition	34
2-2	Blood signal as a function of RF pulses to reach the steady state	35
2-3	2D gradient echo sequence diagram with necessary timing and gradients	37
2-4	Four-lobe truncated sinc pulse to make the TE as short as possible	37
2-5	Constant velocity compensation gradient waveform in read direction	40
2-6	2D gradient echo with flow compensation gradients in x and z directions	40
2-7	2D TOF images with and without flow compensation	41
2-8	2D TOF with low and high resolution to improve vessels visibility	42
2-9	Obtaining a projection image by applying maximum intensity projection	43
2-10	3D TOF with flow compensation and saturation pulse	44
2-11	Both real and imaginary parts of the ramp pulse and its FFT	46
2-12	Ramp pulse flip angle distribution through the imaging volume	47
2-13	Test ramp pulse in-vivo with different orientations	48
2-14	A schematic of 90° saturation pulse to saturate the signal from veins	49
2-15	Applying 3D TOF with saturation pulse on the flow phantom	49
2-16	3D TOF with and without saturation pulse on a human neck	50
2-17	Combining two 3D slabs for Circle of Willis using MOTSA technique	52
2-18	Combining four 3D slabs for Circle of Willis and vertebral artery	52
2-19	Comparing 2D with 3D TOF for Circle of Willis for the same volunteer	53
2-20	Coronal view for Circle of Willis in 2D and 3D TOF for the same volunteer	54

2-21	Test the effect of increasing spatial resolution on the resolution phantom	55
2-22	MIP in-vivo images of 3D TOF with different spatial resolution	56
2-23	MIP in-vivo images of 3D TOF with different flip angles	57
2-24	The source images for the eyes with different TE to remove the fat signal	58
2-25	A theoretical plot for blood and background signals at 1.5 and 3T	60
2-26	The contrast difference between 1.5 and 3T for both gray and white matter	61
2-27	2D scout image to determine the ROI for the 3D TOF	62
2-28	Comparing coronal and sagittal views for Circle of Willis at 1.5 and 3T	65
2-29	Comparing MIP images for Circle of Willis at 1.5 with 3T TOF, case # 2	66
2-30	The images at 1.5 and 3T to show the effect of background suppression	67
2-31	Comparing MIP images for Circle of Willis at 1.5 with 3T TOF, case # 7	68
2-32	The images at 1.5 and 3T to show the effect of background suppression	69

CHAPTER 3:

3-1	The effect of inverse fast Fourier transform on image quality when different centric parts from k -space are chosen	77
3-2	Sequential phase encoding diagram	78
3-3	Centric phase encoding diagram	79
3-4	Elliptical phase encoding diagram	80
3-5	Elliptical centric encoding where we start from the center of k -space	81
3-6	Saving the gradient values in the waveform editor to implement the	82

	elliptical encoding, where each peak represents a certain gradient value	
3-7	Elliptical sequential phase encoding diagram	83
3-8	Producing high signal from the first pass of the contrast agent	84
3-9	Changing the transverse magnetization by applying different flip angles	86
3-10	The relationship between the longitudinal and transverse magnetization	87
3-11	Experimental and theoretical contrast curve	88
3-12	The theoretical and experimental effects of varying start time of data acquisition on signal intensity	90
3-13	Theoretical and experimental images of the simulated artery and vein corresponding to a start time at the arterial peak	91
3-14	Theoretical and experimental images of the simulated artery and vein corresponding to a poor start time of -18.5% before the arterial peak	92
3-15	Illustration of the effects of varying venous return time on the AV contrast	93

CHAPTER 4:

4-1	Theoretic relative signal amplitude of tissues with different T1 values	98
4-2	Theoretic MR signal at steady state as a function of the flip angle	99
4-3	Theoretic MR signal at steady state as a function of repetition time with different T1 values	100
4-4	The 2D GE inversion recovery pulse sequence to measure T1	101
4-5	The magnitude of the signal as a function of TI	102

4-6	The sample used to measure T1 values for Gd	103
4-7	Graphical plot for the experimental T1 values from table 4-1	104
4-8	The source images of the used sample acquired by 2D GE inversion recovery pulse sequence at different TI intervals	105
4-9	A theoretic plot for blood and background signal at the first pass of the contrast agent at both field strengths	107
4-10	The contrast difference between 1.5 and 3T for both fat and muscle	107
4-11	3D CE MRA sequence with short TE 2.2ms and TR 6.5ms	109
4-12	Producing high signal from the first pass of the contrast agent	110
4-13	Test bolus trail to measure the correct timing of the contrast agent arrival	112
4-14	Simulating the blood vessels through the flow phantom	114
4-15	Test bolus on the flow phantom to determine the correct timing for the Gd arrival into the ROI	115
4-16	Scout image for the neck for accurate determination of the ROI	116

ABBREVIATIONS

AV	<u>A</u> rtery-to- <u>V</u> ein Contrast
BW	Bandwidth
CE	Contrast Enhanced
CNR	<u>C</u> ontrast to <u>N</u> oise <u>R</u> atio
EMF	Electromotive Force
EPI	Echo Planner Imaging
FA	Flip Angle
FOV	Field Of View
FT	Fourier Transform
FWHM	Full Width Half Maximum
Gad	Gadolinium
GE	Gradient Echo
IR	Inversion Recovery
MCA	Middle Cerebral Artery
MIP	Maximum Intensity Projection
MOTSA	Multiple Overlapping Thin-Slab Acquisition
MRA	Magnetic Resonance Angiography
MRI	Magnetic Resonance Imaging
MT	Magnetization Transfer
NMR	Nuclear Magnetic Resonance
PC	Phase Contrast

Res	Resolution
RF	Radio Frequency
ROI	Region Of Interest
SE	Spin Echo
SNR	<u>S</u> ignal to <u>N</u> oise <u>R</u> atio
TE	Echo Time
TOF	Time Of Flight
TR	Repetition Time
2D	Two Dimensional
3D	Three Dimensional

SYMBOLS

B_0	external magnetic field
B_1	radio frequency magnetic field
BW_{rec}	receiver bandwidth
E	potential energy of the spin
FOV_{PE}	field of view in the phase direction
FOV_R	field of view in the read direction
G_x	readout gradient
G_y	phase encoding gradient
G_{y-inc}	phase encoding gradient increment
G_z	slice select gradient
I	spin angular momentum
k	Boltzman's constant
M_0	net magnetization vector
M_{xy}	transverse magnetization
M_z	longitudinal magnetization
N_{acq}	number of acquisitions
N_{PE}	number of phase encoding steps (y direction)
N_R	number of acquired samples
N_x	number of samples in x direction

N_y	number of samples (views) in y direction
N_z	number of phase encoding steps in z direction
T	absolute temperature
T_1	longitudinal relaxation time (spin-lattice)
T_2	transverse relaxation time (spin-spin)
T_{acq}	acquisition time
TI	inversion time
TH	slice thickness
T_{sat}	delay time after the saturation pulse
v_x	constant velocity of spins
x_0	initial position of spins
$\Delta\omega$	frequency bandwidth
Δy	spatial resolution in y direction
Δx	spatial resolution in x direction
$\Delta k_{(x,y)}$	sampling period in k -space
Δt	sampling intervals
τ_x	frequency encoding time
τ_y	phase encoding time
α	flip angle
ω_N	Nyquist frequency
ϕ	phase
\hbar	Planck constant divided by 2π

μ_x	x component of magnetic moment
μ_y	y component of magnetic moment
μ_z	z component of magnetic moment
μ	magnetic dipole moment
γ	proton gyromagnetic ratio
ω_0	Larmor frequency (resonance frequency)

CHAPTER 1

Introduction and Background

1.1. Introduction:

During the last two decades, magnetic resonance imaging (MRI) has developed into a major diagnostic modality with applications that cover every part of the human body. The MRI process is based on a sophisticated process with many variable parameters that must be taken into account for each clinical application in order to get the optimal results. For each application, turning MRI into a powerful clinical tool requires knowledge of its physical principles, as well as imaging methods and techniques.

This chapter is intended as a brief overview of topics necessary for the understanding of this thesis. A review of nuclear magnetic resonance (NMR) and MRI fundamentals important to high speed imaging is presented. Since the overall goal of this work is to develop different pulse sequences for magnetic resonance angiography (MRA), the main focus is on MR signal encoding and the parameters that affect the MR signal.

In later chapters the applications of the developed pulse sequences and different acquisition techniques are fully presented with various examples from phantoms or in-vivo to support this thesis work.

1.2. Fundamentals of Nuclear Magnetic Resonance:

The fundamentals of nuclear magnetic resonance theory are presented in this section in order to provide a brief overview of topics necessary for the understanding of this thesis. A more complete description related to these topics can be found in these references [1-3]. Fundamental concepts are presented from both quantum mechanical and classical mechanical descriptions [2].

1.2.1. Quantum Mechanical Description of NMR:

The proton possesses a spin angular momentum \mathbf{I} within an atomic nucleus and an associated magnetic dipole moment μ . The direct relationship between the magnetic dipole moment and the spin angular momentum vector is:

$$\mu = \gamma \hbar \mathbf{I} \quad (1-1)$$

where \hbar is the Planck constant divided by 2π ($\hbar = 1.054 \times 10^{-34}$ J.s) and γ is a constant called the gyromagnetic ratio (for Hydrogen, $\gamma = 2.68 \times 10^8$ rad/s/T or 4257 Hz/Gauss).

The unpaired proton of hydrogen ^1H gives rise to a net magnetic moment of the nucleus, making it suitable for NMR. Other nuclei that also have magnetic moments suitable for NMR include ^{31}P , ^{23}Na , ^1H , and ^{13}C . However, only the hydrogen nuclei (protons) are present in biological material with a concentration high enough to enable imaging techniques with high spatial resolution [3].

The potential energy of the spin angular momentum is the dot product of the magnetic moment with the external magnetic field:

$$E = -\boldsymbol{\mu} \cdot \mathbf{B}_0 \quad (1-2)$$

The static magnetic field makes protons in the tissue polarized so that they are aligned parallel or anti-parallel to \mathbf{B}_0 , spin-up or spin-down as shown in Fig. 1-1. This distribution is a result of a nonzero interaction between the spins and \mathbf{B}_0 , called the *Zeeman interaction*, which produces a difference in energy levels between protons aligned parallel or anti-parallel to \mathbf{B}_0 . The uncertainty principle indicates that only one component of the angular momentum can be determined, which aligns along the external magnetic field I_z [4].

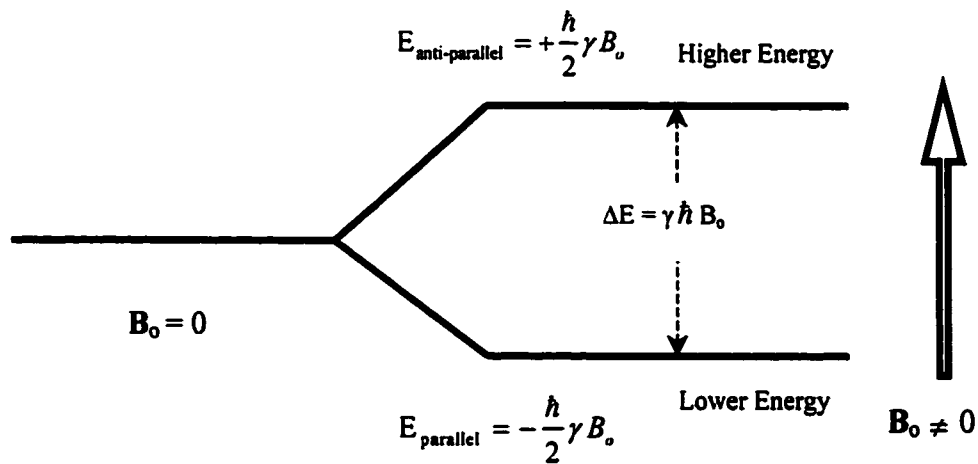


Figure 1-1 Splitting of energy levels in an external magnetic field. In one energy level the spin is parallel to \mathbf{B}_0 , and in the other, the spin is anti-parallel to \mathbf{B}_0 .

This component along the magnetic field is quantized as half integer multiples of \hbar , thus $I = +1/2$ or $-1/2$ for a single proton as given in Eq. (1-1). This difference in energy levels of the separated spin angular momentum, ΔE , is proportional to B_0 as shown in Fig. 1-1. The number of protons in each energy level is controlled by a special distribution known as the *Boltzmann distribution* [5] that can be expressed by:

$$N_{\text{upper}} - N_{\text{lower}} = e^{-\Delta E/kT} \quad (1-3)$$

where N_{upper} and N_{lower} represent the number of protons in the upper and lower energy levels, respectively. T is the absolute temperature in Kelvin (K), and k is Boltzmann's constant 1.38×10^{-23} J/K.

At room temperature, using $B_0 = 3$ T, the difference in proton spins in both energy levels is approximately 20 part per million. It is this small difference that produces the observed NMR signal. A transition from the parallel to anti-parallel energy level can be best achieved by applying energy at a frequency equivalent to:

$$\Delta E = \gamma \hbar B_0 = \hbar \omega_0 \quad (1-4)$$

This equation shows that the frequency of the energy required to cause a spin transition between the energy levels is directly proportional to the applied magnetic field. At $B_0 = 3$ T, this frequency is equal to 127 MHz and is known as the Larmor frequency or resonant frequency, ω_0 . This energy can be applied through a radio-frequency

transmission coil, to move the spins from the parallel to anti-parallel level. Removing the applied radio frequency (RF) energy will allow return of the spins to the equilibrium level, producing small amounts of energy that can be detected with an RF receiver coil. This received signal is the MR signal, which carries the information about the sample.

1.2.2. Classical Mechanical Description of NMR:

If we consider an arbitrary sample volume containing protons located within a magnetic field $B_0 = 0$, we find that each proton has a magnetic moment of equal magnitude. However, the magnetic moment for the entire collection of protons within the tissue are randomly oriented in all directions at thermal equilibrium, producing a vector addition equal to zero [6].

Now, if we placed this sample inside a non zero magnetic field B_0 , the protons start polarizing so that they are aligned parallel or anti-parallel to the B_0 as shown in Fig. 1-2. The net magnetization vector is defined as the sum of all magnetic moments over the sample volume:

$$M_0 = \sum_{\text{volume}} \mu_i \quad (1-5)$$

This magnetization has the same orientation as B_0 , and the greater the field strength B_0 , the greater the value of M_0 and the greater the received MR signal.

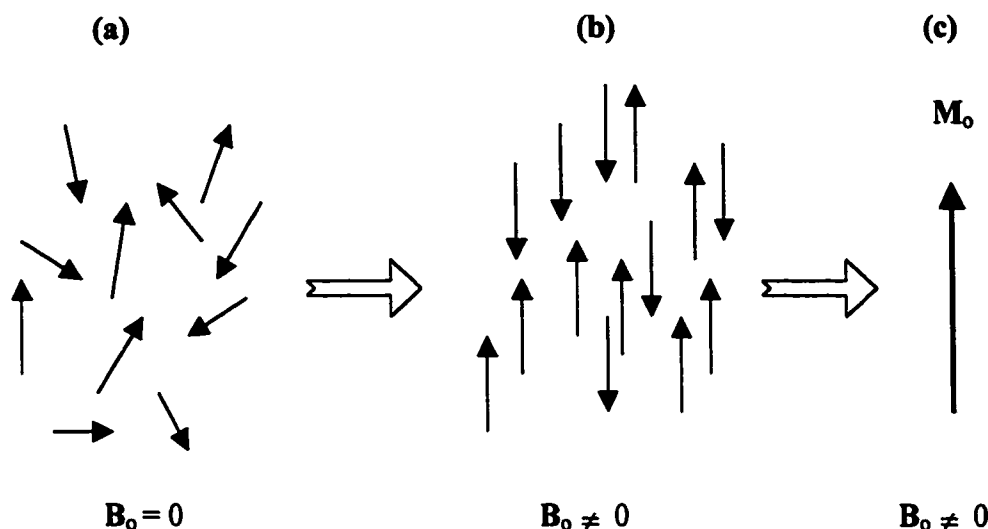


Figure 1-2 (a) Collection of protons in the absence of an external magnetic field, where the magnetic moments are oriented randomly. (b) Inside an external magnetic field, where the magnetic moments align parallel or anti-parallel. (c) The net magnetization vector.

The equation of motion of a magnetic moment vector μ in a magnetic field B_0 can be obtained by equating the torque $\mu \times B_0$ to the rate of change of angular momentum. And because the nuclear magnetic moment is related to the spin angular momentum as in Eq. (1-1), we can write:

$$\frac{d\mu}{dt} = \gamma \mu \times B_0 \quad (1-6)$$

This equation is a simple version of the Bloch equation to be described later. Even though the magnetic moment has a fixed magnitude, its direction is changing, which is equivalent to a left-handed rotation about B_0 , the other vector in the cross product as shown in Fig. 1-3.

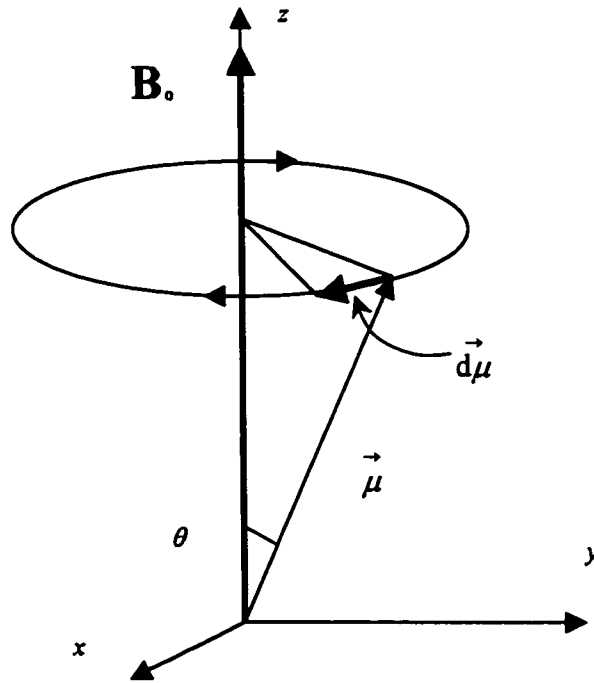


Figure 1-3 Clockwise precession of a proton's spin about the magnetic field B_0 .

The equation of motion can be decomposed using a Cartesian coordinate system; the final solutions describe the magnetic moment precession about the external field B_0 along the z direction. The following equations explain the trajectory of motion for μ [2] [7]:

$$\mu_z(t) = \mu_z(0) \quad (1-7a)$$

$$\mu_x(t) = \mu_x(0) \cos(\omega_0 t) + \mu_y(0) \sin(\omega_0 t) \quad (1-7b)$$

$$\mu_y(t) = \mu_y(0) \cos(\omega_0 t) + \mu_x(0) \sin(\omega_0 t) \quad (1-7c)$$

where μ_z , μ_x , and μ_y are the z , x , and y components respectively.

At equilibrium, the magnetic moment vectors $\vec{\mu}$ will have a random phase, therefore the transverse components will cancel and the resulting magnetization vector \mathbf{M}_0 is aligned with the applied external field. Note that the motion about the external field at a frequency ω_0 is the same resonance frequency mentioned in the previous section, which caused a transition from the lower energy level to the upper energy level using the quantum mechanical model.

The precessional motion becomes more sophisticated when energy absorption is considered (will be explained in the next section). Therefore, a useful technique is included to simplify the description which is known as the *rotating frame of reference*, or rotating coordinate system [4], in which the coordinate system rotates around one axis while the other two axes vary with time. By selecting a suitable axis and rotation rate for the coordinate system, the moving spins will appear stationary.

In the MR experiments we choose the z axis parallel to \mathbf{B}_0 , as the rotation axis and let the x and y axes rotate at the Larmor frequency, ω_0 . In this case it is easy to visualize the precessing protons, where they appear stationary in space with a fixed coordinate system x , y and z as shown in Fig. 1-4.

Since \mathbf{M}_0 is not measurable, we use a special technique to produce detectable magnetization in the sample [8], which can be achieved by applying a second magnetic field \mathbf{B}_1 rotating in the x - y plane at the same frequency, perpendicular to \mathbf{B}_0 as shown in Fig. 1-5.

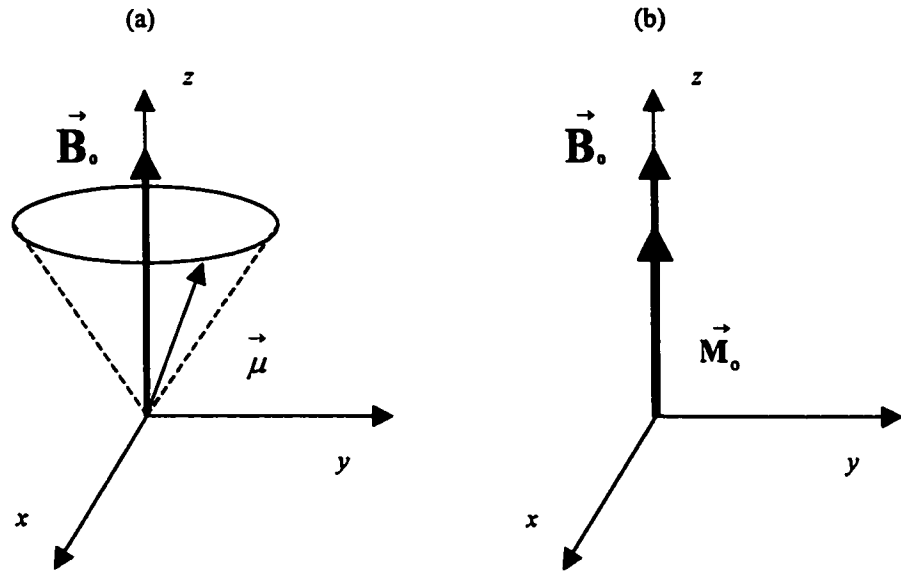


Figure 1-4 (a) In the stationary reference frame the precession of a magnetization vector around the z axis. (b) This precession appears as a stationary vector in the rotating reference frame.

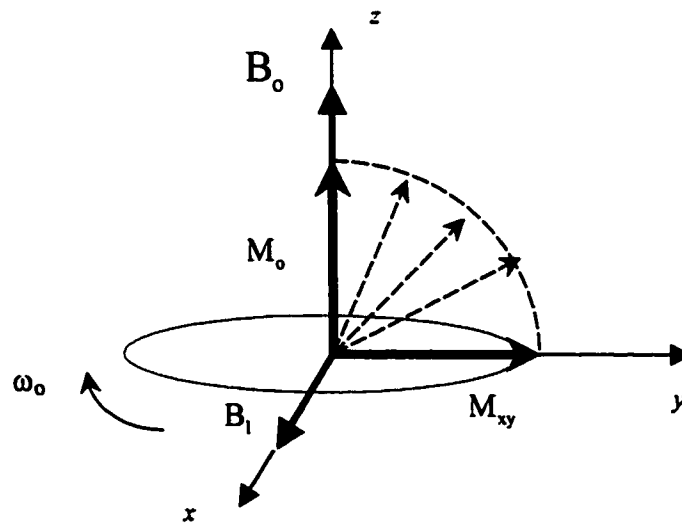


Figure 1-5 Precession of the magnetization vector about the applied field B_1 after applying a 90° pulse to produce the transverse magnetization, a measurable quantity, as viewed in the rotating reference frame.

The process of applying a pulse of B_1 is called RF excitation, making use of a special RF coil. The interaction effect of M_0 , longitudinal magnetization, with B_1 is to flip M_0 away from the z axis to produce nonzero x and y components, M_x and M_y . The magnetization in the x - y plane that results from RF excitation is called the transverse magnetization and is represented by a single complex value M_{xy} :

$$M_{xy} = M_x + i M_y \quad (1-8)$$

where $i = \sqrt{-1}$.

The interaction of M_0 with B_1 is analogous to the interaction of μ with B_0 . The flip angle, α , which is known as the excitation flip angle (FA), depends on the magnitude of B_1 and the duration of the pulse t as:

$$\alpha(t) = \gamma \int_0^t B_1(t) dt \quad (1-9)$$

Choosing this flip angle is dependent on the particular imaging application, and the tissue of interest.

After excitation, the transverse magnetization M_{xy} , the quantity that can be measured, precesses around the z axis at ω_0 . By using a coil stationary in the laboratory frame and placed adjacent to the sample, we can detect the induced current at the resonance frequency as predicted by Faraday's law [4]. The resulting signal is the MR signal that carries all the useful information we are looking for, as shown in Fig. 1-6.

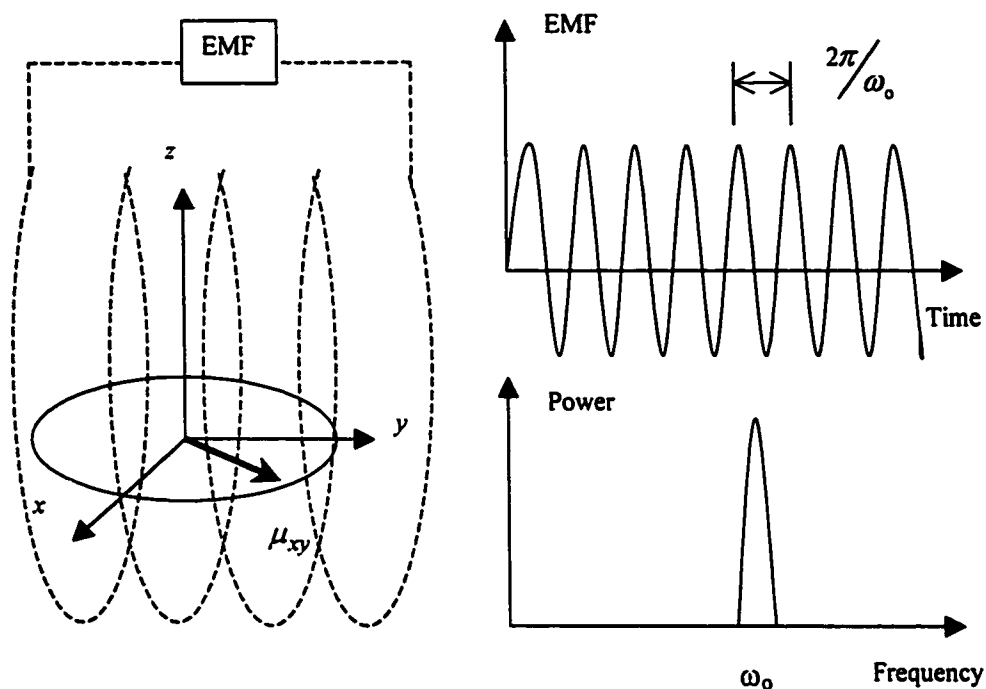


Figure 1-6 The time dependent magnetic field caused by the rotation of $M_{xy}(t)$ threads the RF coil and so induces in it an electromotive force (EMF). Applying a Fourier transform (FT) to the MR signal will give a delta function at the resonance frequency.

1.2.3. Spin Relaxation Times and Bloch Equation:

After RF excitation, the NMR signal can be measured as a function of time; however, this signal does not persist indefinitely. Relaxation effects cause the signal to decay exponentially. The relaxation process is governed by two relaxation times, longitudinal relaxation T_1 and transverse relaxation T_2 .

1.2.3.1. Longitudinal Relaxation T1 (Spin-Lattice):

It was observed independently by Bloch [9] and Purcell [10] that the rate of change of the M_z component is proportional to how far it has been tipped from the equilibrium magnetization M_0 :

$$\frac{dM_z}{dt} = \frac{1}{T1} (M_0 - M_z) \quad \left(\vec{B}_{ext} \parallel \hat{z} \right) \quad (1-10)$$

where the constant T1 is the experimental spin-lattice relaxation time or longitudinal relaxation time.

T1 depends on how fast the energy is transferred from the resonant nuclei to the surrounding molecular lattice by random thermal collisions between adjacent molecules after excitation. To measure the T1 value for various materials, the M_z magnetization must be manipulated into the x-y plane.

The following table shows typical relaxation times for various tissues. Note that the T1 of protons does in fact differ measurably from one tissue type to another, and this provides MR with one of its principal contrast mechanisms, since after the same delay following an excitation pulse, equal numbers of nuclei in different tissue types will have different signal strengths. As an example, by choosing the delay appropriately, the signal strength from one particular tissue type can be set to zero as shown in Fig. 1-7.

Tissue	T1 (ms)	T2 (ms)
Gray Matter (GM)	920	100
White Matter (WM)	790	80
Cerebrospinal fluid (CSF)	4500	2200
Fat	250	60
Blood	1200	100-200

Table 1-1 Representative values of relaxation time T1 and T2 in milliseconds for hydrogen components of different human body tissues at $B_0 = 1.5\text{T}$ and 37°C . [2].

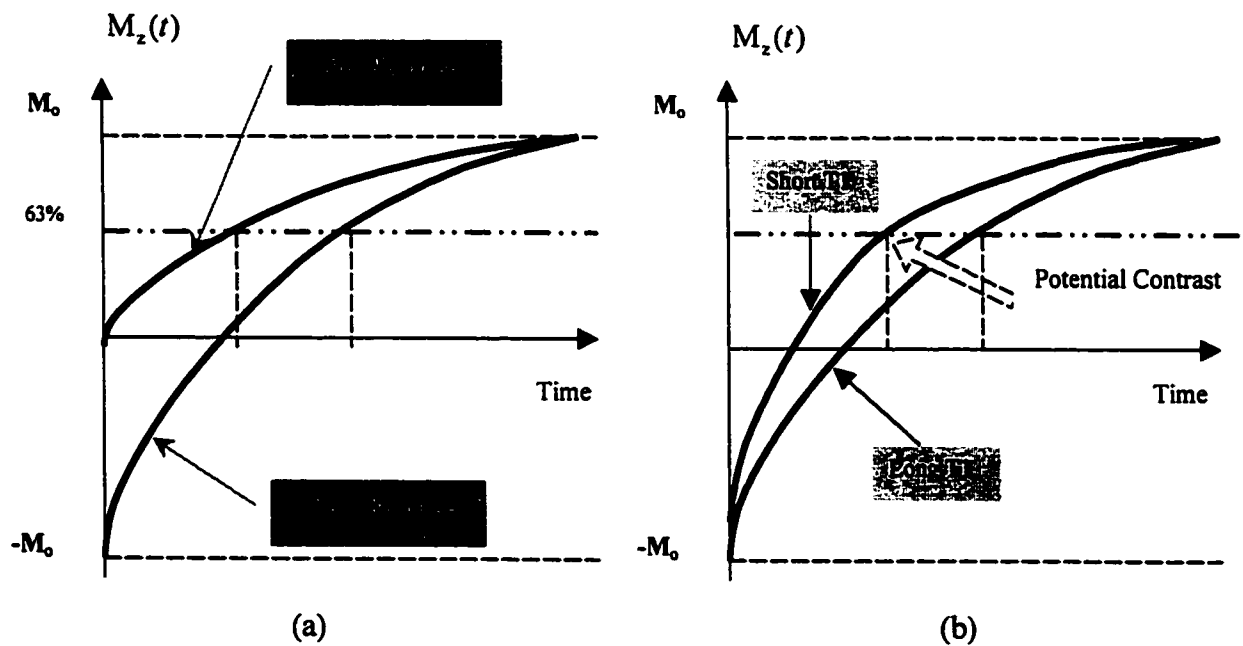


Figure 1-7 (a) The regrowth of the longitudinal magnetization after 90° and 180° RF pulses. Note that T1 is measured such that M_z will regrow to 63% of its equilibrium value M_0 . (b) Using 180° RF pulse we can produce high contrast between different tissues which have different T1 constant.

Integration of Eq. (1-10) over time will give an equation for the z magnetization component, which is the key to understanding the regrowth after an initial excitation of longitudinal magnetization:

$$M_z(t) = [M_z(0) - M_s] \exp(-t/T_1) + M_s \quad \left(\vec{B}_{ext} \parallel \hat{z} \right) \quad (1-11)$$

1.2.3.2. Transverse Relaxation T2 (Spin-Spin):

The rate of change of the x-y component of the transverse magnetization, M_{xy} , is proportional to the magnitude of the transverse magnetization M_{xy} [11]:

$$\frac{dM_{xy}}{dt} = -\frac{1}{T_2} (M_{xy}) \quad (1-12)$$

where the constant T_2 is called the transverse, or spin-spin relaxation time.

By integration of this equation over time we get the equation of decay for the x-y components of the magnetization:

$$M_{xy}(t) = M_{xy}(0) \exp(-t/T_2) \quad (1-13)$$

T_2 represents the dephasing, or loss of coherence of adjacent nuclei due to non-uniform local fields of the neighboring nuclear dipoles. Therefore, no energy is lost to the

lattice in T2 relaxation. Fig. 1-8 shows the decay of the M_{xy} magnetization after a 90° pulse which produces the MR signal.

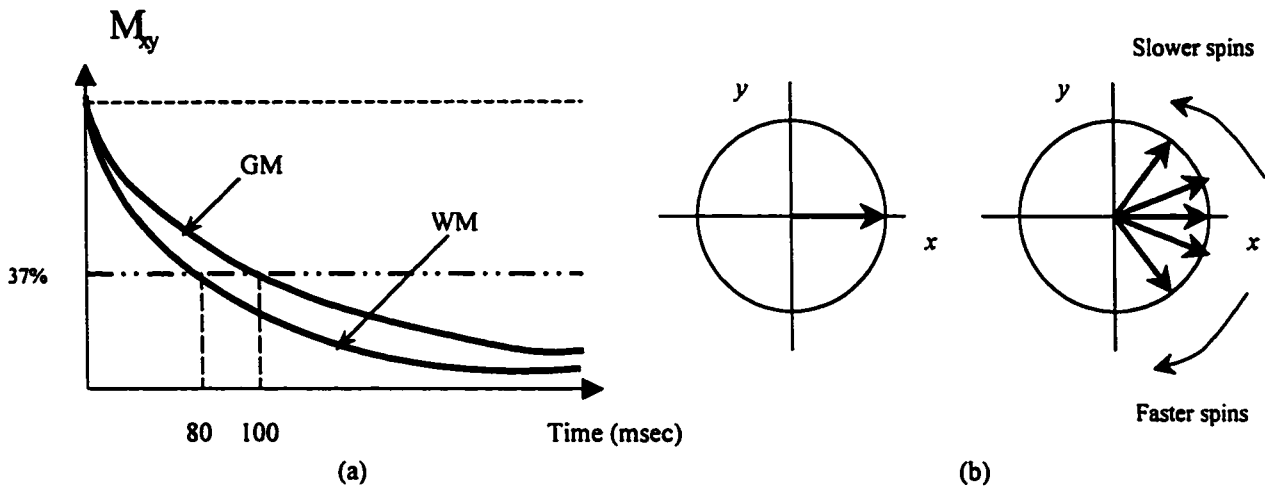


Figure 1-8 (a) M_{xy} as a function of time immediately after a 90° pulse. (b) The spins in the x-y plane start precessing at different frequencies due to experiencing different magnetic fields due to inhomogeneities, this dephasing producing an exponential decay in M_{xy} signal.

The differential equations (1-6) and (1-7) for magnetization in the presence of a magnetic field represent the Bloch equations which describe the precessional behavior. Equations (1-10) and (1-12) describe the exponential behavior of both the longitudinal and transverse components. Although precession does not change the magnitude of M_0 , T1 and T2 relaxation effects do change the magnitude of M_z and M_{xy} , respectively.

1.3. Spatial Encoding:

Localization in MRI is achieved by applying spatially dependent magnetic fields during the play out of the pulse sequence. These gradients (G) are perturbations to the main B_0 field and are much less than the B_0 field strength ($B_0 = 3T = 30000mT$, $G =$

20mT/m). Although the gradient G can vary along any direction, the magnetic field components are always aligned in the direction of the main magnetic field. Thus, at a position (r) the total magnetic field $B_{(r)}$ is:

$$|B_{(r)}| = |B_0| + G.r \quad (1-14)$$

and the resonant frequency $\omega_{(r)}$ is:

$$\omega_{(r)} = \gamma(B_0 + G.r) \quad (1-15)$$

These gradients are used to encode the information in x , y and z directions by means of slice selection, and frequency and phase encoding. The type of encoding used for a specific direction can change from sequence to sequence.

1.3.1. Slice Selection:

A slice within the sample is selected by simultaneously applying a gradient field along the slice direction and a frequency selective RF pulse with a given central resonant frequency. The presence of G_z in the slice select direction will excite spins only in a certain spatial location that matches the Larmor frequency in Eq. (1-15) [12]. The thickness of the slice is determined by the Bandwidth (BW) of the RF pulse, which is chosen based on available RF amplitude and gradient strength. More slices perpendicular to the slice select direction can be excited by applying further pulses centered about

different frequencies in the presence of the same gradient as shown in Fig. 1-9. The size of G_z determines the slice thickness through the equation:

$$\Delta\omega = \gamma G_z \Delta z \quad (1-16)$$

where $\Delta\omega$ is the frequency bandwidth of the RF pulse and Δz is the slice thickness of the slice in the slice select direction. By using fixed frequency bandwidth we can increase the slice thickness by decreasing the amplitude of G_z .

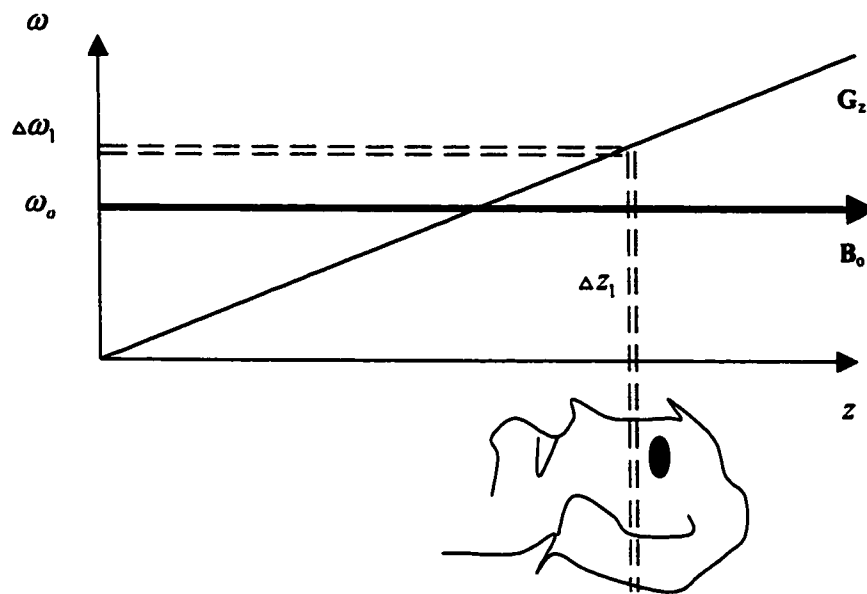


Figure 1-9 Applying linear gradient field G_z with RF pulse to select one slice from the sample; $\Delta\omega$ is the frequency bandwidth of the RF pulse.

1.3.2. Frequency Encoding:

Frequency encoding is used to encode the MR signal in one of the directions within the plane selected by the slice selection gradient. The physics of frequency encoding is similar to that used for slice selection. A gradient is applied along the

direction of interest causing the resonant frequency to vary linearly along that direction as illustrated in Eq. (1-15). The difference between the two is that no RF pulse is used for frequency encoding and data is acquired during frequency encoding.

If an x gradient G_x is applied as shown in Fig. 1-10, then we can write the relation between the bandwidth $\Delta\omega_x$ and position x as:

$$\Delta\omega_x = \omega(x_{\max}) - \omega(x_{\min}) = \gamma \{ (B_0 + G_x x_{\max}) - (B_0 + G_x x_{\min}) \} = \gamma G_x \text{FOV}_x \quad (1-17)$$

where $\Delta\omega_x$ is the bandwidth of the received signal and $\text{FOV}_x = x_{\max} - x_{\min}$ is defined as the field of view (FOV) along the x direction.

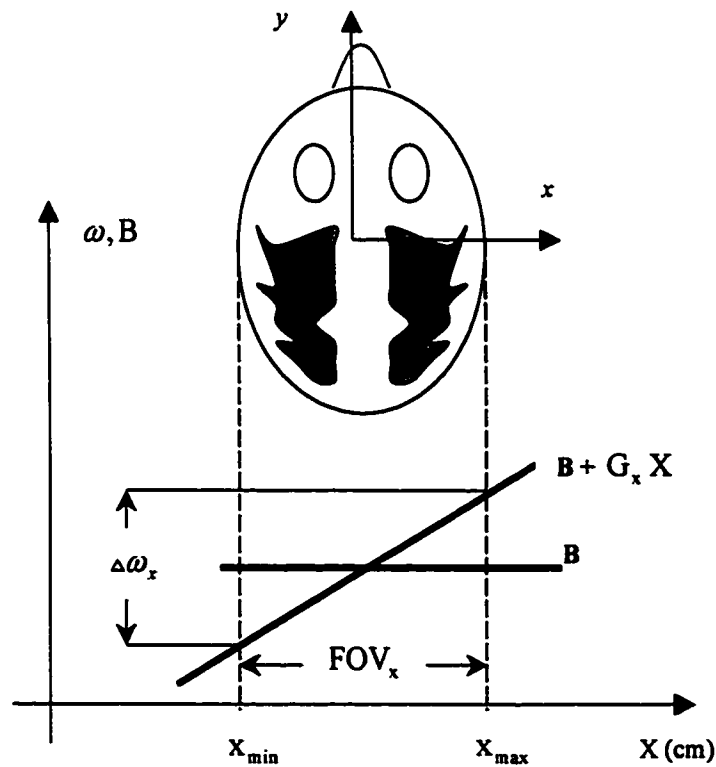


Figure 1-10 Applying linear gradient field G_x to encode the signal in the x direction.

The range of frequencies across the FOV is $\pm \Delta\omega_x/2$ thus by sampling at a rate of $\Delta\omega_x$ the Nyquist criteria is satisfied. This avoids aliasing and wrap around artifacts in the frequency encoding direction providing that the object does not extend beyond the FOV. The sampling interval between each frequency encoded point is:

$$\Delta t = \frac{1}{\Delta\omega_x} \quad (1-18)$$

The sampling interval is often further reduced by oversampling. Oversampling is used by doubling the FOV in the read direction by collecting twice as many points, doubling the receiver bandwidth (i.e. half sample period), without varying the read gradient. Doubling the FOV in the read direction will reduce aliasing artifacts without sacrificing SNR or lengthening acquisition time.

1.3.3. Phase Encoding:

The remaining direction to be encoded is the y direction using the technique of phase encoding. The phase encoding gradient G_{y-inc} is varied between successive repetitions of the sequence. Since spins at the opposite sides of the FOV have phase angles different by 2π , the necessary gradient to avoid aliasing can be calculated from:

$$2\pi = \gamma G_{y-inc} \text{FOV}_y t \quad (1-19)$$

where G_{y-inc} is the gradient value to encode one line along y direction, FOV_y is the field of view in y direction, and t is the duration of the gradient.

For a given value of G_{y-inc} the resonant frequency of spins along the phase direction is encoded. When G_{y-inc} is subsequently turned off, the spin resonant frequency returns to its previous unencoded value. The increment in resonant frequency during application of G_{y-inc} adds a phase angle to the spin vector precession in the transverse plane orthogonal to B_0 as shown in Fig. 1-11. During the next repetition of the sequence the G_{y-inc} value is stepped up such that the phase incurred upon cessation of G_{y-inc} is increased.

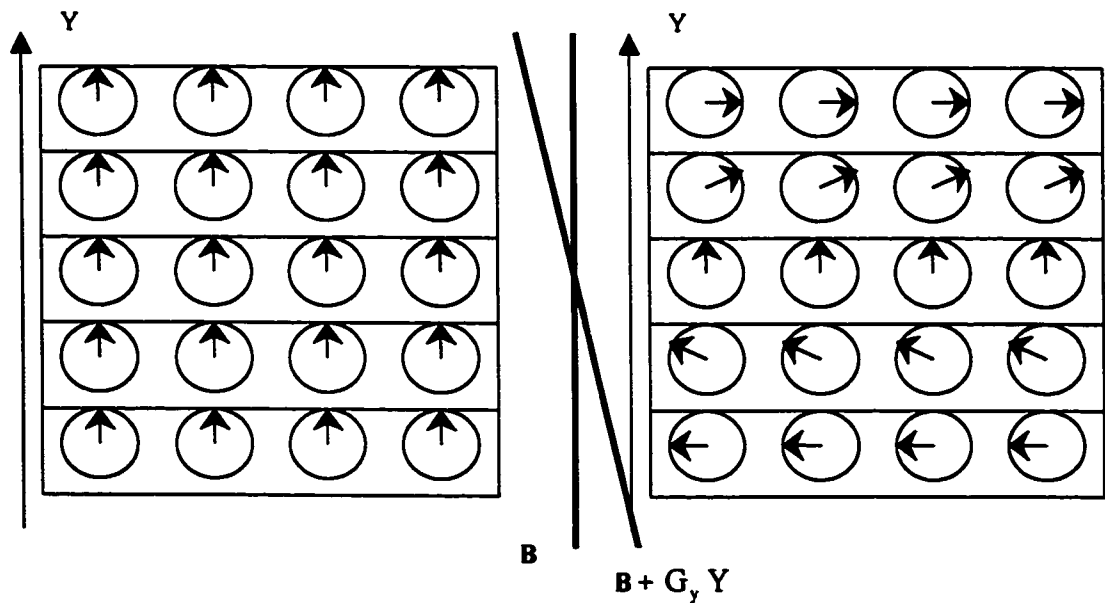


Figure 1-11 Applying linear gradient field G_y to encode the signal in y direction, note that the applied gradient produces phase angle of the spin vector.

The number of phase encoding steps used is determined by the desired spatial resolution in the phase encode direction, thus the voxel size can be reduced by increasing the number of phase encoding steps.

1.3.4. RF Excitation Pulses:

The shape of the applied RF pulse in the frequency domain is the slice profile, and can be determined for small flip angles ($<30^\circ$, small flip angle approximation [6]) by Fourier transformation to its time domain envelope. A sinc pulse will give a rectangular profile in the frequency domain with a central frequency equal to the transmitter frequency of the coil. The duration of the RF pulse will determine the bandwidth in the frequency domain as shown in Fig. 1.12. Hard pulses give rise to a broad bandwidth excitation at all frequencies. In contrast, soft pulses give rise to a narrow bandwidth, which can be selected with gradients to achieve a narrower spatial range of excitation [13]. In general, the B_1 field is applied in the shape needed to excite the desired slice during the application of the G_z gradient.

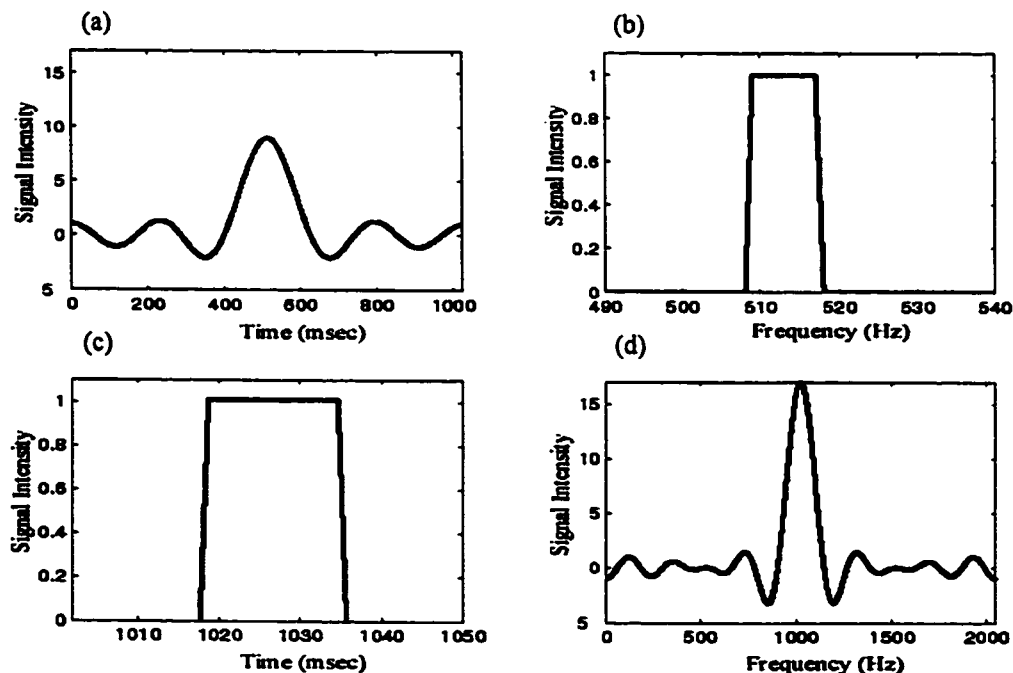


Figure 1-12 (a) A simulated soft, selective pulse (b) the corresponding narrow frequency bandwidth (c) hard, nonselective pulse (d) the corresponding broad frequency bandwidth and significant sidelobes at all frequency.

It is necessary to calibrate the effective slice created by the RF pulse, slice select gradient, and refocusing gradient which refocuses the spins in the xy plane, in order to get the correct slice thickness. By an experiment we can check the RF slice select profile when the read direction is placed along the slice select axis. In general, the full width half maximum (FWHM) of the slice profile is used to define the effective slice thickness as shown in Fig. 1-13.

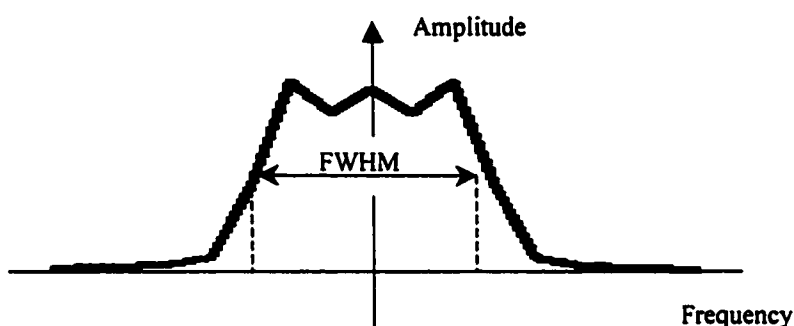


Figure 1-13 The FWHM of a theoretical slice profile generated from a sinc pulse.

In order to protect the patient from heating and to avoid hardware overheating, there is a limitation on the RF power delivered by a given RF pulse set by the maximum output of the transmitter amplifier. This imposes a restriction on both the amplitude and duration of the RF pulse used, and hence the minimum frequency bandwidth. That is critical during fast imaging, such as MRA, where very short repetition times are used.

1.4. Imaging Principles:

The ultimate goal of imaging is to determine the location of transverse magnetization from the measurement of this signal as a function of time. The first stage is to connect the spin precession to its location in the sample, as done in the previous section (Spatial Encoding, Sec. 1.3). The second stage is to recognize that this connection implies that the signal is a linear integral transform of the spin density.

The received time signal $S(t)$ is derived from the contributions of all precessing transverse magnetization in a given region of interest (ROI). Thus the sum of all the received signal $M(x, y)$ can be written as an integral:

$$S(t) = \int_x \int_y M(x, y) e^{-i2\pi[k_x(t) \cdot x + k_y(t) \cdot y]} dx dy \quad (1-20)$$

where we consider that spatial localization is required in only the x and y direction for simplicity, and k_x, k_y are the time integrals of the gradient waveforms in both directions:

$$k_x(t) = \gamma \int_0^t G_x(\tau) d\tau \quad (1-21a)$$

$$k_y(t) = \gamma \int_0^t G_y(\tau) d\tau \quad (1-21b)$$

Eq. (1-20) is called the signal equation, which can describe almost every imaging method. Note that this equation is recognized as the expression for a Fourier transform [14]. The values of k_x and k_y are positions in k -space, the space of the Fourier transform. K -space is a two or three dimensional grid with as many points as voxels assigned to the acquired object.

1.4.1. Two Dimensional (2D) Fourier Transform (FT) Sequence:

To understand the relationship between the spatial encoding gradients and k -space trajectory, let us draw the simple 2D Fourier transform sequence that contains a selective excitation pulse, slice select gradient G_z , phase encoding gradient G_y , and readout gradient G_x [11], as shown in Fig. 1-14.

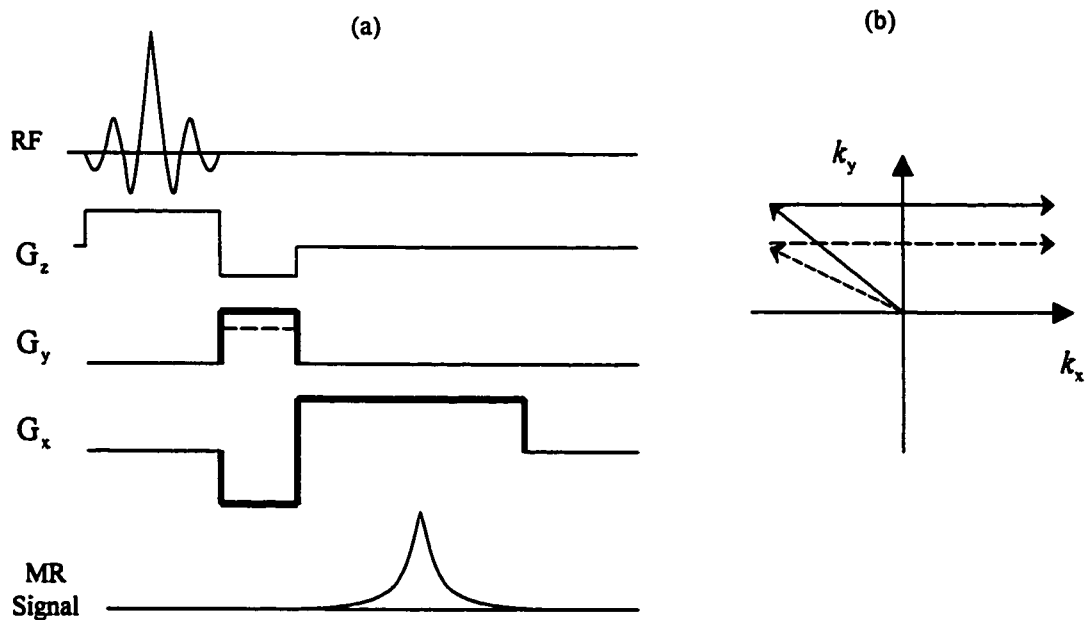


Figure 1-14 2D Fourier transform sequence: (a) timing diagram (b) k -space trajectory, where a single line of k -space is sampled during each repetition of the pulse sequence.

Beginning from the origin, the k-space trajectory (the order in which each (k_x, k_y) point is sampled) moves along the k_y axis during the G_y interval to create the proper vertical location according to Eq. (1-21). The negative part of G_x will move the k-space trajectory to the left side to make the signal (echo) exactly in the center of k-space, and the positive part of G_x will read out the signal, horizontal line.

In the next step, the G_y value will change to locate a new position and so on. The process of selecting the value of k_y is called phase encoding (PE), whereas the process of sampling a line of k_x is called frequency encoding (FE). The experiment is repeated until the k-space grid is completed; for example, a $x = 128$ by $y = 128$ matrix acquisition would be repeated 128 times to collect all k-space.

Different kinds of pulse sequences are used for various imaging applications. Each pulse sequence can map k-space in a specific way, based on the time-varying shape of the localization gradients and Eq. (1-21). Some pulse sequence including spin echo (SE) [15], gradient echo (GE) [16], and echo planar imaging (EPI) [17] map k-space in a rectilinear (Cartesian) fashion as described above. Other pulse sequences map k-space in a non-rectilinear fashion, like projection reconstruction and spiral imaging [2].

1.4.2. Sampling Requirements in 2DFT imaging:

1.4.2.1. Field of View:

In MR imaging, sampling takes place in the spatial frequency domain, therefore, replication in the object domain must be considered as shown in Fig. 1-15 [19], where the separation of these replications determines the effective FOV in the image:

$$\text{FOV}_x = \frac{1}{\Delta k_x} = \text{sampling rate in } k_x \text{ direction} \quad (1-22a)$$

$$\text{FOV}_y = \frac{1}{\Delta k_y} = \text{sampling rate in } k_y \text{ direction} \quad (1-22b)$$

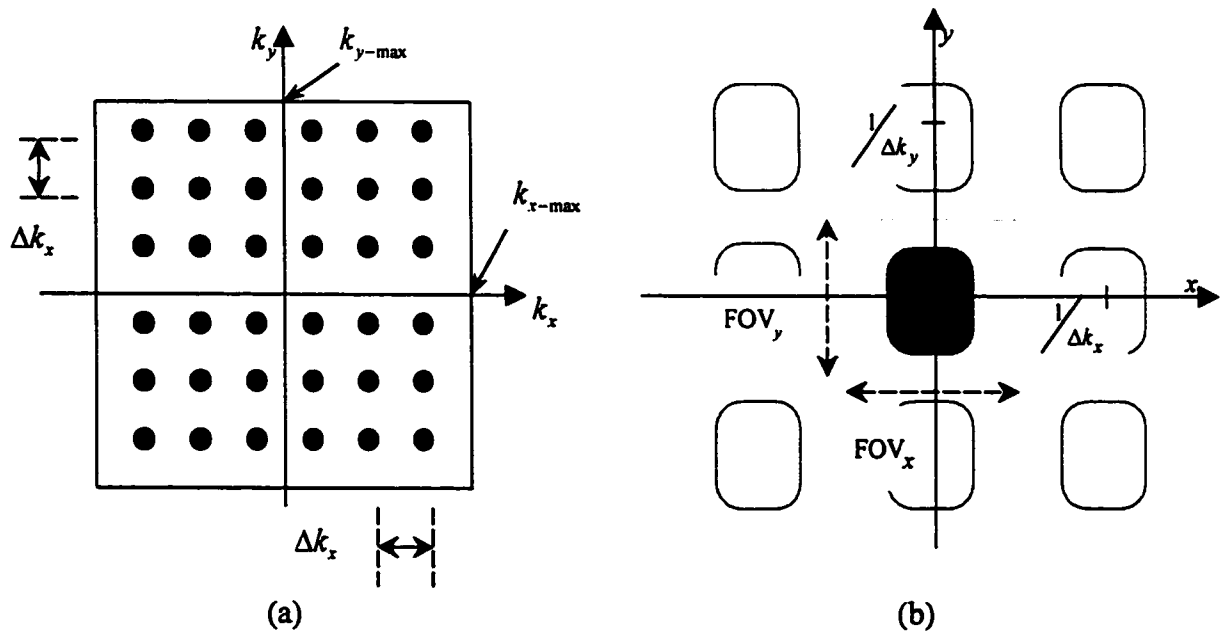


Figure 1-15 (a) Sampling in k-space (b) Corresponding replications in object domain.

To understand FOV in terms of the parameters of imaging, we use Fig. 1-16. Since the k -space position is a function of the incremental area under the gradient. Therefore, the sampling period Δk_x in the x direction depends on the readout gradient amplitude G_x and the sampling period Δt of the analogue-digital A/D converter [11]. The sampling period Δk_y in the y direction depends on the incremental gradient G_{y-inc} and the fixed phase encoding duration τ_y :

$$\Delta k_x = \gamma G_x \Delta t \quad (1-23a)$$

$$\Delta k_y = \gamma G_{y-inc} \tau_y \quad (1-23a)$$

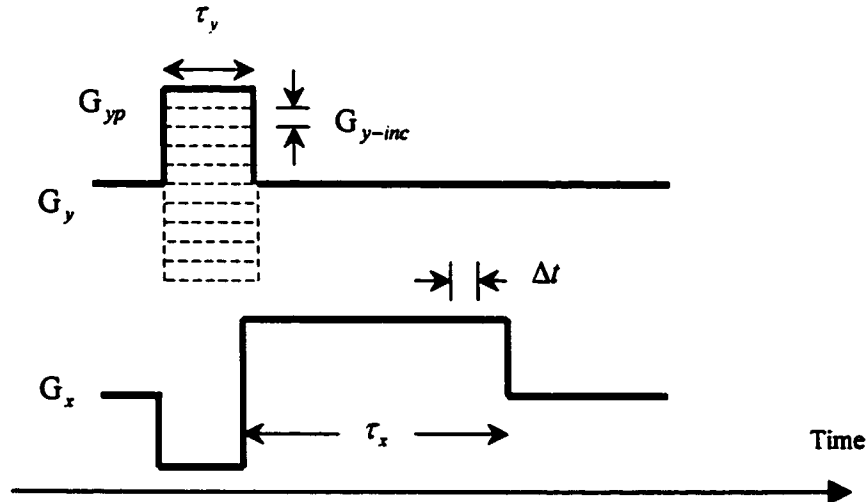


Figure 1-16 Timing and amplitude parameters: G_{y-inc} incremental gradient amplitude; G_{yp} maximum gradient amplitude. G_x readout gradient amplitude; τ_x total readout time.

From these equation and using Eq. (1-21) we can write the expression for FOV

as:

$$FOV_x = \frac{1}{\Delta k_x} = \frac{1}{\gamma G_x \Delta t} \quad (1-24a)$$

$$FOV_y = \frac{1}{\Delta k_y} = \frac{1}{\gamma G_{y-inc} \tau_y} \quad (1-24b)$$

1.4.2.2. Spatial Resolution:

The k -space sampling is finite, as shown in Fig. 1-15, where the maximum distance is $2k_{x-max}$ and $2k_{y-max}$ in the readout and phase encoding directions, respectively. For a given FOV and number of sample points, we can define the spatial resolution Δx and Δy in the x and y directions respectively as:

$$\Delta x = \frac{FOV_x}{N_{read}} = \frac{1}{\Delta k_x N_{read}} = \frac{1}{2k_{x-max}} \quad (1-25a)$$

$$\Delta y = \frac{FOV_y}{N_{pe}} = \frac{1}{\Delta k_y N_{pe}} = \frac{1}{2k_{y-max}} \quad (1-25b)$$

where N_{read} is the number of readout samples and N_{pe} is the number of phase encoding steps.

From Eqs. (1-24) and (1-15) we can write the spatial resolution Δx and Δy as:

$$\Delta x = \frac{1}{\gamma G_x \tau_x} \quad (1-26a)$$

$$\Delta y = \frac{1}{2 \gamma G_{yp} \tau_y} \quad (1-26b)$$

where we have noted from Fig. 1-16 that the readout length τ_x is $N_x \Delta t$ and the maximum phase encoding gradient $G_{yp} = (N_y / 2) G_{y-inc}$.

1.5. References:

1. Potchen, E., *et al.*, *Magnetic Resonance Angiography: Concepts and Applications*. 1993, St. Louis: Mosby.
2. Haacke, E.M., *Magnetic Resonance Imaging, physical principles and sequence design*. 1999: John Willey & Sons.
3. Luiten, A.L., *Fundamentals of NMR imaging*. *Diag. Imag. Clin. Med*, 1984. **53**: p. 4-12.
4. Bronskill, M.J., *The physics of MRI 1992 AAPM summer school proceeding*. 1993, Woodbury: American Institute of Physics, Inc.
5. Slavin, G., *EPI*. 1997, Mayo clinic: Rochester, Ph.D. thesis.
6. Butts, R.K., *Three fast scan techniques in MRI*. 1993, Mayo clinic: Rochester, Ph.D. thesis.
7. Debbins, J.P., *High speed interactive techniques for thoracoabdominal cardiovascular MRI*, . 1997, Mayo clinic: Rochester, Ph.D. thesis.
8. Hinshaw, W.S., *An introduction to NMR imaging*. *Proceeding of the IEEE*, 1983. **71**(3): p. 338-350.
9. Bloch, F., *Nuclear induction*. *Physical Review*, 1946. **70**: p. 460-474.
10. Purcell, E.M., H.C. Torrey, and R.B. Pound, *Resonance absorption by nuclear magnetic moments in a solid*. *Physical Review*, 1946. **69**: p. 37-38.
11. Nishimura, D.G., *Principles of magnetic resonance imaging*. 1996: Stanford University.

12. McRobbie, D.W., *Investigation of slice characteristics in NMR imaging*. Phys. Med. Biol., 1986. **31**(6): p. 613-626.
13. Freeman, R., *Shaped radiofrequency pulses in high resolution NMR*. J. of Progress in NMR Spectroscopy, 1998. **32**: p. 59-106.
14. Bracewell, R.N., *The Fourier Transform and its Applications*. 1978: McGraw-Hill. pp. 122.
15. Bishop, J. and D. Plewes. *Stimulated echo effects in fast spin echo images*. in *10th Annual Mtg. Soc. Magn. Reson. in Med*. 1991. San Francisco.
16. Bampton, A.E.H. and S.J. Riederer, *Improved efficiency in magnetization-prepared rapid gradient echo imaging: application to abdominal imaging*. Magn Reson in Med, 1992. **25**: p. 195-203.
17. Turner, R., et al. *Functional neuroimaging with EPI: sequence issues*. in *Functional MRI of the Brain, A Workshop presented by the SMRM and the SMRI*. 1993. Washington, DC.
18. Wilman, A.H. and S.J. Riederer, *Peformance of an elliptical centric view order for signal enhancement and motion artifact suppression in breath-hold three-dimensional gradient echo imaging*. Magn Reson Med, 1997. **38**: p. 793-802.
19. Brigham, O.E., *The fast fourier transform*. 1974, New Jersey: Prentice-Hall.

CHAPTER 2

Time of Flight Angiography

2.1. Introduction:

Since MR angiography was founded, the primary development goals have been increasing the speed of acquisition, increasing the image contrast, and increasing the spatial resolution. For the latter two goals, the advantages of high field MRA lie in the fact that the signal to noise ratio (SNR) increases with B_0 and the T1 relaxation times are longer [1]. The first advantage, SNR, means that smaller voxel sizes may be used when compared to lower field strengths. Secondly, the longer T1 values can lead to better background suppression. High contrast MRA images have been accomplished by manipulating the pulse sequence parameters based on T1 relaxation times as well as inflow rates of blood [2].

To address the variety of useful MRA techniques, this chapter will explain the importance of each technique with supporting theoretical and experimental results on phantoms or in-vivo. Since MRA can be accomplished by fast imaging methods, the basic concepts behind short repetition time pulse sequences will be explained as they relate specifically to imaging moving blood. Using our 3T magnet, we then compare intracranial MRA results to those on a 1.5T clinical scanner and study the effects of field strength on SNR, blood to background contrast, and vessel conspicuity.

2.2. Time of Flight (TOF):

The beginnings of MRA date back to 1951 when Suryan [3] observed that the T1 of flowing water was different from the T1 of stationary water. The reason was that continuous excitation saturated the spins in stationary water, while fresh magnetized spins replaced the saturated ones in flowing water, hence giving a stronger signal. This is called the in-flow effect. Later on Singer [4] [5] suggested an in-flow experiment to measure the change in signal amplitude of blood. In 1989 Keller [6] developed 2D TOF with two dimensional acquisition and three dimensional display to improve the visibility of blood vessels.

In Fig. 2-1 the imaging volume (slice excitation volume) is perpendicular on the blood vessel direction. By applying a moderate excitation flip angle and repetition time (TR) much shorter than the tissue T1 values, the stationary tissue experiences every RF excitation pulse but the flowing blood does not [1] [7]. The blood volume will be at different locations at the time of every excitation pulse due to its moving during TR. The highest signal from the blood volume is at the entry point of the imaging volume because it has not suffered any excitation pulses [8]. As the blood travels through the slice, it loses signal as it suffers more excitation pulses and becomes saturated. The degree of blood saturation depends on TR, slice thickness, excitation angle, and flow velocity [9]. Therefore, suitable parameters must be chosen for each specific application to have high signal from blood, while limiting background signal.

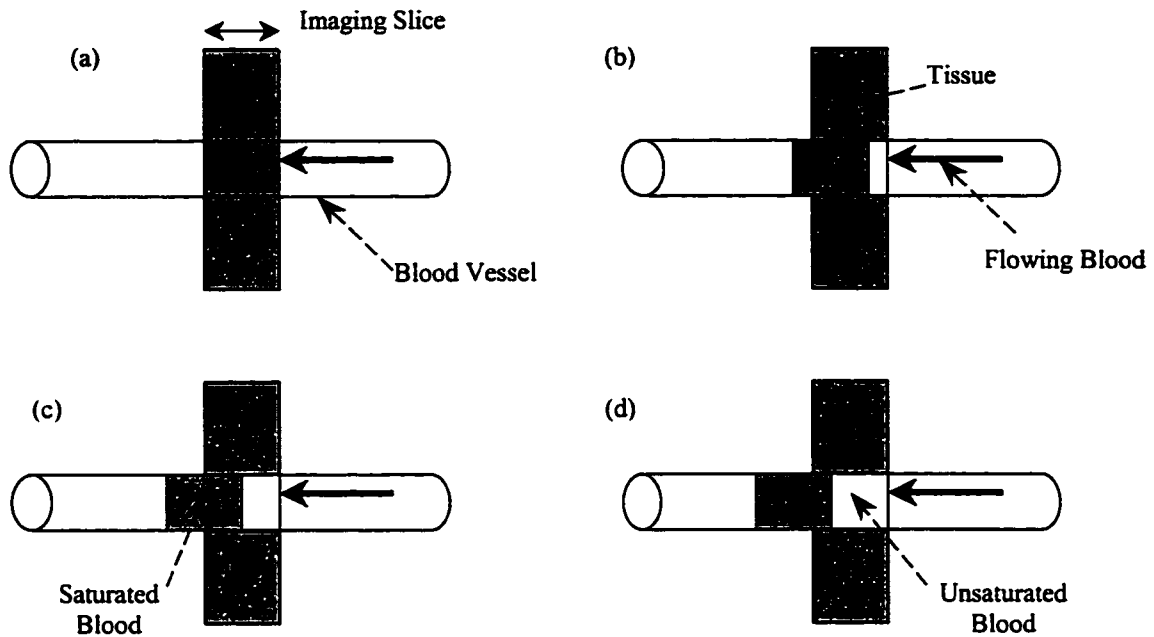


Figure 2-1 During data acquisition in time of flight the imaging, the slice (volume) experiences many RF pulses. (a) Flowing blood experiences the first RF pulse. (b,c) During TR, the excited blood moves and only part of it experiences another RF. (d) At the end of TR, the initial blood volume will be outside the excitation slice without any contribution to the detected signal.

The blood signal, the transverse magnetization M_{xy} , just after the n^{th} RF pulse with flip angle α is found from the Bloch equation [1]:

$$M_{xy}(n) = \left\{ [M_z(n-1) - M_0] \exp(-TR/T_1) + M_0 \right\} \sin(\alpha) \quad (2-1)$$

Fig. 2-2 shows blood signal plots for various flip angles, illustrating the signal saturation with increasing number of RF pulses. This plot assumes blood receives all of the RF pulses. In reality, the blood will move out of the volume before receiving all of the pulses and fresh blood will continually flow in. However, background tissues remain

stationary so the steady-state can be used. The Bloch equation at steady state for background can be expressed as [1]:

$$M_{xy} = \frac{M_0 [1 - \exp(-TR/T_1)]}{1 - \cos(\alpha) \exp(-TR/T_1)} \sin(\alpha) \quad (2-2)$$

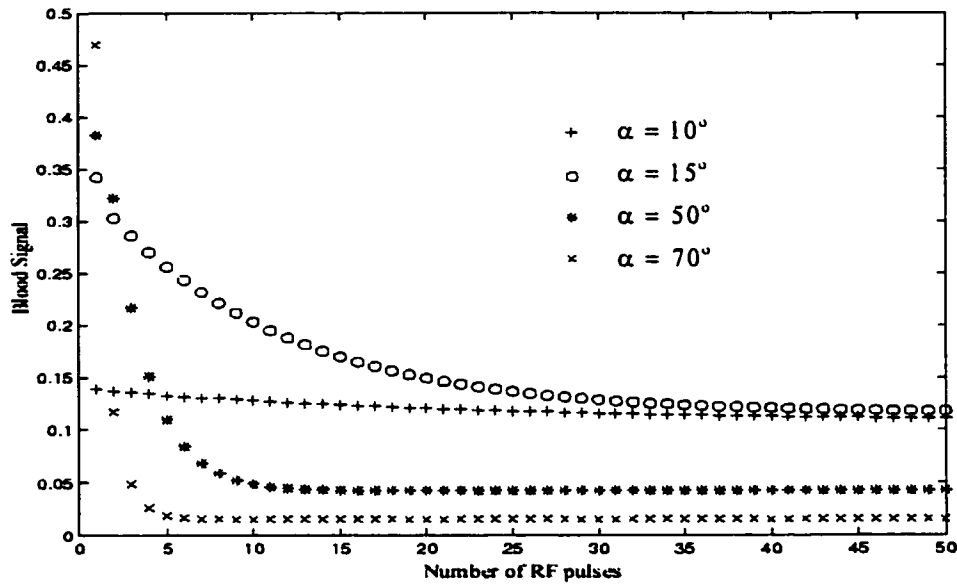


Figure 2-2 Blood signal as a function of the number of RF excitation pulses. $T_1=1200\text{ms}$ and $TR=36\text{ms}$ [1]. In spite of the high flip angles start off with more magnetization for low n , number of pulses, the flip angle giving the highest steady signal is associated with the Ernst angle ($E = \cos^{-1}(e^{-TR/T_1}) = 14^\circ$).

2.3. Pulse Sequence Design:

The heart of magnetic resonance imaging exists in the sequence design to extract the desired information from a specific region of interest. This process can be achieved by making sequences sensitive to a specific tissue property such as T_1 or T_2 , flow or other parameters [10]. This section discusses advanced imaging techniques that are used in imaging blood vessels. There are a variety of pulse sequences possible to collect the

information. In this work we used gradient echo (GE) sequences [11] [12] which have the advantage of short echo times compared to spin echo sequences (SE) [13].

2.3.1. Design of 2D Time of Flight:

The first part of any sequence structure is to excite a slice using an RF pulse, where the shape of the RF field $\mathbf{B}_1(t)$ is shown in Fig. 2-3 along the RF line. Usually the excitation pulse is combined with a slice select gradient that is turned on early relative to the RF pulse to stabilize the gradient amplitude and dephase any remnant transverse magnetization as shown in the G_z line. Next the slice refocusing lobe is used to rephase the spins before data acquisition in a way that the zeroth moment of $G_z(t)$ from the top part of the RF pulse to the end of the negative part is equal to zero, the shaded gradient area in G_z line.

In Fig. 2-3 a truncated sinc pulse is used instead of a symmetric one as shown in Fig. 2-4 [14] in order to make the echo time as short as possible which helps in capturing the signal from flowing blood before it suffers more dephasing from flow effects. Both G_y and G_x lines are used to encode the signal in the x and y directions as explained in chapter one (section 1.3.). It is clear from the sequence diagram that the gradients must be quite compact to achieve a short TE. A sequential encoding technique is used in TOF sequences to encode the signal [1].

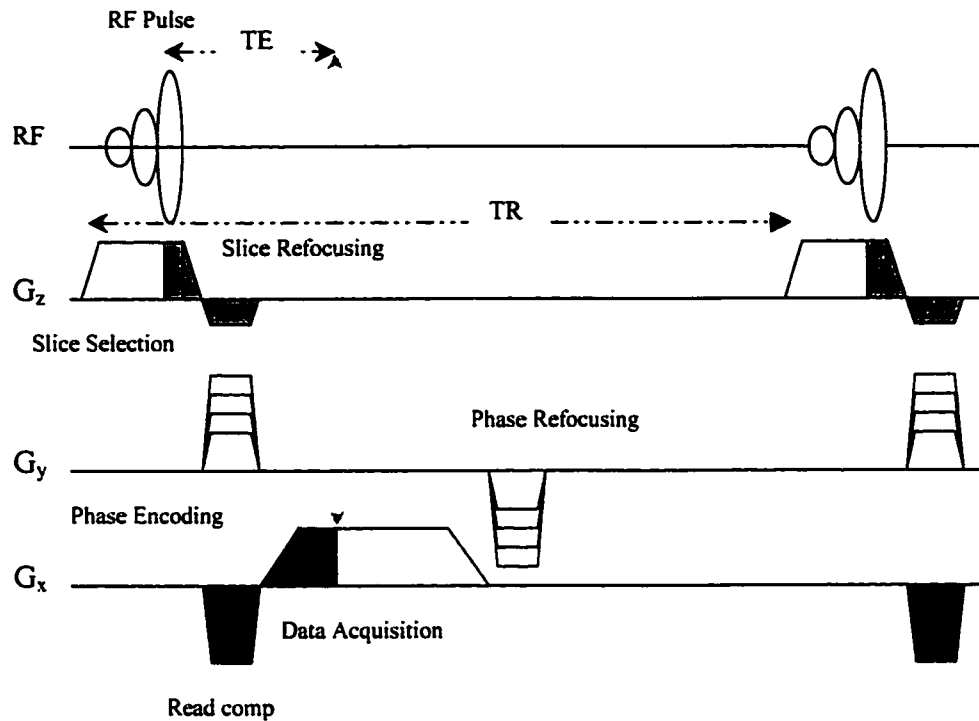


Figure 2-3 Sequence diagram with necessary timing and gradients for a 2D gradient echo imaging sequence. The shaded areas represent equal gradient areas. TR is the repetition time between two RF pulses.

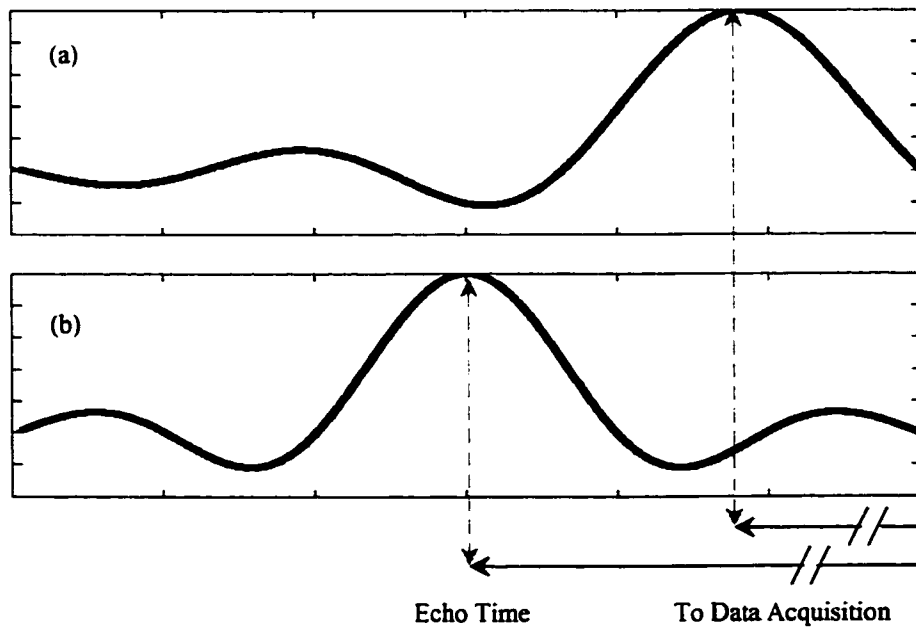


Figure 2-4 (a) Four lobe truncated sinc pulse to make the TE as short as possible, (b) The original five lobe symmetric sinc pulse.

In 2D TOF the TE can be calculated from the following equation [15]:

$$TE = RF_{time} + Phase-Encoding_{time} + Frequency-Encoding_{time} + Total-Ramp_{time} \quad (2-3)$$

By using a 50% fractional echo property in the frequency direction [16, 17], we shift the center of k-space to the left side and save 25% from the total time of data acquisition to reduce TE. Using Eq. (2-3) on our system we obtain:

$$TE = 300\mu s_{RF} + 540\mu s_{phase} + 1280\mu s_{read} + 880\mu s_{ramp-times} = 3000\mu s \quad (2-4)$$

where the reading window has 512 samples with a BW of 100KHz.

The multi-slice 2D approach is used to cover 3D volumes of interest (VOI's), where the RF pulse is centered at a different frequency to excite a different slice each time. Because the RF profile is not perfect the immediate neighborhood of an excited slice is also partly excited [18], which might cause some problems when we combine the slices.

2.3.1.1. Flow Compensation:

The effects of flowing blood on phase can lead to signal loss because the spins are not in phase at the echo center. Table 2-1 shows the effect of dephasing on the signal loss across a voxel.

ϕ	0	$\pi/4$	$\pi/2$	$3\pi/4$	π
Signal Loss	0%	10%	64%	45%	100%

Table 2-1 Representing the dephasing phenomenon due to a spread of velocities across a voxel [1]. ϕ is the phase at the center of the voxel assuming laminar flow.

To avoid this signal loss it is necessary to redesign the gradient lobes in a way that both stationary and moving spins have zero phase at the echo center [19] to be encoded correctly. In this case we consider the easiest motion that can be described as follows:

$$x = x_0 + v_x \cdot t \quad (2-5)$$

where x_0 is the initial position at time $t = 0$ and v_x is the constant velocity for spins in the x direction.

In Fig. 2-5 the additional gradient lobe is added to ensure that the phase at the echo is zero for both stationary and constant moving spins, these conditions lead to two equations, one for the zeroth moment of $G_x(t)$ and one for the first moment of $G_x(t)$.

$$M_0(t) = \int_0^{\tau} G_x(t) \cdot dt = 0 \quad (2-6)$$

$$M_1(t) = v_x \int_0^{\tau} t \cdot G_x(t) \cdot dt = 0 \quad (2-7)$$

The zero moment $M_0(t)$ must be zero to refocus the stationary spins and the first moment $M_1(t)$ must be zero to guarantee that $\phi_{v_0} = \phi_{v_r} = 0$ for all spins.



Figure 2-5 Constant velocity compensation gradient waveform (in read direction).

The sequence structure will have a slightly different shape as shown in Fig. 2-6, where the TE becomes bigger in this case due to the additional gradient lobe:

$$TE = RF_{time} + Phase-encoding_{time} + Frequency-Encoding_{time} + Flow\ Comp. + Ramp_{time} \quad (2-8)$$

$$TE = 300\mu s_{RF} + 1000\mu s_{phase} + 1280\mu s_{read} + 1100\mu s_{flow-comp} + 1320\mu s_{ramp-times} = 5000\mu s \quad (2-9)$$

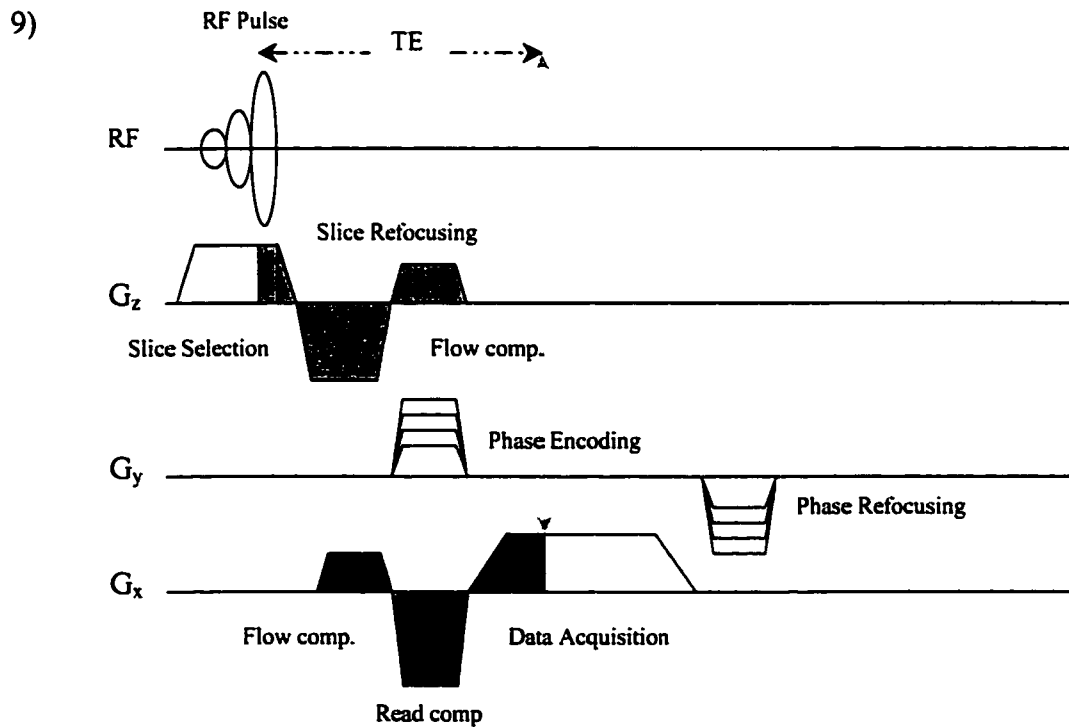


Figure 2-6 2D gradient echo with flow compensation gradients in x and z directions.

To check the effect of using flow compensation on image quality, two experiments were run on the same volunteer with the same parameters shown in Fig. 2-7a, a 2D TOF source image of the neck without flow compensation. Note the signal loss in the blood vessel that appears as ghosting across the image. This is particularly troublesome in the vessels containing high blood speeds. Fig. 2-7b illustrates a clear image of the neck after adding flow compensation. Note that ghosting disappears, which is essential to achieve high quality images.

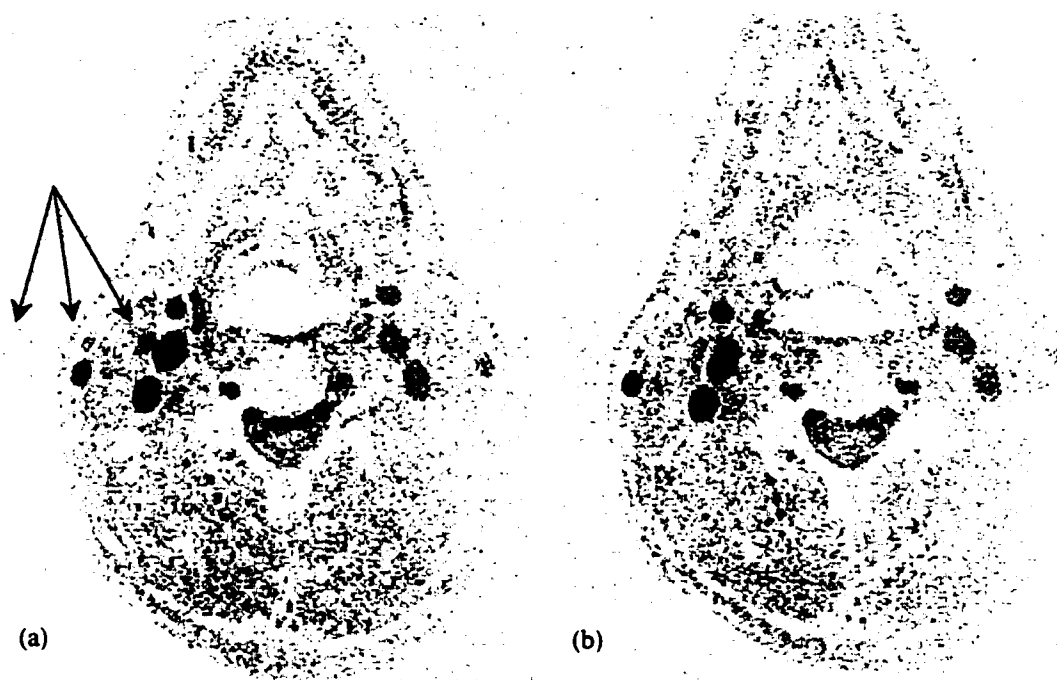


Figure 2-7 Two source images for the neck (a) 2D TOF without flow compensation. Note the ghosting line across the image (arrows). (b) After using flow compensation, the ghosting line disappears. (parameters for both TR/TE= 35/5.3ms, slice thickness 2mm, 512×256 resolution, FA 25°, FOV 200mm)

To see the effect of using higher spatial resolution on 2D images, two set of data were collected on the same volunteer using different resolutions. Fig. 2-8a shows low spatial resolution 256×256 with a slice thickness of 4mm, and Fig. 2-8b is after increasing the spatial resolution in 512×256 with a slice thickness of 2.4 mm. Note the

clearer image for the Circle of Willis, middle cerebral artery, vertebral artery, anterior cerebral artery, and the small blood vessels in both edges after using higher spatial resolution.

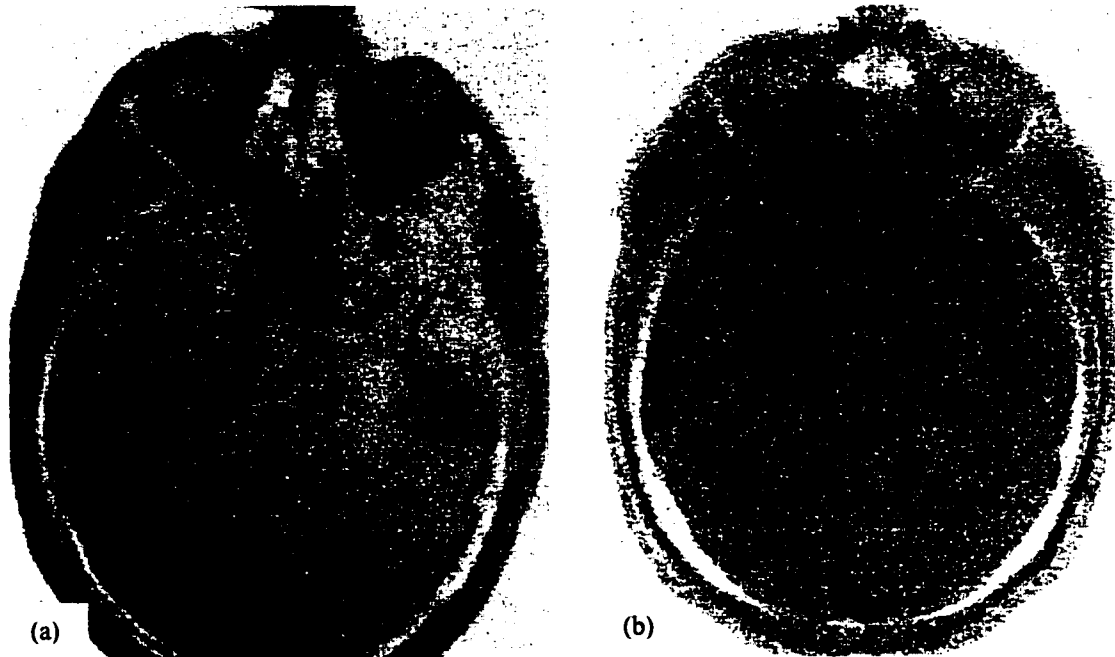


Figure 2-8 (a) 2D TOF, TE 3ms, slice thickness 4mm, 256×256 resolution (low resolution). (b) 2D TOF, TE 5ms, 512×256 resolution (high resolution), where we can see the small blood vessels in both sides, slice thickness 2.4mm, . (In both cases FA 30°, TR 30ms, FOV 200mm)

2.3.1.2. Maximum Intensity Projection:

Displaying blood vessels can take on many forms. For a set of 2D or 3D slices, it is possible to look through the images at a given angle and to take the maximum value along a line of sight and write this value to a point in a 2D plane, which is called the projection image as shown in Fig. 2-9 [20]. This technique is known as maximum intensity projection (MIP). By using it, we can view the vascular information from arbitrary angles.

Sometimes, viewing images as projection might block or hide the vessel of interest because of other bright structures. By determining the local region of interest, cutting out unwanted structures in each slice and then performing MIP, this problem can be avoided [1].

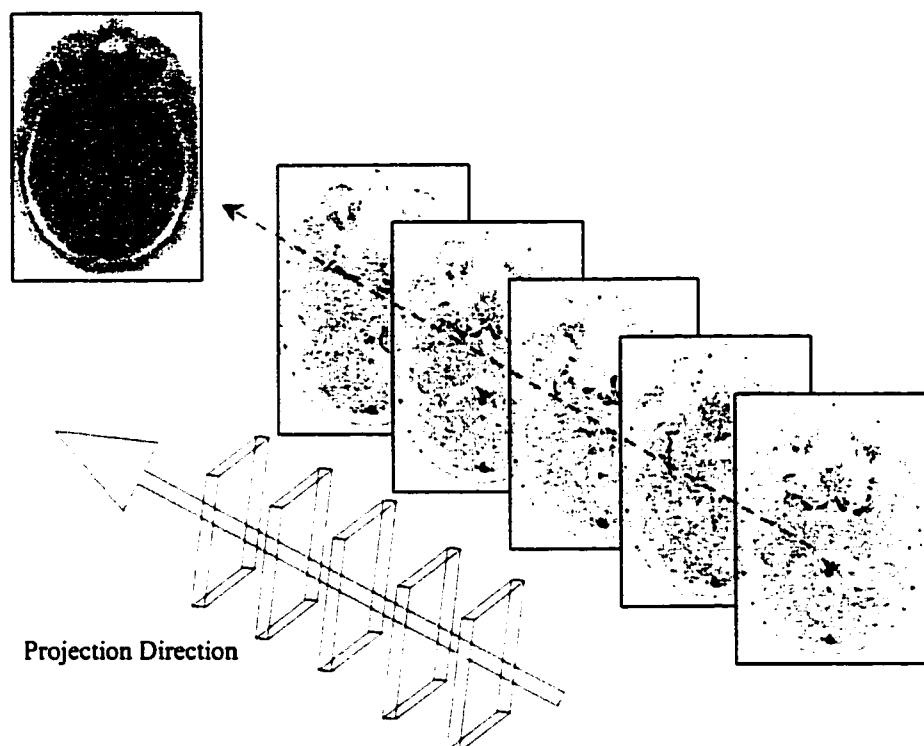


Figure 2-9 Obtaining a projection image by applying maximum intensity projection.

2.3.2. Design of 3D Time of Flight:

3D TOF is able to obtain thin slices for high resolution imaging and short TE [21] [22], whereas a thin slice in 2D TOF requires a long RF pulse time to create a sharp slice profile and the thickness is limited directly by the gradient strength [23]. Fig. 2-10 shows a 3D gradient echo sequence with flow compensation, where the slice encoding gradient is added to the 2D sequence to phase encode along the slice selection direction as well.

Both slice encoding and phase encoding are playing out at the same time, so no extra time is spent in this process. Each new RF pulse excites the same slab, but is followed by a different phase encoding gradient value.

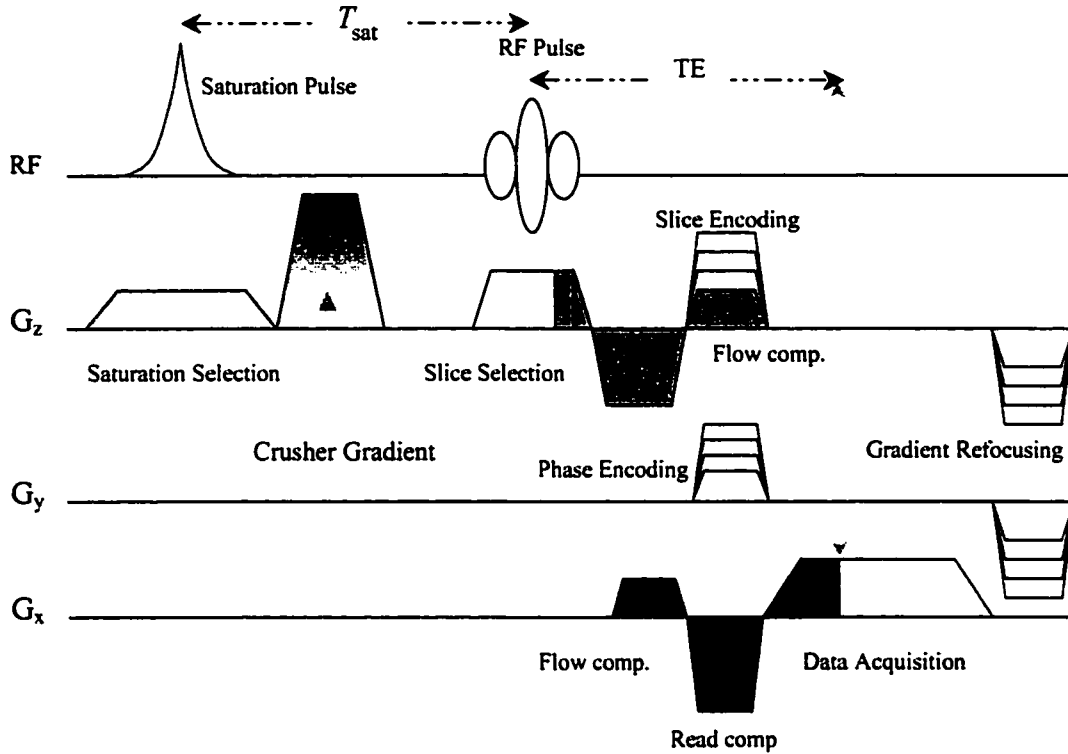


Figure 2-10 3D TOF with flow compensation in x and z direction and saturation pulse. Note the phase encoding in slice direction is playing out at the same time with phase encoding in y direction.

The advantages of using 3D imaging volume in comparison with 2D multi-slice imaging are [1]; first, the flexibility in changing the number of phase encoding steps over the slab in the slice direction [21] [24], which means more control over the slice thickness without any boundary on the RF amplitude or duration as can be expressed from this equation:

$$\text{Slice Thickness} = \frac{\text{Slab Thickness}}{\text{Number of Phase Encoding in Slice Direction}} \quad (2-10)$$

Second, consecutive slices can be adjacent in a 3D slab, whereas in 2D the RF pulse leaks into the neighboring slices because the slice profile is never perfect. Third, larger RF BW can be applied for a thicker slab, and that will shorten the RF pulse time, making it easy to reduce TE, which is very important when performing MRA. Fourth, both short TE and high spatial resolution in the slice direction help in reducing signal loss due to T2* dephasing [25]. Fifth, the signal to noise ratio can be enhanced because of the extra parameter available in a 3D sequence, N_z [26], the number of phase encoding steps in the slice direction. For 2D imaging the SNR can be expressed as:

$$SNR_{2D} = \left(\frac{TH_{Slice}}{1} \right) \left(\frac{FOV_R}{N_R} \right) \left(\frac{FOV_{PE}}{N_{PE}} \right) \sqrt{\frac{N_{acq} N_R N_{PE}}{BW_{rec}}} \quad (2-11)$$

where TH slice thickness, FOV_R field of view in the read direction, N_R number of acquired samples, FOV_{PE} field of view in the phase direction, N_{PE} number of phase encoding steps in y direction, N_{acq} number of acquisitions, and BW_{rec} receiver bandwidth.

For 3D imaging the SNR is:

$$SNR_{3D} = \left(\frac{TH_{Slab}}{N_z} \right) \left(\frac{FOV_R}{N_R} \right) \left(\frac{FOV_{PE}}{N_{PE}} \right) \sqrt{\frac{N_{acq} N_R N_{PE} N_z}{BW_{rec}}} \quad (2-12)$$

where TH_{Slab} the slab thickness, N_z number of phase encoding steps in z direction. The first three parentheses in both equations represent the voxel dimensions and the numerator in the square root term relates to signal averaging while the denominator relates to noise contributions to the final measured signal [7].

2.3.2.1. Ramp Pulse:

The saturation encountered when the blood propagates into the slab remains an important issue in 3D TOF, because the slab is typically thick (around 3cm) and spins will suffer from many RF pulses before they leave it as shown in Fig. 2-2. Therefore, we use a special RF pulse with a slice excitation profile that increases linearly throughout the imaging slab as shown in Fig. 2-11 [27], where the excitation pulse has a small flip angle when the blood enters the slab and a larger flip angle when the blood exits the slab as shown in Fig. 2-12. The larger flip angles provide a larger signal than would be achieved by using smaller ones [28]. These larger flip angles will saturate the blood beside the edge, which is acceptable since the saturated blood will leave the slab sooner.

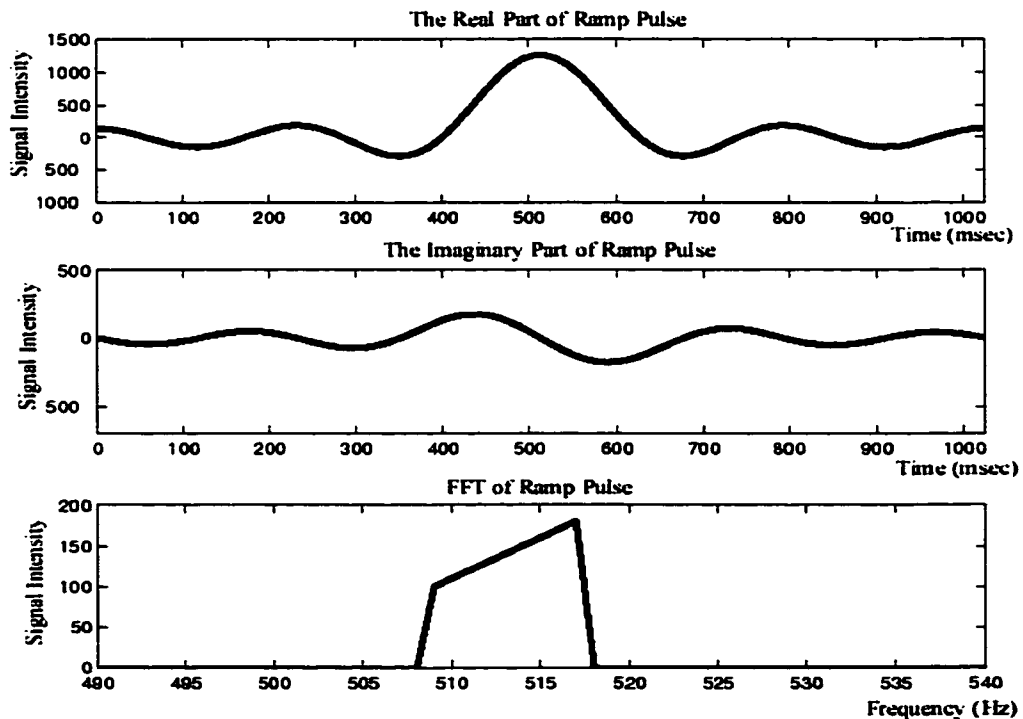


Figure 2-11 Both real and imaginary parts of the ramp pulse and its FFT (slice excitation profile).

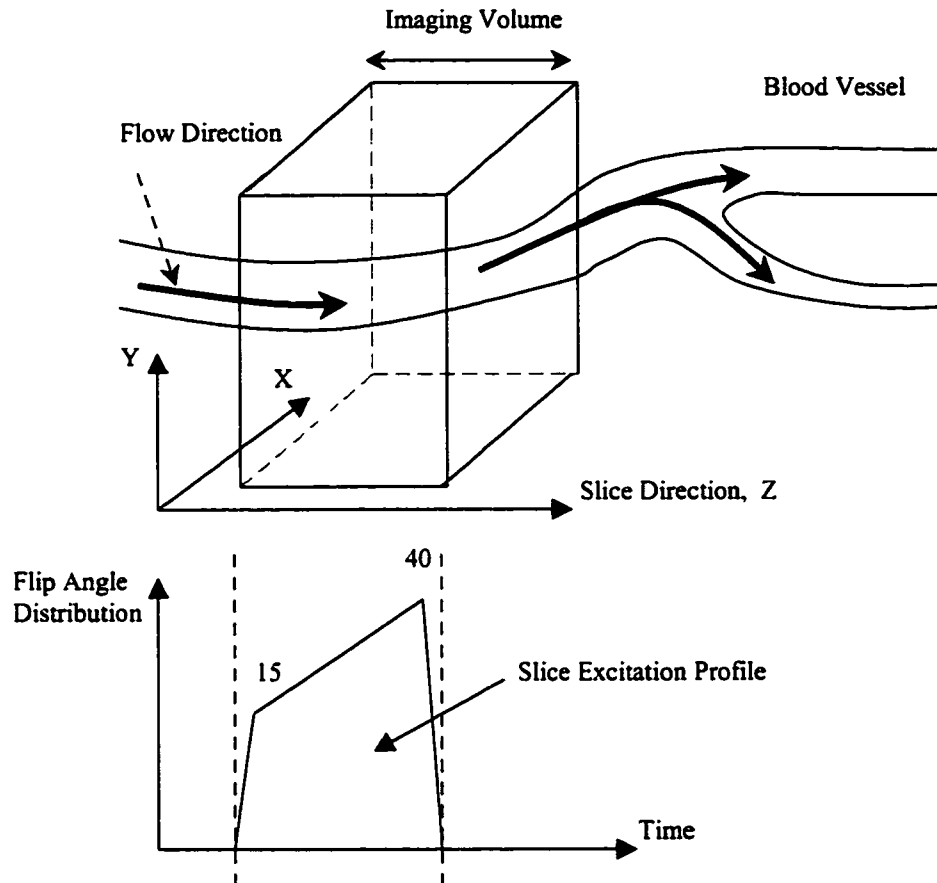


Figure 2-12 Flip angle distribution through the imaging volume, where a small flip angle is applied when the blood enters the slab and a larger one when it exits the slab to produce higher signal beside the exit edge.

Fig. 2-13 shows an in-vivo experiment for using the ramp pulse. Fig. 2-13a represents the ramp pulse with a small flip angle as the blood enters the 3D slab and increases linearly as the blood moves through it, you can see the extended parts of the small vessels are visible. In Fig. 2-13b for the same volunteer with the same parameters but reversing the direction of the ramp pulse, from large flip angle as the blood enters the slab to small flip angle as it leaves. In this case some of the extended parts are not visible any more.

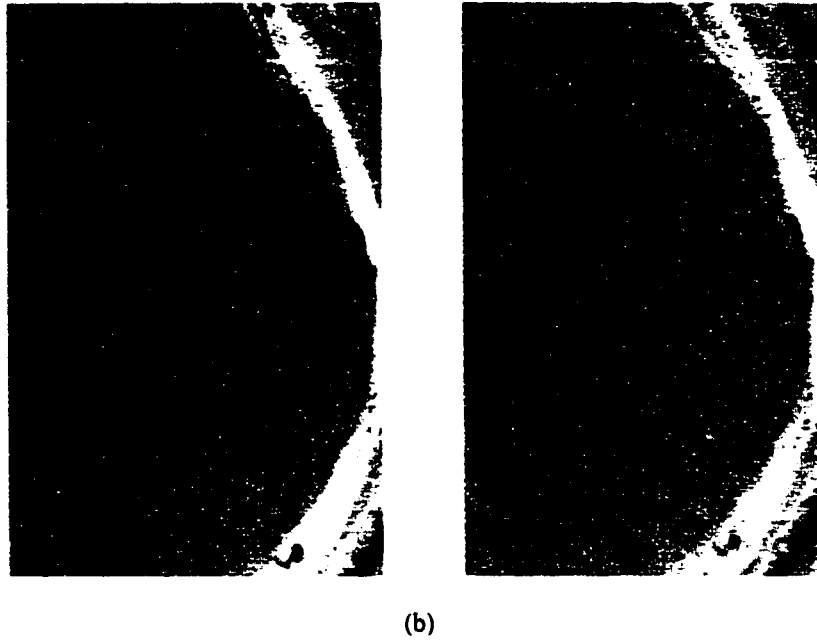


Figure 2-13 (a) Applying the ramp pulse with flip angle increasing linearly as the blood flows into the imaging volume (b) reverse the direction of the ramp pulse; note the effect of reversal on visualization of the extended parts of small vessels (arrows) (parameters for both $512 \times 256 \times 32$ resolution FA 25° , TR/TE= 36/7ms, FOV 200mm).

2.3.2.2. Saturation Pulse:

In many applications it is desirable to selectively image either arteries or veins. To do this a saturation pulse can be placed either above or below the imaging slab [8] [29], followed shortly by the RF excitation pulse. Figures. 2-14 and 2-15 illustrate the effect of saturation pulse. The time T_{sat} , as shown in Fig. 2-10, between the saturation and excitation pulse depends on the velocity of the flowing blood and imaging parameters. Usually, T_{sat} is on the order of 5-10ms, and the saturation pulse thickness can be varied from a few mm to cm. In our study to produce a sharp excitation profile a 7-lobe-sinc pulse is used, with 90° flip angle, 40mm thickness, and 10mm away from the slab to avoid any interfering with RF pulse.

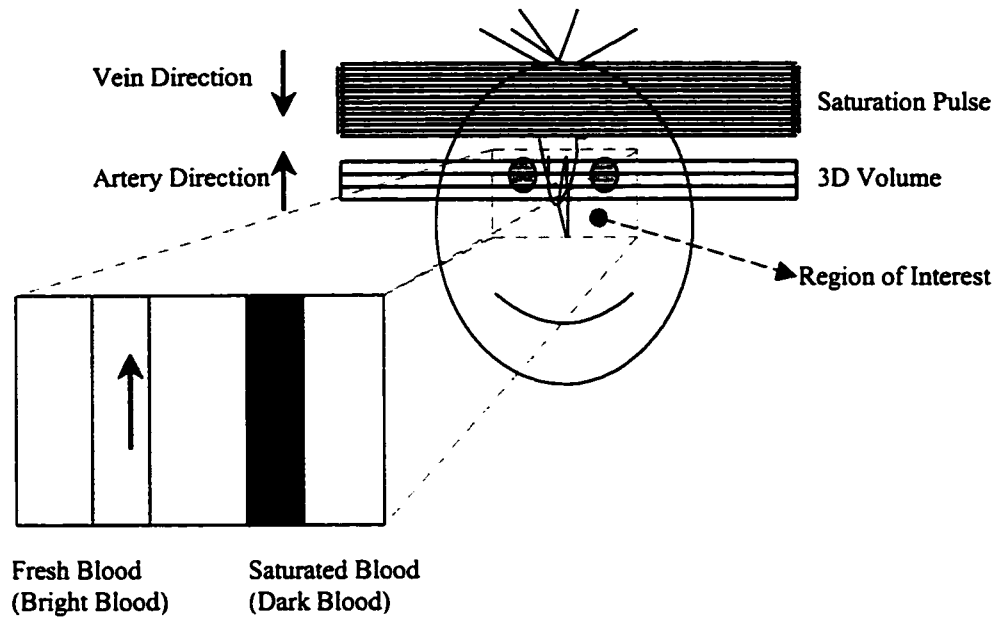


Figure 2-14 A schematic of a 90° saturation pulse to saturate the signal from veins and RF excitation pulse to image the 3D slab, mainly arterial signal.

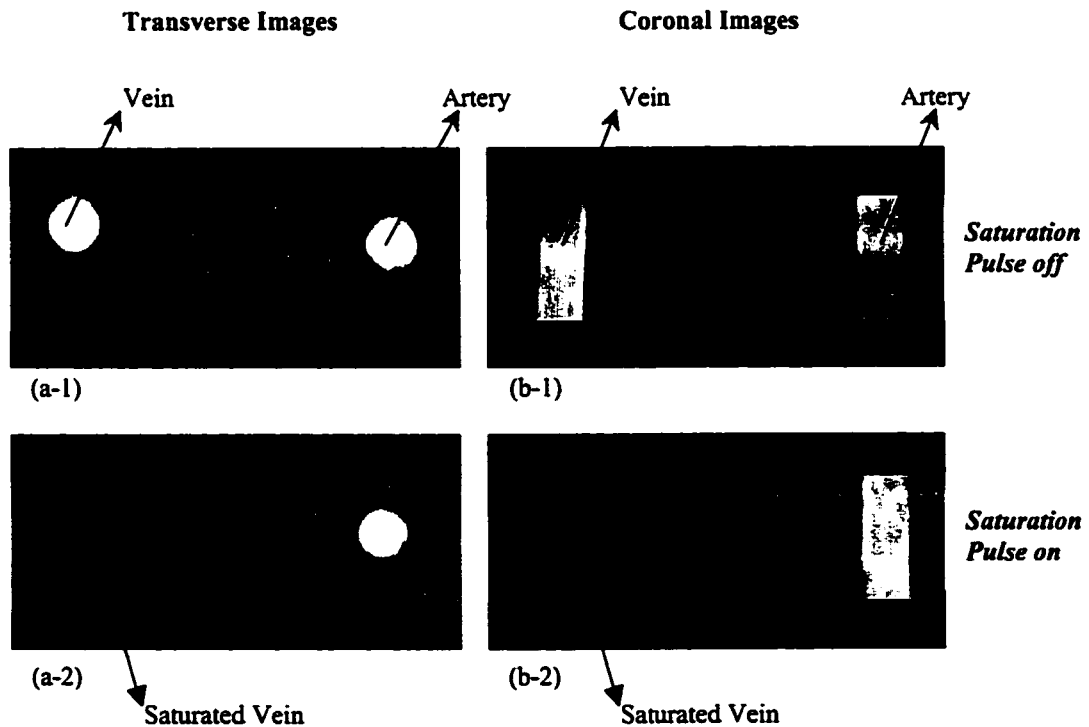


Figure 2-15 Applying 3D TOF with saturation pulse on a flow phantom. (a) The transverse images show clearly how the vein is saturated when the saturation pulse is turned on. (b) Also from the coronal images we can see that the venous signal has vanished. (In both cases FA 25° , TR/TE=36/7ms, $512 \times 80 \times 16$ resolution, FOV 200mm)

Fig. 2-16 shows applying 3D TOF with saturation pulse on a human neck, note that without the saturation pulse both veins and arteries will appear in the image.

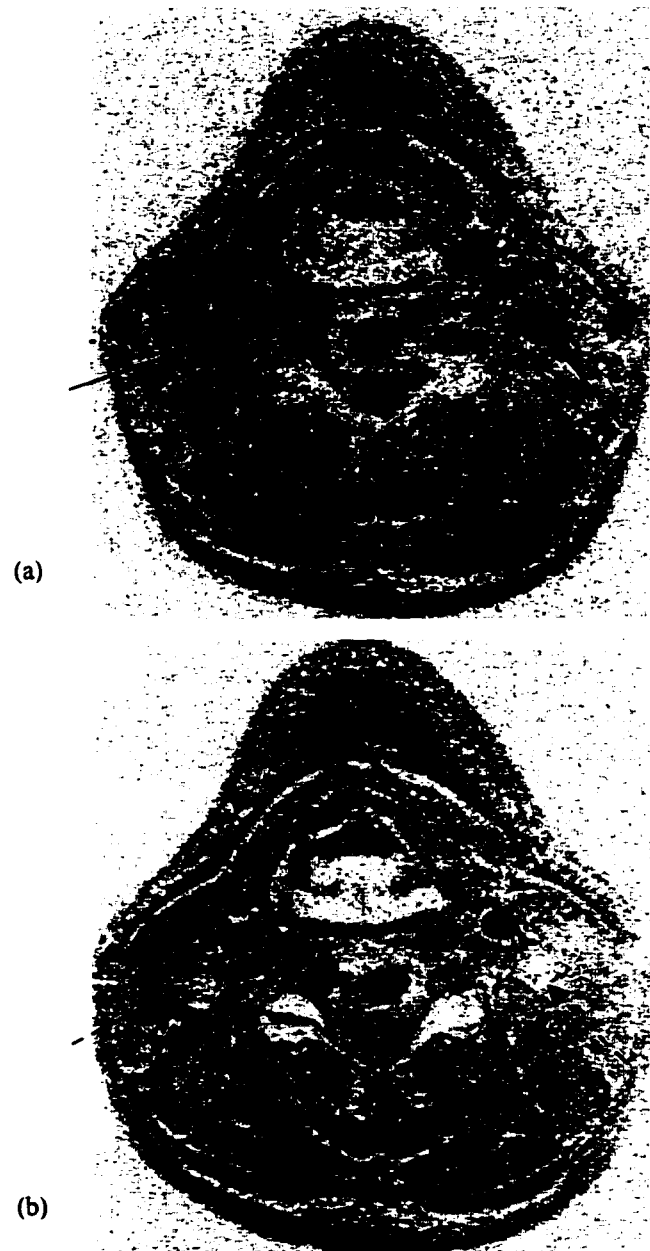


Figure 2-16 3D TOF with a saturation pulse of a human neck. (a) A transverse image without saturation pulse shows both the carotid artery and jugular vein (solid arrow). (b) After using the saturation pulse the signal from the jugular vein is vanished (dashed arrow). (In both cases FA 25°, TR/TE=36/7ms, 512×256×32 spatial resolution, FOV 200mm).

In the pulse sequence, Fig. 2-10, a Crusher Gradient is used after the saturation pulse to spoil the transverse magnetization created by the saturation pulse and prevent encoding it with the desired signal. Therefore, the RF slab thickness is reduced slightly to keep the edges of the excited region within the imaging volume. In our case we used a 2.8cm RF slab thickness with a 3.2cm imaging dimension. Approximately 3 slices are deleted from each side of the imaging volume to further limit this effect.

2.3.2.3. Multiple Overlapping Thin-Slab Acquisition (MOTSA):

A significant improvement in blood vessel visibility has been achieved by acquiring multiple overlapping thin 3D regions [31] [32]. Using thin slab regions increases the benefit of fresh in-flow enhancement, while maintain the 3D benefit of very small voxel, short TE, and higher signal. In the MOTSA technique, several 3D slabs can be combined to image longer segments of vessels, where one 3D slab is slightly overlapped with the adjacent one to delete few slices in both slab edges, because in 3D imaging signal contributions of spins that are excited outside the slice profile will be aliasing into the imaging region affecting the quality of the resulting images. Fig. 2-17 shows an example of MOTSA techniques using two 3D overlapped slabs for the Circle of Willis.

More slabs can be combined to cover even a larger area on the body in order to trace the blood anatomy. Fig. 2-18 shows combining four slabs for the head using the MOTSA technique with 1mm slice thickness (32mm slab).



Figure 2-17 Combining two 3D slabs for the Circle of Willis in the same volunteer using the MOTSA technique at 3T. (FA 25° , TR/ TE = 36/7ms, $512 \times 256 \times 32$ resolution, FOV 200mm, with flow compensation).



Figure 2-18 Combining four 3D slabs for vertebral artery, Basilar artery, and the Circle of Willis using the MOTSA technique at 3T. (FA 25° , TR/ TE = 36/7ms, $512 \times 256 \times 32$ resolution, 1mm slice thickness, FOV 200mm, with flow compensation).

2.4. Comparing 2D with 3D TOF:

As explained earlier, the 3D sequence has many advantages over the 2D sequence. With the 3D sequence the higher SNR and thinner slice thickness can give finer details in the images, thus better displaying small blood vessels. An in vivo experiment using 2D and 3D sequences was run on the same volunteer to check the difference between them. Note that the optimal parameters for both of them were used in this comparison [33]. Fig. 2-19 shows the MIP images for the Circle of Willis using 2D and 3D sequences, it is clear that the signal in the 3D is higher than in the 2D where the small blood vessels can be seen.

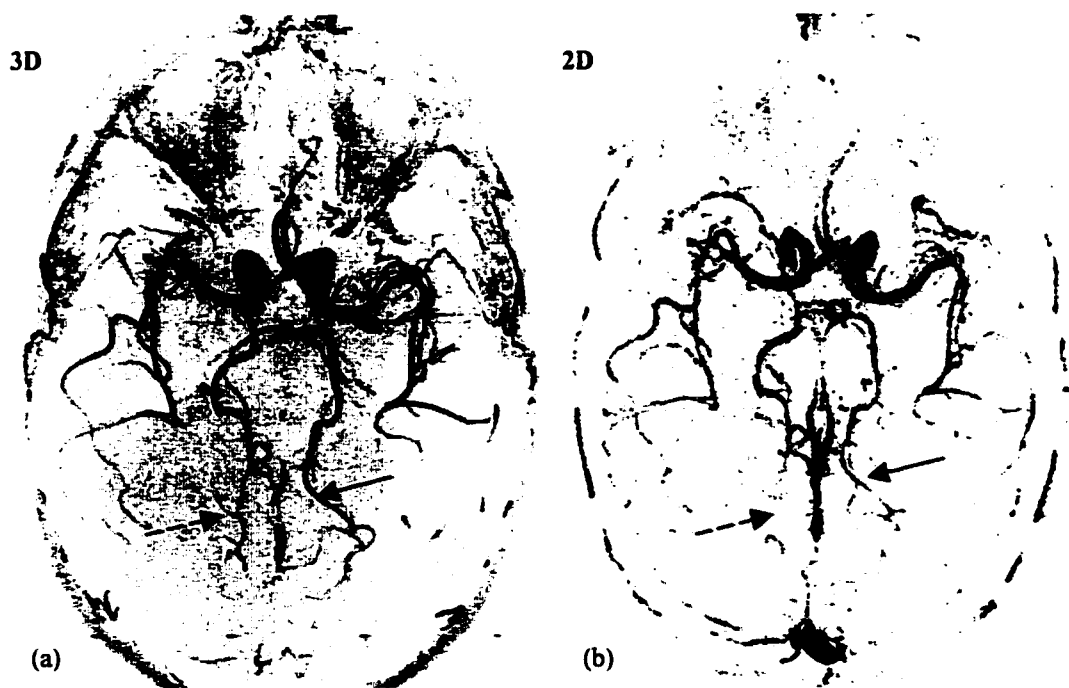


Figure 2-19 Both images for the Circle of Willis in the same volunteer: (a) MIP images of 3D MOTSA with flow compensation (FA 25°, TR/TE = 36/7ms, 512×256×32 resolution, FOV 200mm, slice thickness 1mm). (b) MIP images of 2D multi-slices with flow compensation (FA 30°, TR/TE= 30/5ms, 512×256 resolution, FOV 200mm, slice thickness 2.4mm). Note the significant increase in vessel visibility (solid arrows), and the appearance of the small vessels (dashed arrows).

Table 2-2 shows some measurements from Fig. 2-19 for the middle cerebral artery (MCA) signal: background, noise, SNR, contrast to noise ratio (CNR) [29], and normalized contrast (C) ($[\text{blood} - \text{background}] / \text{background}$). The data clearly demonstrate that 3D has higher signal than 2D, almost 56% more signal, and a significant increase in the SNR, three times more.

Sequence	Blood MCA	Back- ground	Noise	SNR MCA/Noise	CNR	C Contrast
2D	20888	4648	1002	20.88	16	3.49
3D	25680	3184	360	71.33	62	7.06

Table 2-2 The signal measurement for both 2D and 3D images in Fig. 2-18. These measurements were made on the same location in both source images. It can be seen the tremendous improvement in SNR, CNR, and Contrast.

In addition to that, coronal views from the same two data sets are shown in Fig. 2-20, where the importance of the thin slice thickness can be seen. The 3D sequence uses a 1mm slice thickness compared to 2.4mm in 2D, where the slice thickness is directly controlled by the available gradient strength.



Figure 2-20 Coronal view for the Circle of Willis in the same volunteer: (a) 2D multi-slices (FA 25°, TR/TE= 30/3ms, 512×256 resolution, FOV 200mm, slice thickness 2.4mm). (b) One slab 3D with flow compensation. Note the significant increase in vessel visibility (FA 25°, TR/ TE = 36/7ms, 512×256×32 resolution, FOV 200mm, slice thickness 1mm). It is clear that using 3D sequences improves the vessel visibility and increases the signal intensity from the small vessels.

2.5. Improving 3D TOF Images:

2.5.1. Increasing the Spatial Resolution:

Spatial resolution in 3D TOF imaging can be enhanced by decreasing the pixel size, hence, by broader coverage in k -space, as shown in Eq. (1-26) [34]. In Fig. 2-21 a 3D sequence with a different number of samples in the N_x and N_y direction is used on a resolution phantom. Increasing the number of samples lead to an increase in the spatial resolution, where the reduced voxel size gives higher resolution [1].

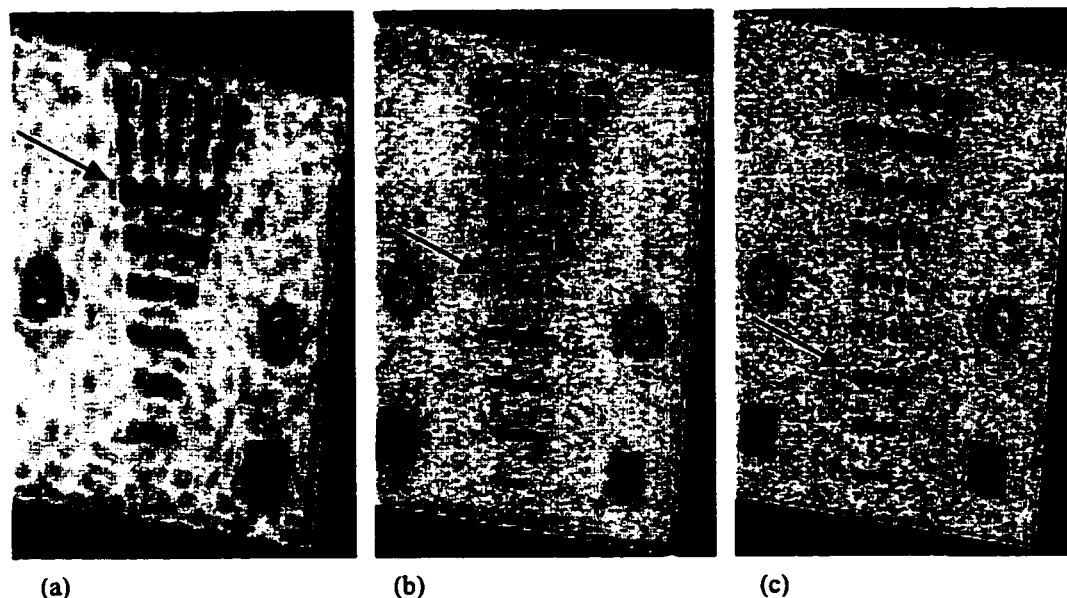


Figure 2-21 Resolution phantom images using a 3D sequence with a different number of samples in the x and y directions (a) 256×150 , TE 5ms (b) 512×230 , TE 7ms (c) 700×300 , TE 10ms (parameters for all FA 25° , TR 36ms, FOV 200mm). The definition of the small holes increases as the spatial resolution increases. Note that halving of the voxel size leads to a 50% loss in SNR, but the reduced voxel size is essential to see the small features.

To see the effect of using high spatial resolution in vivo, a 3D TOF pulse sequence was applied twice using the same parameters on the same volunteer, the first

time with 512×256 spatial resolution, and the second with 700×300 . From Fig. 2-22 it is obvious the increase in signal intensity for the small vessels and enhanced signal of the visible ones.

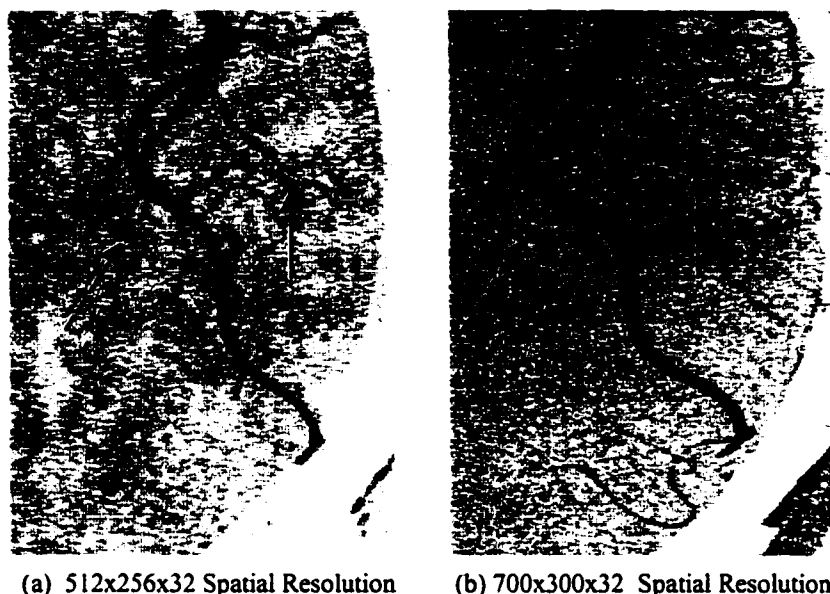


Figure 2-22 Transverse MIP of 3D TOF with different spatial resolution. (a) $512 \times 256 \times 32$ spatial resolution, TE 7ms (b) $700 \times 300 \times 32$ spatial resolution, TE 10ms (parameters for both FA 25° , TR 36ms, FOV 200mm). The utility of high resolution lies in its ability to visualize the small vessels (arrows).

Increasing the spatial resolution certainly enhances the contrast of the small vessels and the over all image quality, but achieving this is countered by the expense of increased imaging time. A set of 3D data with 256×32 views (in y and z direction) and TR 36ms needs 4.9 minutes to be collected, whereas 5.7 minutes are needed to collect 300×32 views at the same TR. Achieving the high resolution images by increasing the acquisition time is not a preferable option, since it is related to patient comfort and is time consuming, but still it is a useful tool to image the small vessels in the upper part of the head.

2.5.2. Optimizing the Flip Angle:

As we have seen in the previous section, increasing the spatial resolution can achieve better image quality, but it causes an increase in the imaging time. A second parameter independent on the imaging time is the flip angle. The 3D TOF sequence with the same parameters on the same volunteer is used to optimize the flip angle [28]. Fig. 2-23 shows three source images using different flip angles, where the 19° flip angle provides the best vessel depiction.

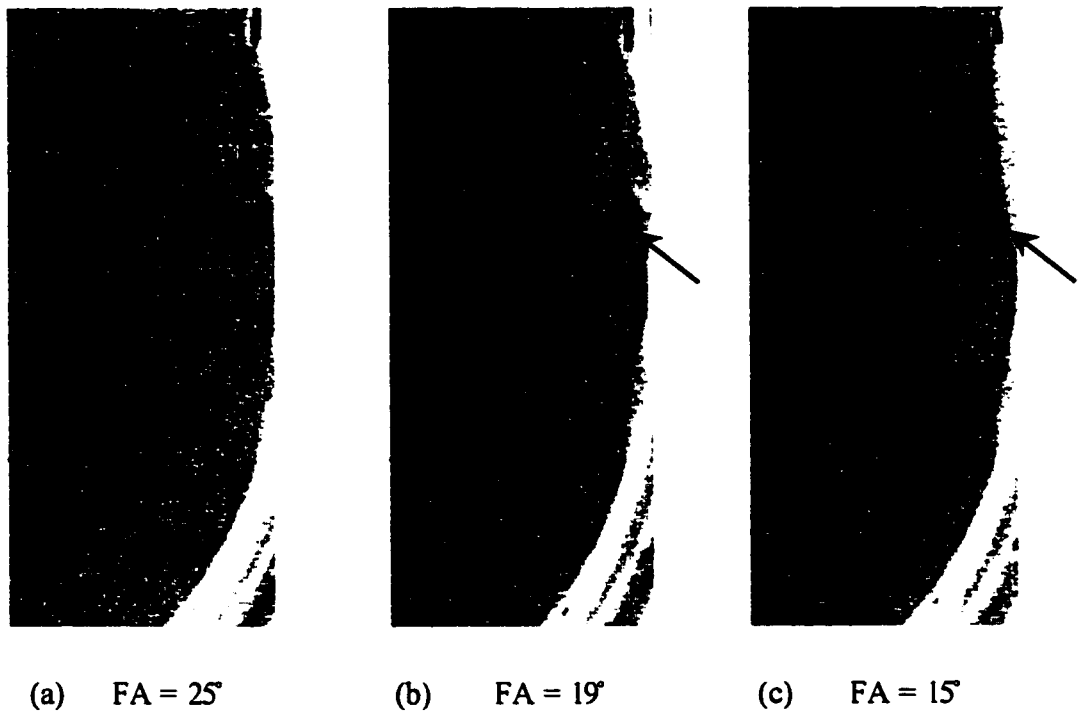


Figure 2-23 Transverse MIP of 3D TOF with the same resolution but different flip angles. (a) FA = 25° (b) FA = 19° (c) FA = 15° (parameters for all 512×256×32 spatial resolution, TR/TE= 36/7ms, FOV 200mm). Reducing the flip angle from 25° to 19° increases the visibility of small vessels (dashed arrow), on the other hand reducing it to 15° leads to signal loss from some vessels (solid arrow).

2.5.3. Adjusting TE to Produce Water/Fat Out-of-Phase:

The difference between the water and fat resonance is 220Hz at 1.5T [28] and 440Hz at 3T which can lead to addition or subtraction of fat and water depending on the echo time. At 3T the water/fat signal will be out-of-phase at the following echo times (1.14, 3.4, 5.7, and 7.9 ms) and in-phase at (2.2, 4.5, and 6.8 ms). Fig 2-24 shows three images at different echo time and how the fat signal can be suppressed which is very important when we scan the neck where there is considerable fat.

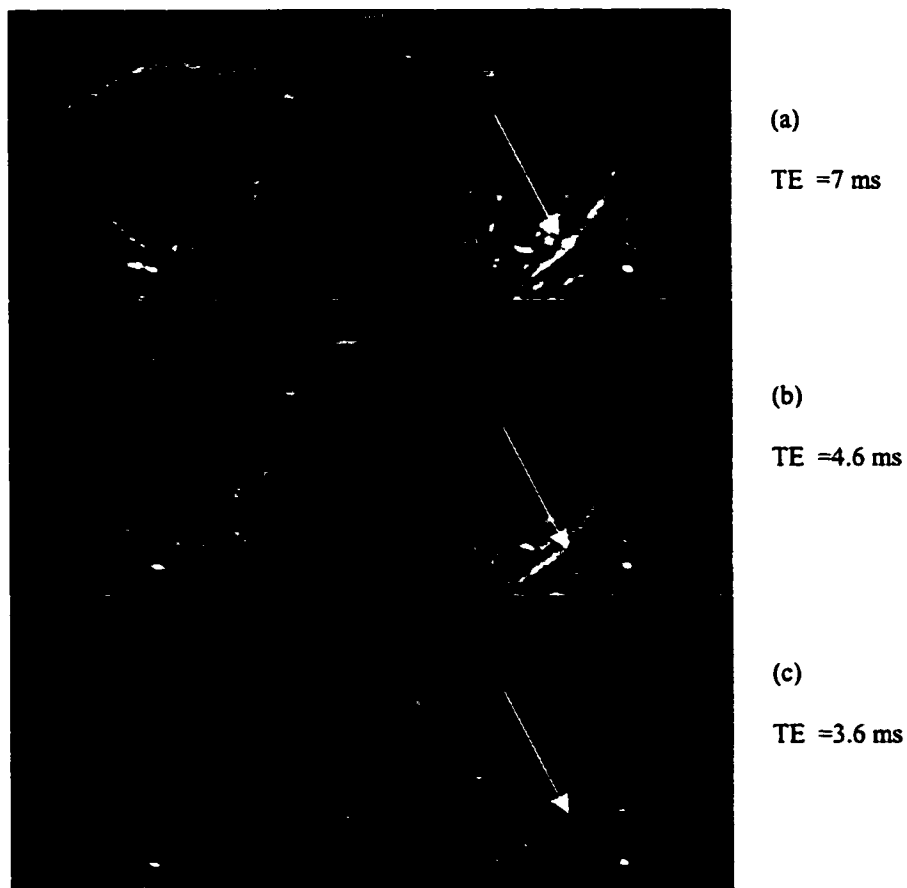


Figure 2-24 The source images for the eyes on the same volunteer at different echo times. (a, b) TE = 7 ms and 4.6 ms where water and fat are in-phase. Note the high signal from fat. (c) TE = 3.6 where the water and fat out-of-phase, now we have an acceptable suppression for the fat signal.

2.6. Comparing 1.5T with 3T using 3D TOF:

The goal of this comparison is to provide in-vivo evidence that the high field strength of 3T increases the signal intensity and contrast over medium field strength 1.5T for magnetic resonance angiography. 1.5T has been used for the last two decades by the medical and research community and it proves to be a powerful diagnostic tool for different applications. Higher field strengths have now entered the research community but their value for MRA remains unproven.

Table 2-3 shows different values of the relaxation time T1 at 1.5 and 3T for different tissues. The increase in T1 values gives the 3T the advantage of suppressing the background signal more easily from white and gray matter. Fig. 2-25 shows a theoretical plot for the blood signal and background at different field strengths using a flip angle of 25°. As the blood signal flows through the imaging volume it receives more RF pulses, while the background signal receives all the RF pulses and is at steady-state.

Tissue	T1 (ms) at 1.5 T	T1 (ms) at 3 T
Blood	1200	1500
White Matter	790	850
Gray Matter	920	1300

Table 2-3 Representative values of relaxation time T1 at 1.5 and 3T. Note increasing T1 values as the field strength increases.

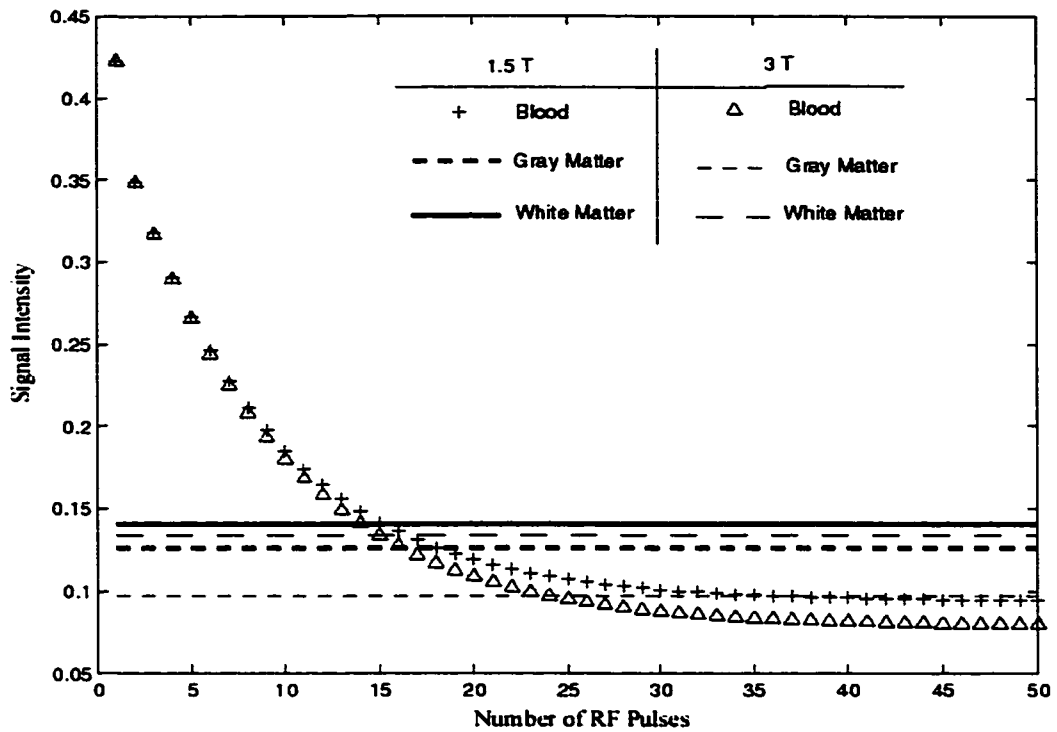


Figure 2-25 A theoretical plot for blood and background signal at different field strength. Note that the increment in T1 values at 3T produces less background signal which gives the main advantage for the higher field. FA 25° and TR 36ms.

To find out the contrast difference between 1.5 and 3T for both the gray and white matter the following equation was used:

$$\text{Contrast Difference} = \left[\frac{\text{Blood} - \text{Background}}{\text{Background}} \right]^{3T} - \left[\frac{\text{Blood} - \text{Background}}{\text{Background}} \right]^{1.5T} \quad (2-13)$$

From Fig. 2-26 it is clear how the 3T field can produce better blood-to-background contrast than 1.5T for blood vessels in gray matter, but for white matter the 1.5T gets better after applying more than 14 RF pulses. Luckily, the distal, slow flowing intracranial vessels tend to be in gray matter, making 3T preferable.

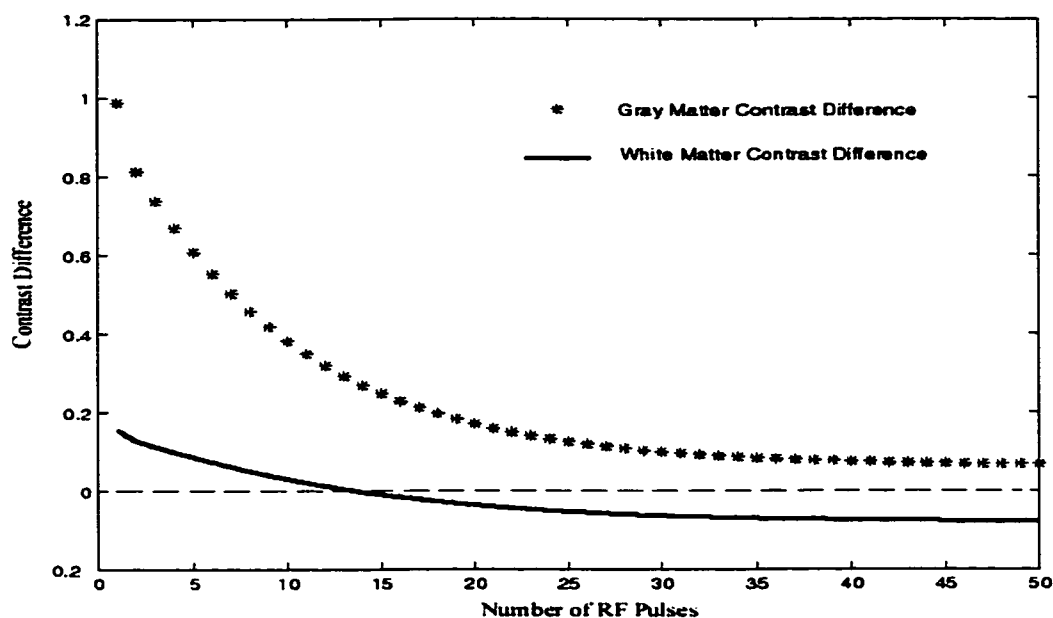


Figure 2-26 The contrast difference between the 1.5 and 3T for both the gray and white matter. Above the zero line is the advantage of 3T in having better contrast and under it is the advantage of 1.5T. FA 25° and TR 36ms.

2.6.1. 3D TOF Experiment Protocol:

The same protocol is used in both field strengths to collect the required data under similar parameters. The parameters used in this study were essentially optimized for the 1.5T clinical scanner (Siemens, Magnetom Symphony 20mT/m, Germany) and not for the 3T research scanner (SMIS, Magnex 20mT/m, UK). These parameters are 512×256×32 spatial resolution with oversampling, readout bandwidth of 41.5 kHz for Siemens and 50 kHz for SMIS, ramp pulse with FA 25°, TR/TE= 36/7ms, FOV 200mm, flow compensation in *x* and *z* directions, two slabs to cover the ROI with overlapping factor 0.38 (3 slices will overlap from each slab), saturation pulse 40mm thickness and 10mm away from the slab, slice thickness 1mm, and sequential phase encoding in both *y* and *z* directions.

The same parameters have been matched in the 3T scanner to achieve a fair comparison. However, some parameters such as the flip angle and TE were later optimized to improve the performance of 3D TOF at 3T.

The 3D TOF protocol is started by taking a sagittal image using a 2D sequence for accurate determination of the volume placement, which includes the Circle of Willis, middle cerebral artery, anterior cerebral artery as shown in Fig. 2-27.

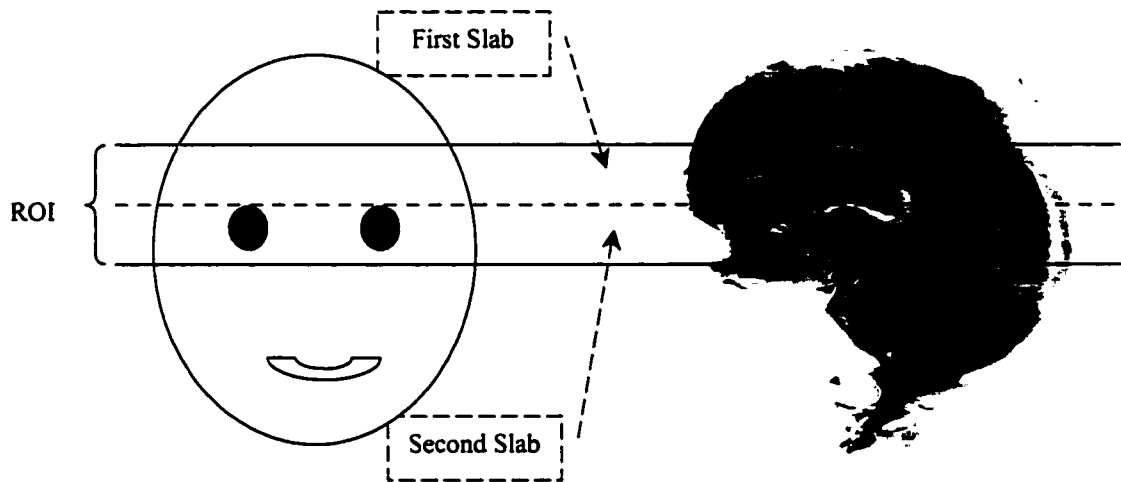


Figure 2-27 2D scout image to determine the ROI for the 3D TOF, the two slabs should cover the ROI with 3 slices overlapping from each slice.

After determining the volume of interest, shimming is performed to maximize the signal intensity over the entire ROI, then both ramp and saturation pulses are optimized to the RF flip angles. After collecting the data from two slabs the image reconstruction is performed using the same pre-scaling values in order to produce a normalized set of images. The 1.5T images are converted to the SMIS image display format for further analysis keeping the same intensity scale.

2.6.2. Experimental Results for 1.5T vs 3T:

The experiments were performed on the same seven volunteers, at both field strengths, with the parameters kept as identical as possible. At 1.5T two sets of data were collected, first one without magnetization transfer (MT) and the second with MT to suppress the background signal more effectively [27] [35]. Whereas at 3T only one set of data was collected without MT, because of concerns over patients heating if MT was used.

Table 2-4 shows measurements of the middle cerebral artery which include signal-to-noise, normalized contrast, and contrast-to-noise. The data clearly demonstrate that the 3T field strength provides higher signal and contrast than the 1.5T which will enhance the overall quality of the images.

	3T			1.5T without MT		
<i>Volunteer</i>	SNR	C	CNR	SNR	C	CNR
Case 1	83	6.9	75.1	42	2.9	33.5
Case 2	81	6.7	66.6	53	2.52	38.9
Case 3	59	4.5	46.2	51	2.66	32.8
Case 4	55	5.4	41.7	59	2.8	41.9
Case 5	61	5.2	50.4	36	2.08	24.1
Case 6	67	4.4	62.9	46	1.66	31.7
Case 7	70	6.3	58.9	51	2.26	38.4

Table 2-4 This table demonstrates the signal measurements of the middle cerebral artery. The measurements were made on the same locations in the source images and their MIPs. The tremendous improvement in SNR and CNR at 3T can be seen compared to 1.5T.

Table 2-5 shows the same 3T measurements but compared to 1.5T using MT. It is clear that the MT pulse enhances the background suppression at 1.5T [36] and increases the contrast between the blood and background which enables the small vessels to be visible.

	3T			1.5T with MT		
<i>Volunteer</i>	SNR	C	CNR	SNR	C	CNR
Case 1	83	6.9	75.1	41	3.4	33.3
Case 2	81	6.7	66.6	52	3.4	40.7
Case 3	59	4.5	46.2	48	3.1	31.8
Case 4	55	5.4	41.7	57	3.3	41.6
Case 5	61	5.2	50.4	38	2.4	23.5
Case 6	67	4.4	62.9	39	2.1	29.4
Case 7	70	6.3	58.9	45	2.9	37.0

Table 2-5 This table demonstrates the signal measurements of the middle cerebral artery after using MT at the 1.5T. Note that the contrast between the blood and background increases comparing with the previous table, without using MT.

Table 2-6 shows the average measurements from seven volunteers of the middle cerebral artery following 3D TOF at 1.5 and 3T.

<i>Measurements</i>	1.5 T without MT	1.5 T with MT	3T	3T advantage (ratio without MT)
SNR	48 ± 7	46 ± 7	68 ± 11	1.4
C	2.4 ± 0.4	2.9 ± 0.5	5.6 ± 1.0	2.3
CNR	34 ± 6	34 ± 7	57 ± 12	1.7

Table 2-6 The average measurements and standard deviations from seven volunteers. Note the big increment in the C and CNR at the 3T comparing with 1.5T. The 3D advantage is defined as (1.5T without MT / 3T).

Fig. 2-28 shows the coronal and sagittal views for the same volunteer, case #2, at both field strengths, where the signal intensity looks higher on the high field strength which enables better visualization for the small vessels.

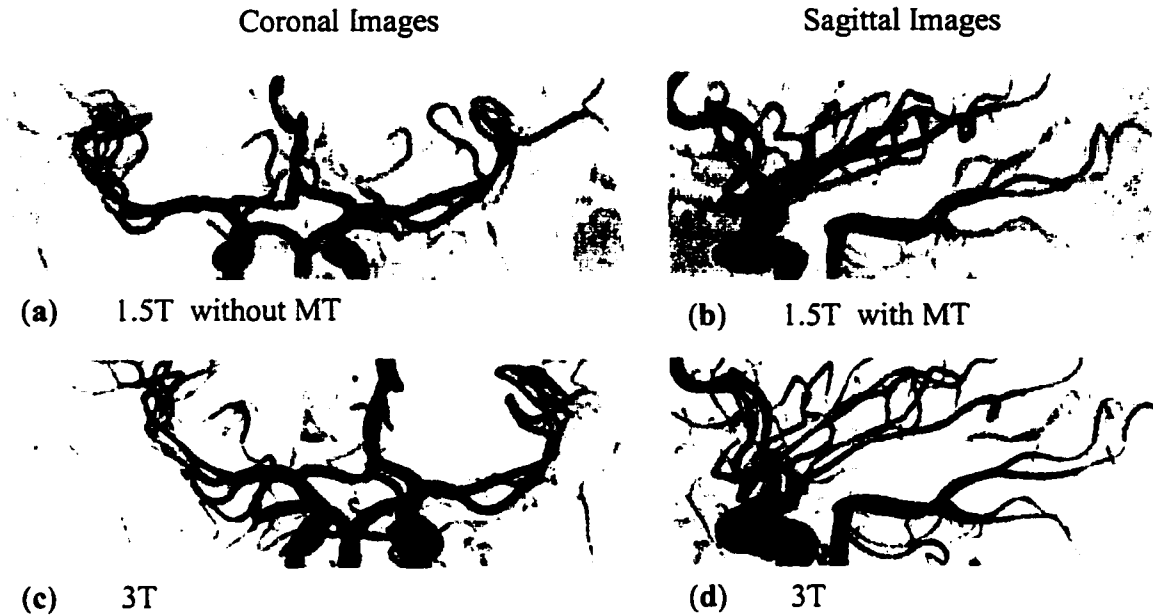
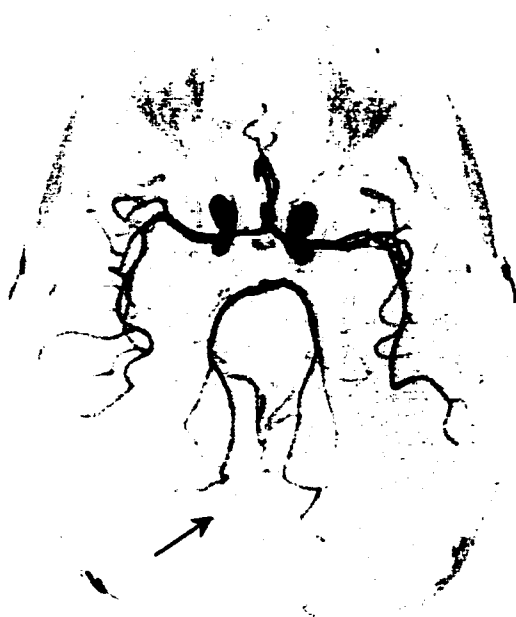


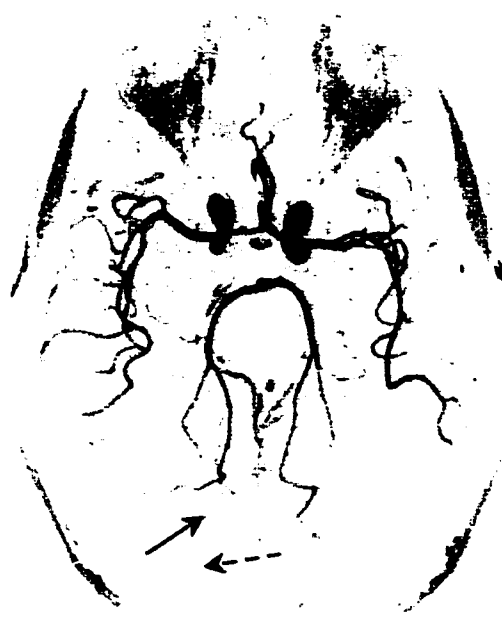
Figure 2-28 Coronal and sagittal views for the Circle of Willis for the same volunteer, case #2. (a, b) at 1.5T. (c, d) at 3T. Note the high signal intensity at the higher field.

Figures. 2-29 and 2-31, for case #2 and #7, respectively, show the maximum intensity projection images where (a) is the MIP at 1.5T without MT, (b) at 1.5T with MT, and (c) at 3T without MT. Note the effect of using MT on the background suppression (a vs. b), where the thin vessels become visible. The background suppression is higher at the higher field which enhances the visibility of the thin vessels and the overall quality of the image. Figs. 2-30 and 2-32, for case #2 and #7 respectively, show the individual source images at both field strengths where the effect of MT appears clearly in suppression of the background signal at 1.5T. But still the higher field offers higher contrast due to increasing T1 values of different tissues which enhance the contrast between tissue and blood [37].

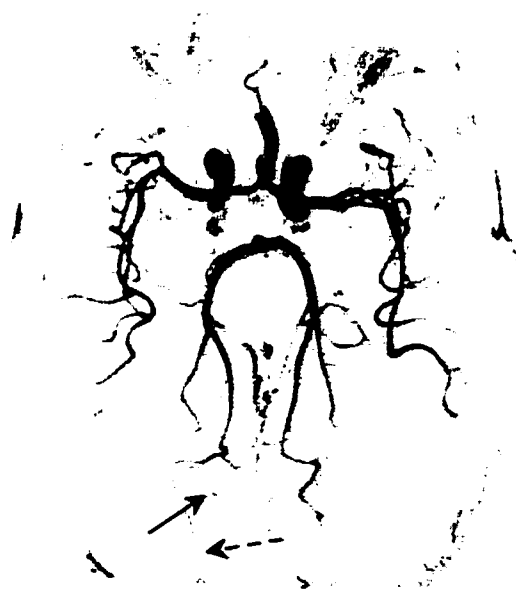
(a) 1.5T without MT



(b) 1.5T with MT



(c) 3T without MT

Parameters:

512×256×32 resolution

FA 25°

TR / TE= 36/7ms

FOV 200mm

1mm slice thickness

Figure 2-29 MIP images for the Circle of Willis in the same volunteer, case #2, at different field strengths. (a) At 1.5T without MT (b) at 1.5T with MT. Note the background suppression that enhances the appearance of the thin vessels (solid arrow). (c) At 3T. Note the high signal intensity at 3T compared with 1.5T and the better background suppression even without using MT which enables the visibility of the vessels ends (dashed arrows).

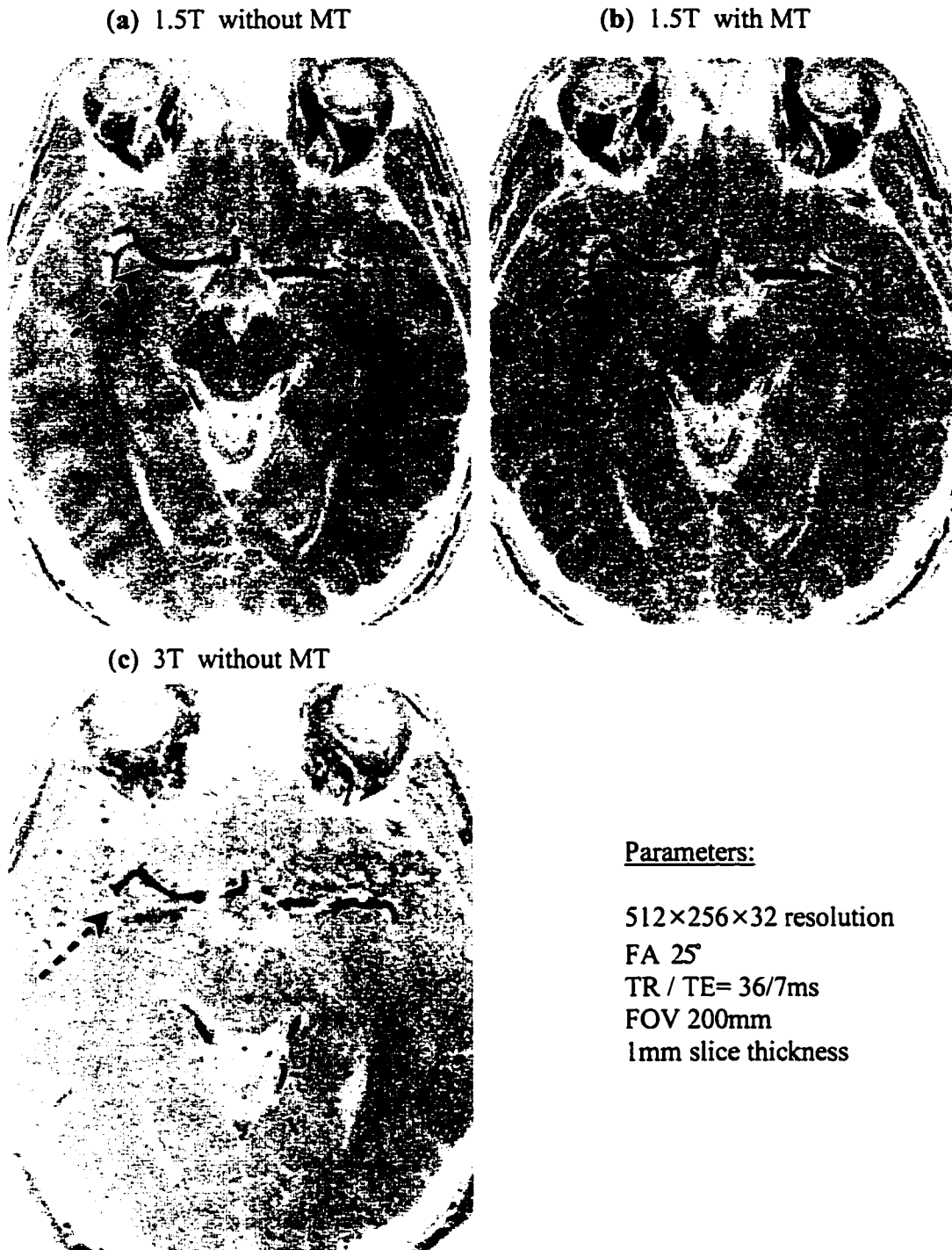
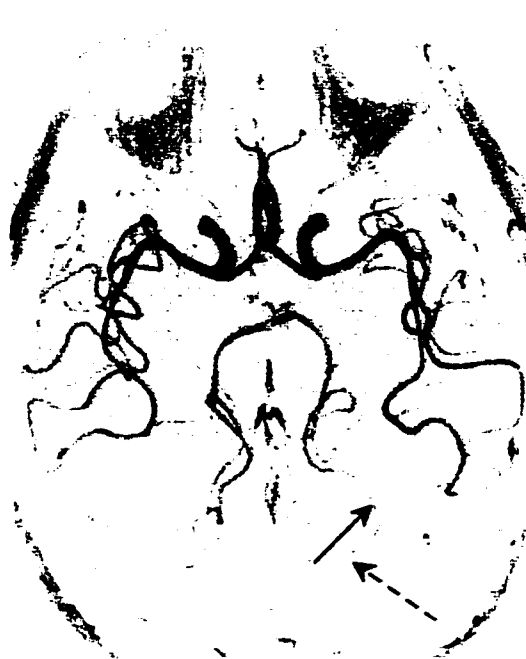


Figure 2-30 The individual source images at both field strengths, for case #2. (a) At 1.5T without MT (b) at 1.5T with MT. Note the background suppression. (c) At 3T. Note the better background suppression even without using MT. Also note at the high field the pulsatile artifact appears clearly (dotted arrow).

(a) 1.5T without MT



(b) 1.5T with MT



(c) 3T without MT

Parameters:

512×256×32 resolution

FA 25°

TR / TE= 36/7ms

FOV 200mm

1mm slice thickness

Figure 2-31 MIP images for Circle of Willis in the same volunteer, case #7, at different field strengths. See Fig. 2-29 caption for details.

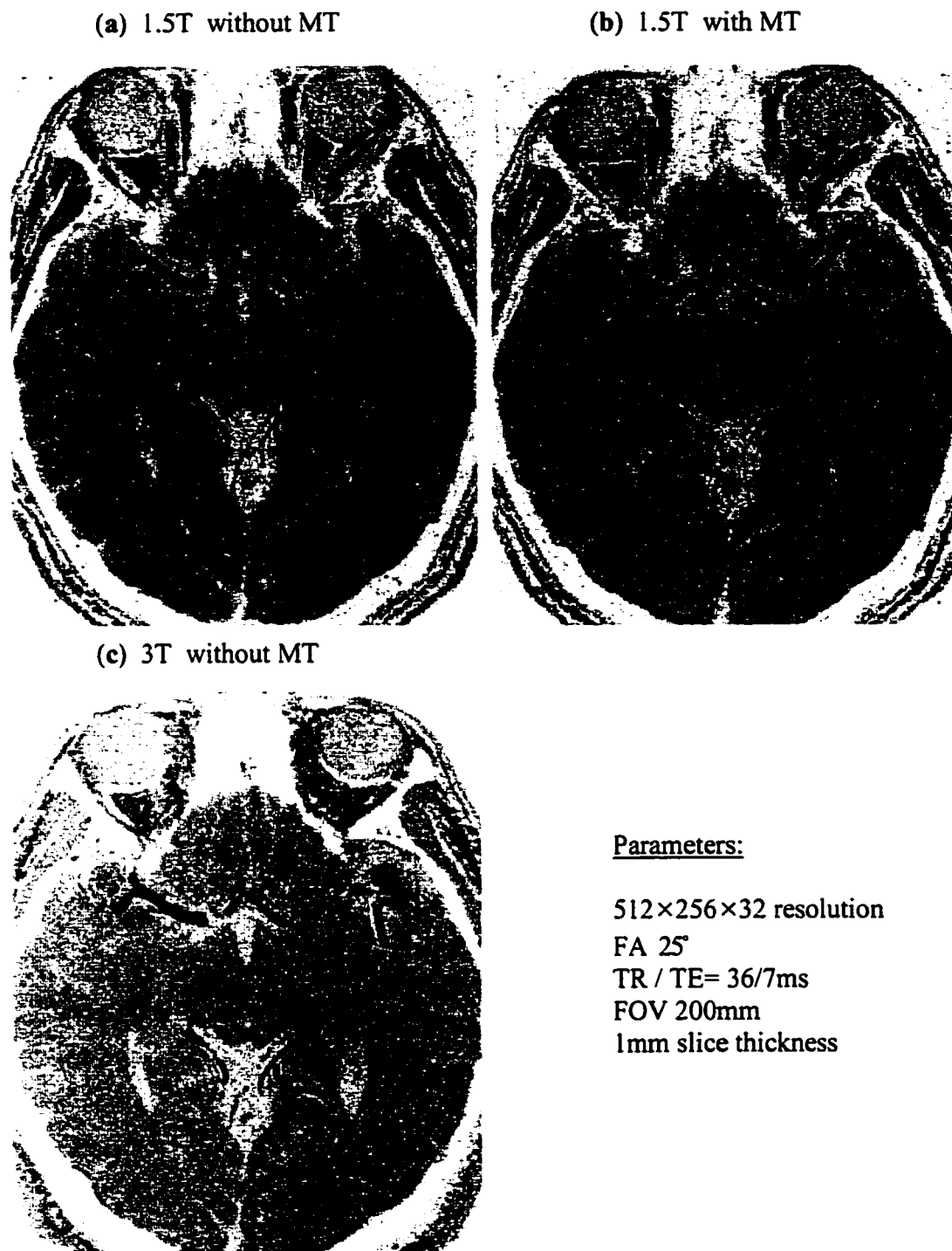


Figure 2-32 The individual source images at both field strengths, for case #7. (a) At 1.5T without MT (b) at 1.5T with MT. Note the background suppression. (c) At 3T. Note the overall background suppression even without using MT.

2.7. Conclusion:

Time of flight MRA is emerging as a powerful clinical tool. Both 2D and 3D sequences can be used. Limitations in 2D TOF include: long TE needed to excite a thin slice that yields more flow phase effect than would happen in 3D, lower SNR, and limited slice resolution. The 3D sequence can overcome these limitations. Using flow compensation with 2D and 3D TOF proves to be useful in reducing the signal loss due to the uncompensated effects of velocity. The main disadvantage of the 3D sequence is the high sensitivity for motion where any motion during the scan can affect the entire results, while in 2D sequence the motion might affect only one or more slices.

The comparison study between 1.5T and 3T indicates that the high field strength has the advantages of increasing SNR and increased T1 times:

- 1- MRA sequences can benefit from the increased SNR available in high field strength [37]. Although a 2 fold increase was expected, we found 1.4 in our study. We expect the poorer increase relates to lack of an RF shielded room at 3T.
- 2- Increasing T1 values of different tissue with the field strength will allow better contrast between tissue and blood [38]. We measured the blood-to-background contrast to be 2.3 times more at 3T, and the contrast-to-noise ratio was 1.7 times more at 3T (Table 2-6).

More ghosting was visible at 3T due to pulsation artifacts; we expect that reducing TE could reduce these artifacts at 3T.

2.8. References:

1. Haacke, E.M., *Magnetic Resonance Imaging, physical principles and sequence design*. 1999: John Willey & Sons.
2. Haase, A., *Applications to T1, T2, and chemical shift imaging*. J Magn Reson, 1990. **13**: p. 77-89.
3. Suryan, G., *Nuclear resonance in flowing liquids*. Proc Indian Acad Sci, 1951. **33**(107-111).
4. Singer, J.R., *Blood flow rates by nuclear magnetic resonance measurements*. Science, 1959. **130**: p. 1652-1653.
5. Morse, O.C. and J.R. Singer, *Blood velocity measurement in intact subject*. Science, 1970. **170**: p. 440-441.
6. Keller, P.J., et al., *MR angiography with two-dimensional acquisition and three-dimensional display*. Radiology, 1989. **173**: p. 527-532.
7. Brown, M.A., *MRI Basic Principles and Applications*. 1995: John Wiley & Sons.
8. Dumoulin, C.L., et al., *Three-dimensional time-of-flight magnetic resonance angiography using spin saturation*. Magn Reson in Med, 1989. **11**: p. 35-46.
9. Dumoulin, C., *Rapid scan magnetic resonance angiography*. Magn Reson Med, 1987. **5**: p. 238-245.
10. Edelman, R.R., et al., *Quantification of blood flow with dynamic MR imaging and presaturation bolus tracking*. Radiology, 1989. **171**: p. 551-556.

11. Nishimura, D.G., *et al.*, *Magnetic resonance angiography by selective inversion recovery using a compact gradient echo sequence*. Magn Reson Med, 1988. 8: p. 96-103.
12. Wilman, A.H., J. Huston, and S.J. Riederer, *Three-dimensional magnetization-prepared time-of flight MR angiography of the carotid and vertebral arteries*. Magn Reson Med, 1997. 37: p. 252-259.
13. Grover, T. and J.R. Singer, *NMR spin-echo flow measurement*. J Appl Physics, 1971. 42: p. 938-940.
14. Freeman, R., *Shaped radiofrequency pulses in high resolution NMR*. J. of Progress in NMR Spectroscopy, 1998. 32: p. 59-106.
15. Schmalbrock, P., *Volume MR angiography: methods to achieve very short echo times*. Radiology, 1990. 175: p. 861-865.
16. MacFall, J.R., N.J. Pelc, and R.M. Vavrek, *Correction of spatially dependent phase shifts for partial Fourier imaging*. Magn Reson Imaging, 1988. 6: p. 143-155.
17. Haake, E.M., *A fast iterative partial fourier technique capable of local phase recovery*. J Magn Reson, 1991. 92: p. 126-145.
18. Haacke, E.M., *et al.* *High resolution 2D and 3D gradient-field-echo functional imaging correlated with high resolution MRA*. in *Functional MRI of the Brain, A Workshop presented by the SMRM and the SMRI*. 1993. Washington, DC.
19. Weisskoff, R.M., A.P. Crawley, and V. Wedeen. *Flow sensitivity and flow compensation in instant imaging*. in *Abstracts of the SMRI*. 1990. New York.

20. Brown, D.G. and S.J. Riederer, *Contrast-to-noise ratios in maximum intensity projection images*. Magn Reson in Med, 1992. **23**: p. 130-137.
21. Carlson, J., *et al.*, *Signal-to-noise ratio and section thickness in two-dimensional versus three-dimensional Fourier Transform MR imaging*. Radiology, 1988. **166**: p. 266-270.
22. Parker, D.L. and G.T. Gullberg, *Signal-to-noise efficiency in magnetic resonance imaging*. Med Phys, 1990. **17**: p. 250-257.
23. Reeder, S.B. and E.R. McVeigh, *The effect of high performance gradients on fast gradient echo imaging*. Magn Reson Med, 1994. **32**: p. 612-621.
24. Edelstein, W.A., *et al.*, *Signal, noise, and contrast in nuclear magnetic resonance (NMR) imaging*. J Comput Assist Tomogr, 1983. **7**: p. 391-401.
25. Hutchison, J.M., *NMR imaging: image recovery under magnetic fields with large nonuniformities*. J. Phys. E.: Scient. Instrum., 1978. **11**: p. 217.
26. Kaufman, L., *et al.*, *Measuring signal-to-noise ratios in MR imaging*. Radiology, 1989. **173**(1): p. 265-267.
27. Atkinson, D.J., *et al.*, *Improved MR angiography:magnetization transfer suppression with variable flip angle excitation and increased resolution*. Radiology, 1994. **190**: p. 890-894.
28. Nagele, T., *The effect of linearly increasing flip angles on 3D inflow MR angiography*. Magn Reson Med, 1994. **31**: p. 561-566.
29. Potchen, E., *et al.*, *Magnetic Resonance Angiography: Concepts and Applications*. 1993, St. Louis: Mosby.

30. Vinitsky, S., *et al.*, *Effect of sampling rate on magnetic resonance imaging*. Magn Reson in Med, 1987. 5: p. 278-282.
31. Parker, D.L., C. Yuan, and D.D. Blatter, *MR angiography by multiple thin slab 3D acquisition*. Magn Reson in Med, 1991. 17: p. 434-451.
32. Blatter, D.D., *Cerebral MR angiography by multiple thin slab 3D acquisition*. Radiology, 1991. 179: p. 805-811.
33. Lewin, J.S., G. Laub, and R. Hausmann, *Three-Dimensional Time-of-Flight MR Angiography: Applications in the Abdomen and Thorax*. Radiology, 1991. 179: p. 261-264.
34. Frahm, J., K. Merboldt, and W. Hanicke, *Functional MRI of human brain activation at high spatial resolution*. Magn Res Med, 1992. 29(1): p. 139-144.
35. Li, D., *et al.*, *Coronary arteries: three-dimensional MR imaging with fat saturation and magnetization transfer contrast*. Radiology, 1993. 187: p. 401-406.
36. Pike, G.B., *et al.*, *Magnetization transfer time-of-flight magnetic resonance angiography*. Magn Reson Med, 1992. 25: p. 372-379.
37. Lee, J.H., *High contrast and fast three dimensional magnetic resonance imaging at high fields*. Magn Reson Med, 1995. 34: p. 308-312.
38. Kim, S.G., *Accurate T1 determination from inversion recovery imaging: application to human brain at 4 Tesla*. Magn Reson Med, 1994. 31: p. 445-449.

CHAPTER 3

Experimental Contrast Curve Design for Testing Different Acquisition Techniques in 3D CE MRA

3.1. Introduction:

Contrast enhanced (CE) MRA employs an intravenously injected contrast agent [1]. This agent will significantly shorten T1 of the blood, which in turn will enhance the intensity of the MR signal from the blood, but only for a transient time. The start time of data acquisition is critical to make use of the contrast agent to enhance the arterial signal but also to limit the venous signal. This is difficult since the MRA acquisition requires 20-40 sec to acquire a 3D data set while the veins may enhance just a few seconds after the arteries.

New data acquisition techniques have made use of reordering *k*-space in different manners to improve image quality and reduce the artifacts when a contrast agent is used. This chapter describes four different encoding techniques and their method of reordering *k*-space. These techniques have been implemented in a 3D contrast enhanced sequence. An experimental contrast curve has been implemented to perform a quantitative comparison among three different data acquisition techniques using a 3D CE sequence.

These results were compared to a computer simulation performed under the same conditions.

3.2. Data Acquisition Techniques:

Different data acquisition techniques are used for different applications in MRA. In all cases, most of the signal comes from sampling the data near the center of k -space [2]. Fig. 3-1 shows the effect on the resulting image quality of limiting the acquisition to central regions of k -space [3] [4].

In our study four different data encoding techniques are introduced to collect the data along both phase encoding directions in a 3D scan: sequential, centric, elliptical centric, and elliptical sequential. These phase encoding orders will be described later in this chapter.

Some works have been performed comparing different encoding techniques for 3D CE MRA. For example, Maki [5] compared centric to sequential using only a single dimension of phase encoding. Ito [6] explained the k -space filtering effects on 3D CE MRA for sequential encoding. Wilman [7] studied the differences between the elliptical centric technique and other phase encoding orders for 3D CE MRA, where the centric acquisition would be preferable. In this study we introduce the first quantitative comparison that examined all commonly used competing techniques supported with computer simulation under the same conditions.

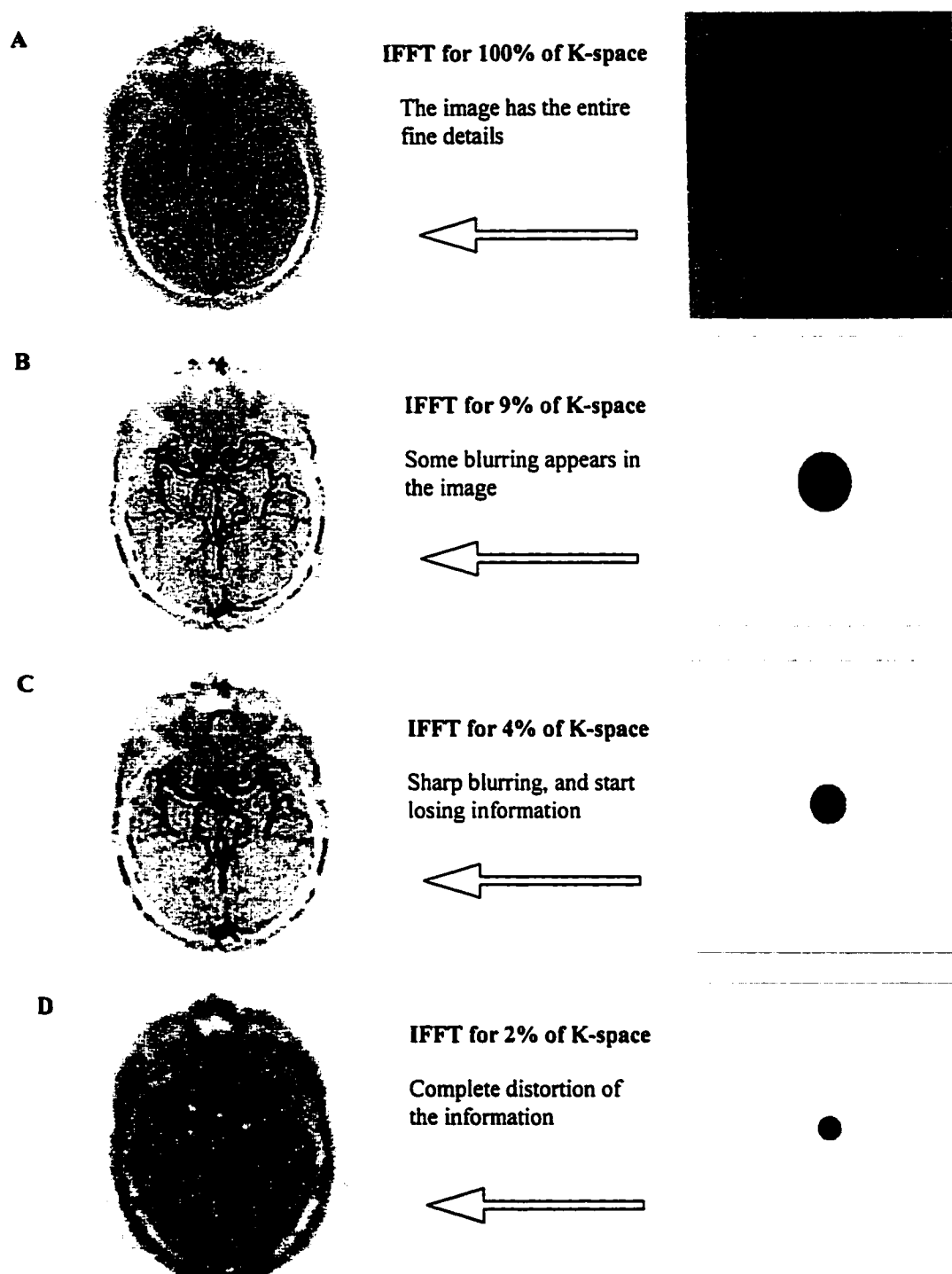


Figure 3-1 The effect of inverse fast Fourier transform on image quality when different centric parts from k-space are chosen. Note a complete distortion of the information in (D).

3.2.1. Sequential Encoding Technique:

This encoding technique is widely used, where complete coverage of k -space is performed in a sequential manner. Fig. 3-2 illustrates how the data encoding starts from the first slice first line then second line... etc, till the first slice is completely encoded; then move to the second slice first line and so on. The rest of the slices will be encoded in the same way [8]. Contrast between tissues depends mainly on the central part of k -space. The sequential technique covers the center part of k -space in the middle of the scan.

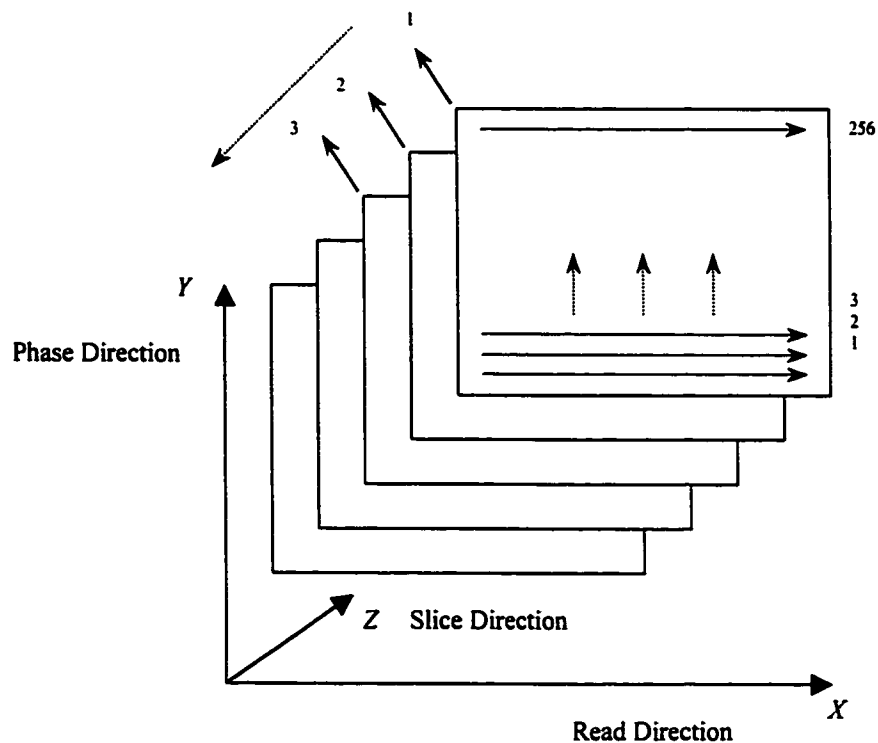


Figure 3-2 Sequential encoding for k -space where we start from the first slice first line, then the second line till the entire slice is scanned, then moving into the second slice with the same encoding method.

The transverse magnetization must be brought into a steady-state condition in order to avoid any ringing effect that might accompany the high signal in the center of k -space. This problem can be removed if a number of pulse sequence waveforms are applied without collecting data (dummy scans) to stabilize the condition before the data are collected. This encoding technique is used in 3D contrast enhanced MRA to capture the first pass of the contrast agent (Ch. 4).

3.2.3. Elliptical Centric Encoding Technique:

In this technique data are collected by starting at the center of k -space and moving out toward the edges of k -space for the y - z directions, increasing the k -space radii in the phase encoding plane as time increases, as shown in Fig. 3-4 and Fig. 3-5. This technique collects the important part of k -space first in the shortest time possible [7].

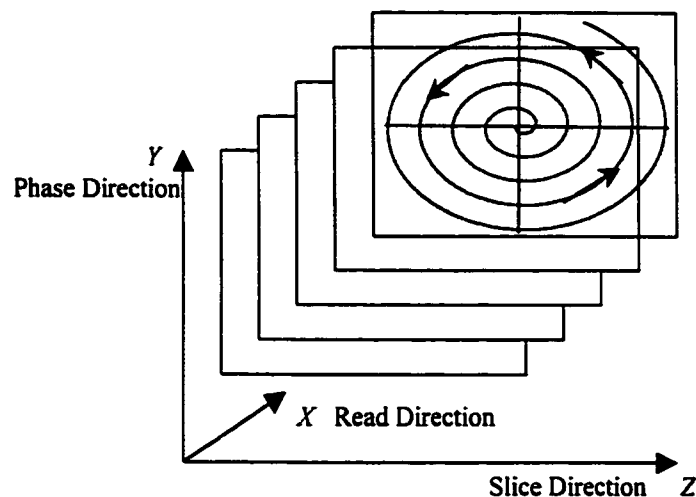


Figure 3-4 Elliptical centric encoding where we start from the center of k -space toward the edges as time increases.

Fig. 3-5 is drawn to illustrate this encoding scheme in the phase encoding plane (y - z directions). Since the SMIS Pulse Programming Board does not have the ability to process large matrix sizes, all the gradient values for this matrix were first calculated using a Matlab™ program. This matrix contained all of the trapezoidal waveforms for each gradient phase encoding. After that the matrix was saved on the Waveform Editor as seen in Fig. 3-6, then played out in the pulse sequence using the MR3040-output command, because the main control board can only handle 64 Kbytes of compiled data at once. In addition, limitations in the 3040 board caused use of only 34 K points in total. To maximize use of points, only 4 points were used on each ramp of the trapezoid.

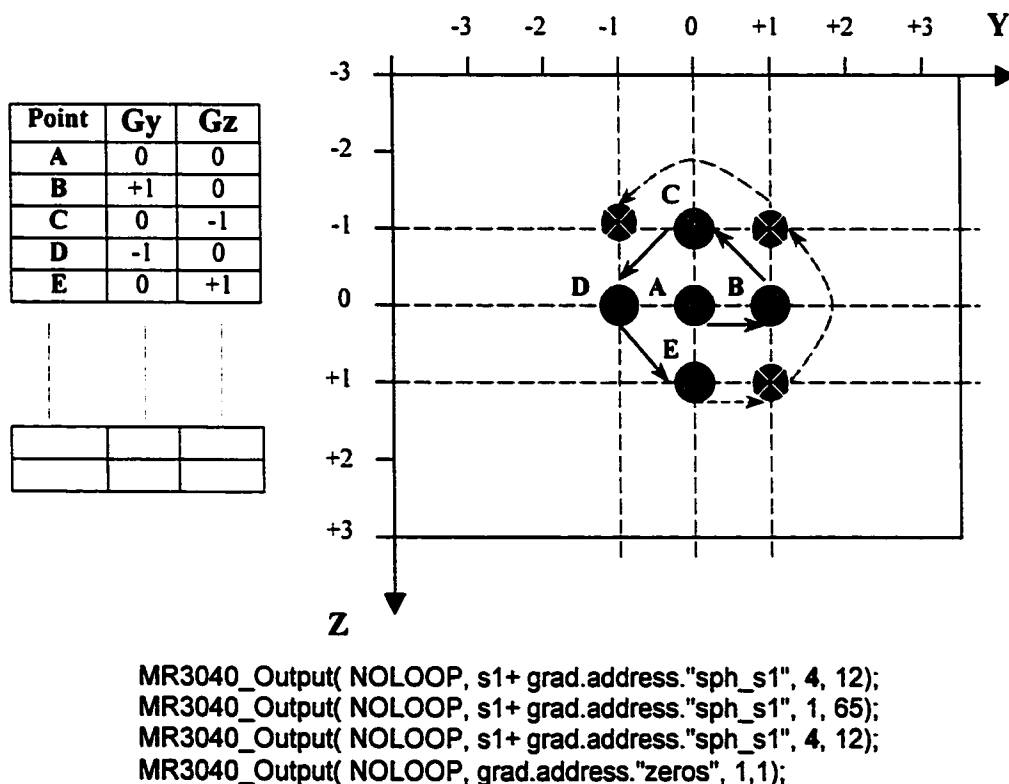


Figure 3-5 Illustration for elliptical centric encoding scheme where we start from the center of k -space toward the edges and saving the gradient values in a special matrix. Also the output commands used to play out these values from the PPL files is shown. Note that only 4 points were used on each of the trapezoid (bold letter).

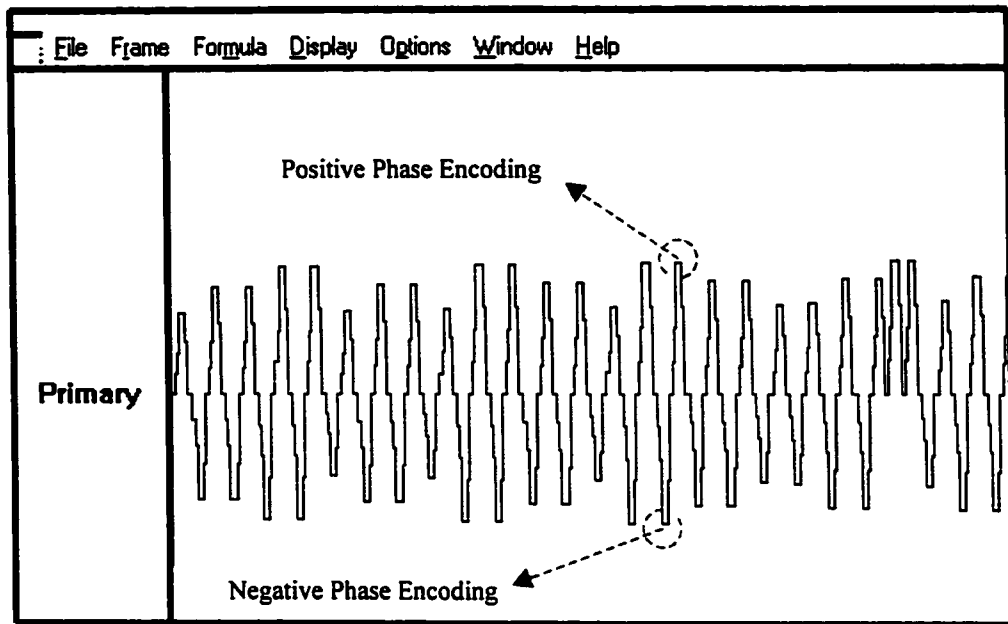


Figure 3-6 Saving the gradient values in the Waveform Editor to implement the elliptical centric encoding, where each peak represents a certain gradient value. Note that limitation on 3040 board caused use of only 4 points on each ramp of the trapezoid.

This technique offers the advantages of less motion artifact [7] and acquiring the data at the first pass of the contrast agent to have better venous suppression.

3.2.4. Elliptical Sequential Encoding Technique:

This technique depends on dividing k -space into two parts and sampling each one in a different manner, in order to locate the important information from the sample around the center of k -space. Fig. 3-7 shows how the first half of k -space is encoded starting from the edge toward the center, reducing k -space radii, with sequential fashion. While the second half is encoded in the opposite way from the center toward the edge, increasing k -space radii, with elliptical fashion.

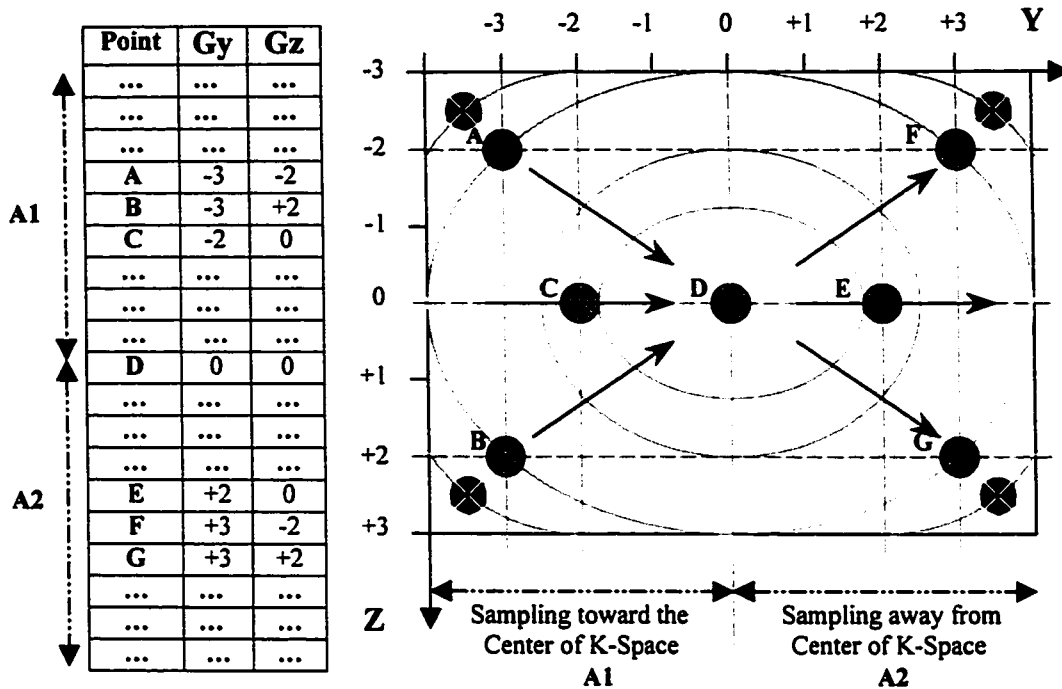


Figure 3-7 Splitting k -space into two parts and encoding each one using a different encoding technique to reserve the important information from the sample around the center of k -space.

Also in this technique the Matlab™ program was used to calculate the accurate gradient values which were saved in the Waveform Editor. This technique acquires the most central k -space views in the middle of the scan, but unlike sequential encoding the central views are acquired extremely compactly.

3.3. Experimental Comparison among Different Data Acquisition Techniques:

The effects of different encoding techniques (sequential, centric, and elliptical) on image quality in 3D contrast-enhanced MRA were evaluated experimentally [10]. Since a contrast agent produces a high signal for only a short time (will be explained in Ch4), it is

important to ensure that the center of the phase encoding plane in k -space is acquired at maximum arterial contrast [5], as shown in Fig. 3-8.

Choosing a time of flight method to test these encoding techniques would not give obvious evidence of their importance, since magnetization does not have big changes when constant agent flows into a region of interest.

In contrast enhanced MRA the contrast agent enhances the signal from both artery and vein when it passes through a region of interest. The purpose of this comparison is to prove experimentally that certain techniques can provide higher image quality by encoding the arterial signal before venous enhancement. The results were compared to a computer simulation under the same conditions [11].

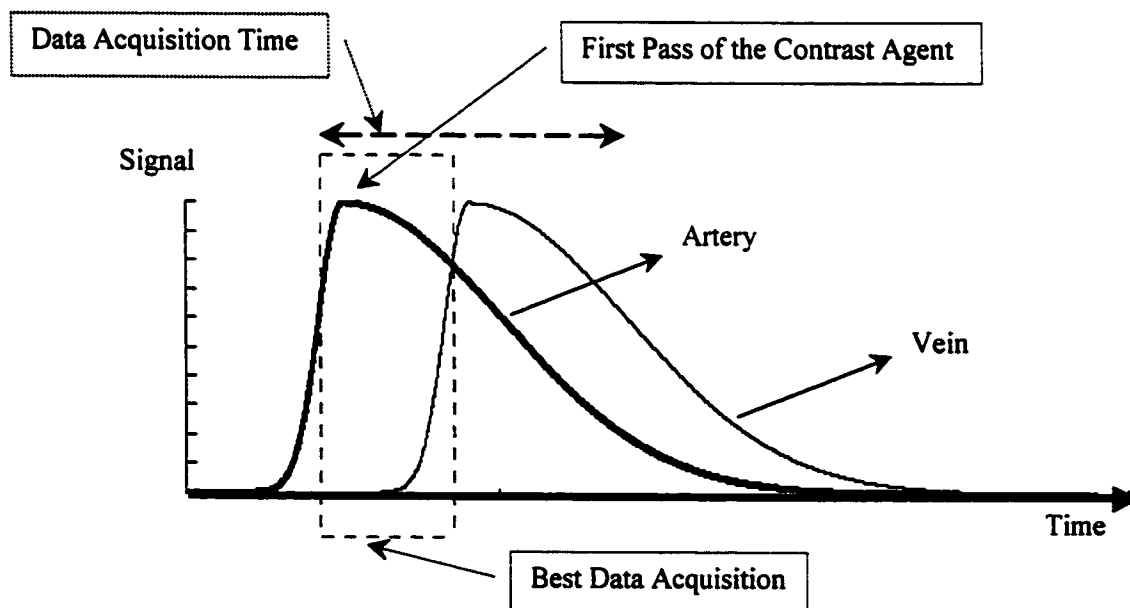


Figure 3-8 Producing high signal from the first pass of the contrast agent. Note the vein enhancement after the blood returns back to the region of interest. The dashed box indicates the best area to be encoded in the center of k -space, where the vein enhancement is not yet existing.

3.3.1. Experimental Contrast Curve Design:

Prior to proceeding to in-vivo trials, it is necessary to examine the different encoding techniques not only in computer simulations, but also in an experimental setting. For 3D contrast enhanced MRA, the appropriate experimental design is usually a flow phantom with capability for contrast injection. In this way, the degree of contrast enhancement is somewhat similar to in-vivo conditions.

However, to ensure precise repeatability, a power injector must be used with computerized control from the pulse sequence and the flow phantom must consistently output exactly the same flow characteristics. In addition the complete flowing system must be flushed of the entire contrast agent between trails. Moreover, to exactly duplicate the contrast waveform, each trial must make use of all the dose expected under in-vivo conditions. When numerous methods must be tested at different starting timepoints of a contrast curve, experimental testing becomes both an expensive and time consuming task.

Therefore, in this study we introduce a new method to produce this contrast enhancement curve during data acquisition in real time [10]. This method depends on shaping the available signal intensity to match a theoretical contrast enhancement curve by varying the flip angle throughout the 3D acquisition. Changing the flip angle was introduced for the first time for magnetization prepared sequences to eliminate blurring and artifacts by Mugler [12].

From Fig. 3-9 we can see how the transverse magnetization is changing with the available magnetization after applying a certain flip angle α :

$$M_{xy^2} = M_z^{\alpha 2} \sin(\alpha 2) \quad (3-1)$$

$$M_{xy^1} = M_z^{\alpha 1} \sin(\alpha 1) \quad (3-2)$$

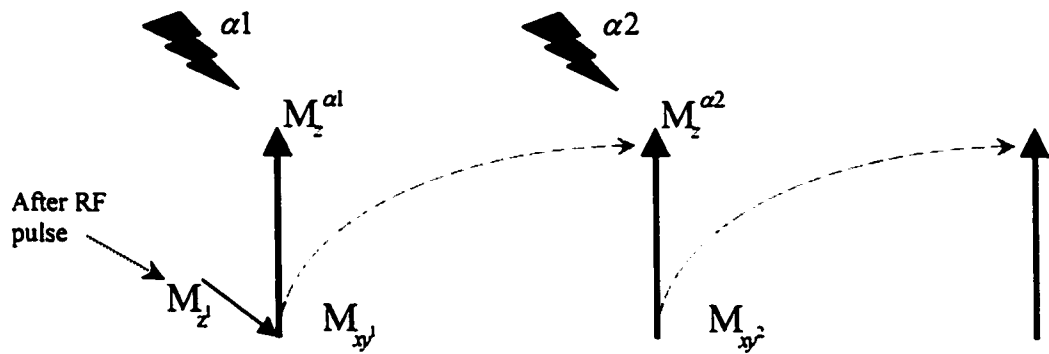


Figure 3-9 Changing the transverse magnetization by applying different flip angles.

From the Bloch equation at the steady state condition we can write:

$$M_z^{\alpha 2} = M_0 - (M_0 - M_z^1) e^{-TR/T1} \quad (3-3)$$

where M_0 is the original longitudinal magnetization, and $T1$ the longitudinal relaxation.

The angle between the longitudinal and transverse magnetization, as shown in Fig. 3-10, can be expressed as:

$$\tan(\alpha 1) = \frac{M_{xy1}}{M_{z1}} \quad (TE = 0) \quad (3-4)$$

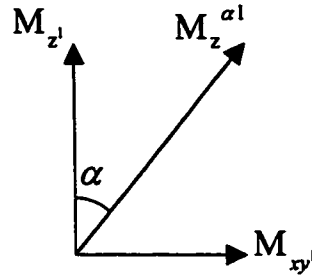


Figure 3-10 The relationship between the longitudinal and transverse magnetization.

By substituting Eq. (3-4) and (3-3) in (3-1) we get:

$$M_{xy2} = \left\{ M_0 - \left(M_0 - \frac{M_{xy1}}{\tan(\alpha 1)} \right) e^{-TR/T1} \right\} \sin(\alpha 2) \quad (3-5)$$

After further refining we find that the second flip angle is a function of some parameters $\alpha 2(M_{xy2}, M_{xy1}, TR, T1, \alpha 1)$, assuming perfect RF spoiling, as the following:

$$\sin(\alpha 2) = \frac{M_{xy2}}{M_0 (1 - e^{-TR/T1}) + \frac{M_{xy1}}{\tan(\alpha 1)} e^{-TR/T1}} \quad (3-6)$$

From this equation and using the known phantom $T1 = 30$ ms, and $TR = 40$ ms the flip angle distribution was calculated and loaded into the RF Waveform Memory of the scanner to play out the contrast curve during data acquisition. Fig. 3-11 shows the

experimental reproduced contrast curve using the variable flip angles scheme and the theoretical contrast curve resulting from Eq. (3-5).

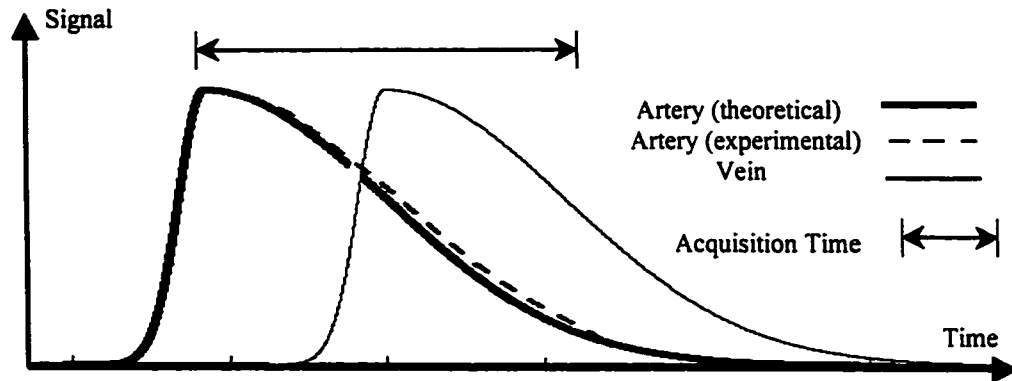


Figure 3-11 Experimental and theoretical contrast curve; the experimental data was collected by turning off all phase encoding in the 3D pulse sequence. Note the close agreement between them. Shifting the curve of the artery produced the vein. The maximum flip angle that corresponds to the arterial peak is 26° .

3.3.2. Comparison Results:

The 3D CE pulse sequence was run using the 3T whole body scanner (Magnex, Abingdon, UK) equipped with 10mT/m gradient strengths with 400 μ s rise times to maximum. The phantom consisted of 1.5 and 2.8 cm diameter cylindrical tubes, which is representative of the phase encoding plane in a typical coronal 3D MRA used for carotid arteries. These tubes were filled with gadolinium (Gd-DTPA) and water with a T1 of 30 ms. The same phantom was used for the artery and the vein. The phase encoding matrix was kept fixed at 32 (z) by 128 (y) where z is the slice selection direction.

The same experimental contrast curve was used throughout this study, however, the start times and the time between arterial and venous enhancement were varied to test

the effects of using various phase encoding techniques. The length of the acquisition is 2.7 minutes.

For each phase encoding order, seven different start times were acquired along the contrast curve. The vessel ROI measurements were made on the experimental artery and vein images, for each given start time and venous return time, in order to determine the experimental artery-to-vein (AV) signal. To normalize the results, a data set was collected with a constant flip angle to produce constant signal intensity equal to the arterial peak. The theoretical data, from a previously developed computer simulation [11], were normalized in the same approach to have a fair comparison with the experimental results.

The theoretical and experimental results are shown in Fig. 3-12 for different starting acquisition times. The horizontal axis represents the start timing as a percentage of the time from the arterial peak divided by the total acquisition time; so the start time is at the arterial peak, and the start time of -50% means that the arterial peak is exactly half way through the acquisition. The AV value of one indicates perfect arterial signal reception and complete venous suppression. In Fig. 3-12a, the arterial ROI signal is plotted, while in Fig. 3-12b the AV contrast is plotted. Note the close agreement among theoretical and experimental results. The vertical dashed lines indicates the start time points for images shown in Fig. 3-13 and Fig. 3-14. From Fig. 3-12b the optimal starting point on the contrast curve for each encoding technique can be determined to have the best AV contrast.

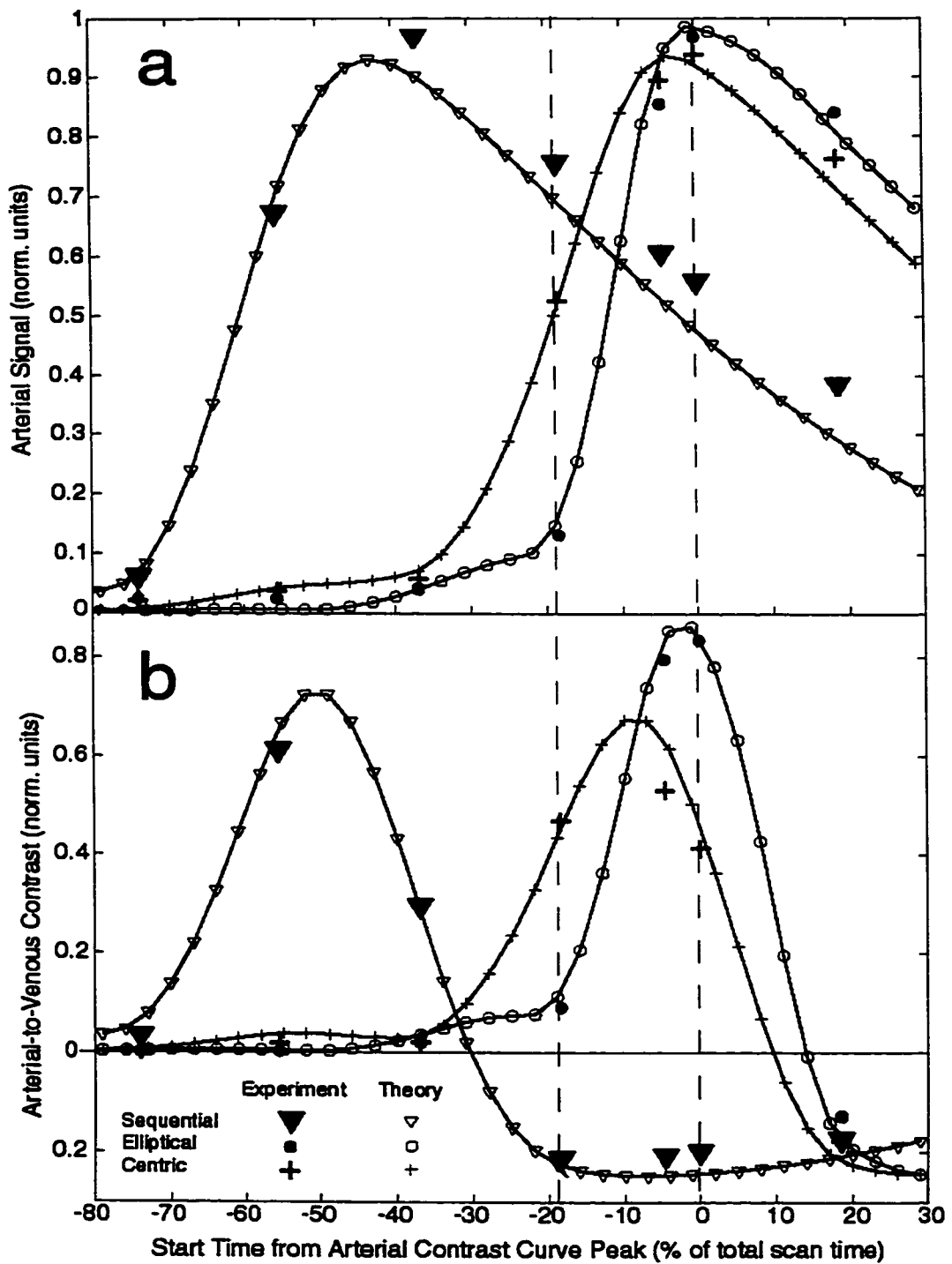


Figure 3-12 The theoretical and experimental effects of varying the start time of data acquisition, (a) the arterial signal (b) the arterial-to-venous contrast. The vertical dashed lines indicates the images shown in Fig. 3-13 and Fig. 3-14.

Fig. 3-13 shows that the best start time for the elliptical encoding technique is located at the arterial peak, start time 0%. Note the high venous suppression with the elliptical technique (c, f) versus the standard centric technique (b, e).

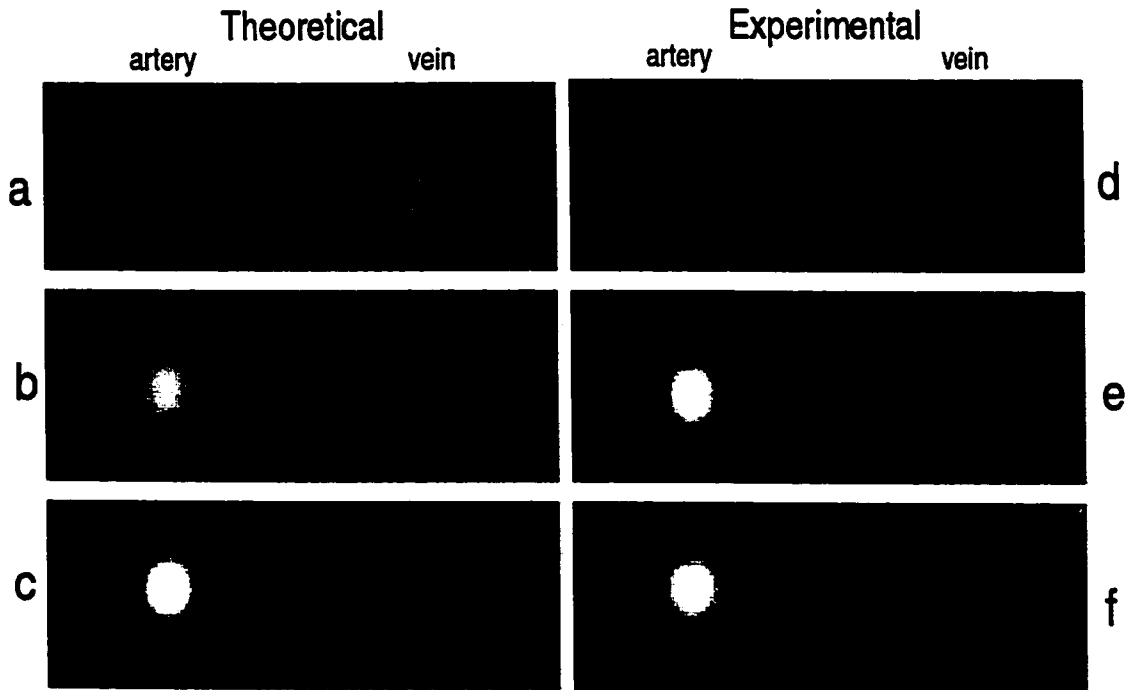


Figure 3-13 Theoretical and experimental images of the simulated artery and vein (tube) corresponding to a start time at the arterial peak (start time of 0% in Fig. 3-12). Images (a-c) are from the computer simulation while (d-f) are experimental images. (a-d) sequential, (b-e) centric, (c-f) elliptical. Note the superior arterial signal from the elliptical technique and the high vein suppression.

Fig 3-14 shows a poor start time -18.5% before the arterial peak. Note the extremely small arterial signal for the elliptical technique (c, f) due to missing the high signal from the center of k -space, where the elliptical is quite compact in the center. In both figures 3-13 and 3-14 the theoretical and experimental images look quite similar.

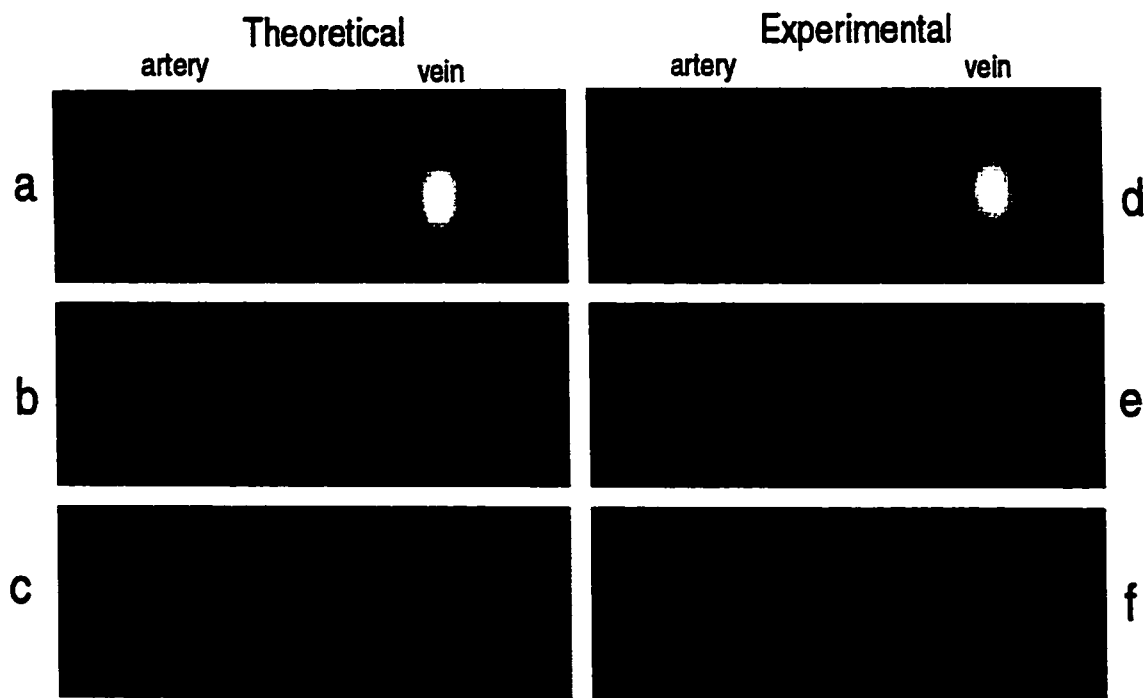


Figure 3-14 Theoretical and experimental images of the simulated artery and vein (tube) corresponding to a poor start time of -18.5% before the arterial peak (Fig. 3-12). Images (a-c) are from the computer simulation while (d-f) are experimental images. (a-d) sequential, (b-e) centric, (c-f) elliptical. Note the poor arterial signal from the elliptical technique, but better result from the sequential one.

It is clear from Fig. 3- 13 and Fig. 3-14 that choosing the acquisition start time is critical to image quality. If the data are acquired before the arrival of the contrast agent (for elliptical and centric), the vessels will not appear in the image. If the data are acquired too late, the arterial signal will be diminished, and the venous signal will be enhanced, which leads into difficulty in evaluating the arteries.

Fig. 3-15 shows the effect of varying arterial-to-venous return time on the AV contrast. The venous return time was varied for each acquisition with the start time always at the arterial peak.

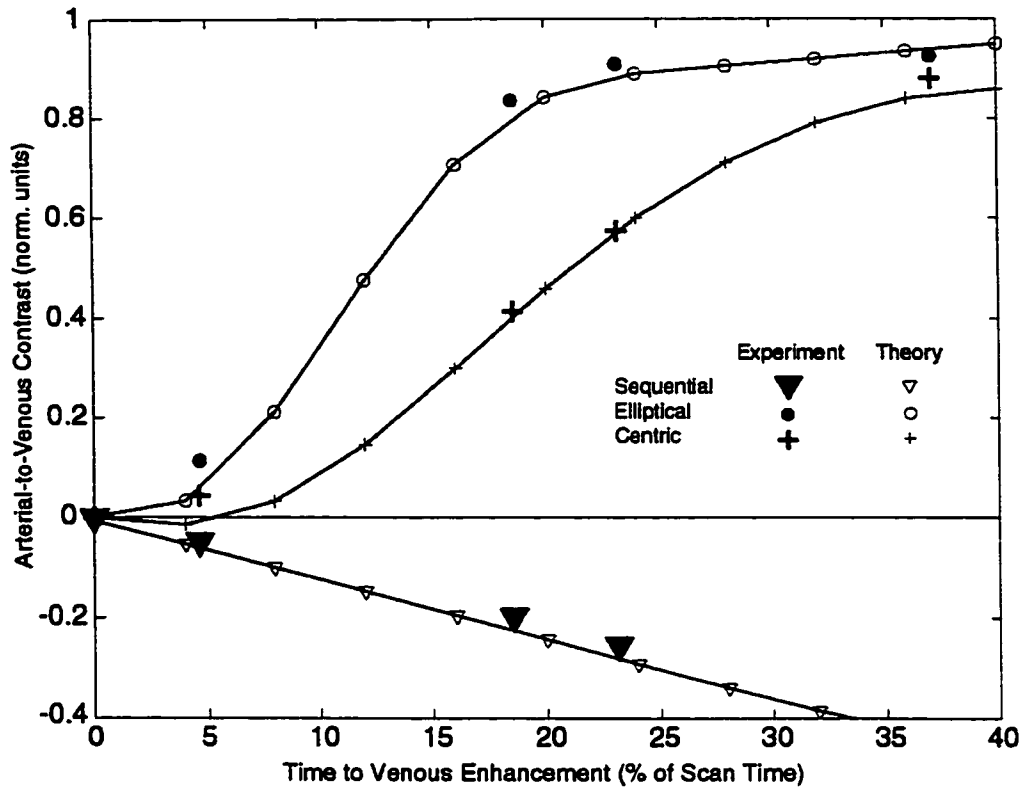


Figure 3-15 Illustration of the effects of varying venous return time on the AV contrast. Note that centric and elliptical techniques approach similar value as a large portion of the scan is completed before venous enhancement.

3.4. Conclusion:

In conclusion, each encoding technique has its own unique characteristics, and all of them are capable of producing a reasonable result if the acquisition is timed correctly. However, if precise timing is available, the image quality can be tremendously improved by optimizing the choice of phase encode scheme, which exhibit the highest degree of compactness for the center of k -space. In this study the elliptical technique provides the superior AV contrast of 0.88, compared to the centric encoding of 0.73, and the sequential encoding of 0.66 for ideal start time for each technique.

3.5. References:

1. Prince, M.R., *et al.*, *Dynamic gadolinium-enhanced 3D abdominal MR arteriography*. J. Magn. Reson. Img., 1993. **3**: p. 877-881.
2. Gonzalez, R.C., *Digital image processing*. 1993: Addison-Wesley Publishing Company.
3. Twieg, D.B., *The k-trajectory formulation of the NMR imaging process with applications in analysis and synthesis of imaging methods*. Med Phys, 1983. **10**: p. 610-621.
4. Ljunggren, S., *A simple graphical representation of Fourier-based imaging methods*. J Magn Reson, 1983. **54**: p. 338-343.
5. Maki, J.H., *et al.*, *The effects of time varying intravascular signal intensity and k-space acquisition order on three-dimensional MR angiography image quality*. J. Magn. Reson. Img., 1996. **6**: p. 642-651.
6. Ito, K., *et al.*, *K-space filter effect in three-dimensional contrast MR angiography*. Acta Radiol, 1997. **38**: p. 173-175.
7. Wilman, A.H. and S.J. Riederer, *Peformance of an elliptical centric view order for signal enhancement and motion artifact suppression in breath-hold three-dimensional gradient echo imaging*. Magn Reson Med, 1997. **38**: p. 793-802.
8. Kim, J., R. Farb, and G. Wright, *Test bolus examination in the carotid artery at dynamic gadolinium-enhanced MR angiography*. Radiology, 1998. **206**: p. 283-289.

9. Potchen, E., *et al.*, *Magnetic Resonance Angiography: Concepts and Applications*. 1993, St. Louis: Mosby.
10. Al-kwif, O. and A.H. Wilman. *Experimental contrast curve design for the evaluation of vessel contrast and artifacts in 3D contrast enhanced MR angiography*. in *ISMRM*. 2000. Denver, USA.
11. Yep, C.H. and A.H. Wilman. *Quantitative evaluation of centric view orders for 3D contrast enhanced MR angiography*. in *ISMRM*. 1999. Philadelphia, USA.
12. Mugler, J.P., F.H. Epstein, and J.R. Brookeman, *Shaping the signal response during the approach to steady state in three-dimensional magnetization-prepared rapid gradient-echo imaging using variable flip angles*. *Magn Reson Med*, 1992. **28**: p. 165-185.

CHAPTER 4

3D Contrast Enhanced MRA

4.1. Introduction:

3D CE MRA is able to obtain high resolution images of the carotid arteries from their origins up to the Circle of Willis in 30-40 seconds, where in the mid 1990's it would have taken up to 15 minutes to obtain this amount of coverage without contrast agent, because the recovery rate of the MR signal is much more rapid when the contrast agent is present. However, the contrast agent signal is transient and also increases the signal intensity of veins which can obscure the arterial signal in the final images.

The main challenge with 3D CE MRA is to scan long enough to collect sufficient spatial resolution while limiting the signal from veins. This is very difficult in the carotid arteries where the intense jugular vein signal will appear within approximately 7 seconds following carotid artery enhancement, but the scan time must be at least 30~40 seconds to obtain the necessary coverage. For this reason the centric encoding [1] is used in 3D CE MRA to implement this study.

The use of contrast agents allows one to reduce several limitations of current MRA techniques. By using a contrast agent in conjunction with time of flight techniques,

the MR signal no longer exclusively depends on flow characteristics. The steady state magnetization increases because of the T1 shortening of the blood, leading to a higher vascular signal. The short blood T1 allows use of short TR times and larger flip angle without worrying about saturating the blood signal. Also, this allows one to acquire all the data in one 3D acquisition encompassing the complete vessel of interest. In contrast, 3D TOF must be mainly acquired using multiple slabs perpendicular to the direction of flow.

The use of extrinsic contrast agents (paramagnetic species) for MRA was initially performed in 1993 by Prince [2] [3] to improve the sensitivity and the specificity of MRA. MR contrast agents such as gadolinium (Gd-DTPA) (Gd) have been used previously in clinical MRI to increase lesion conspicuity and obtain functional information about pathology processes. The agents are injected intravenously and rapidly distribute through the vascular system, and are excreted via glomerular filtration, approximately 95% of the injection dose being excreted within 24 hours [1].

In this chapter the importance of the contrast agents for MRA will be described. Although patient studies were not performed, the 3D CE MRA pulse sequence with centric phase encoding was fully developed and tested on the flow phantom.

4.2. Effect of Reducing T1 via Contrast Agent:

In an RF spoiled gradient echo sequence, the steady state signal and the number of excitations mainly depend on the T1 of the tissue as well as the TR and flip angle [4]. Fig. 4-1 shows the progress of the longitudinal magnetization toward the steady state for gradient echo sequence for different T1 values as a function of number of excitations. Note that a longer T1 requires a larger number of excitations, up to 40, to reach the steady state and the magnetization is low, and as a result the SNR is low. This saturation happens in 3D TOF sequences when the blood flow is low. Therefore, in the TOF MRA method the imaging volume is oriented perpendicular to the main direction of flow to reduce the saturation effect of flowing blood.

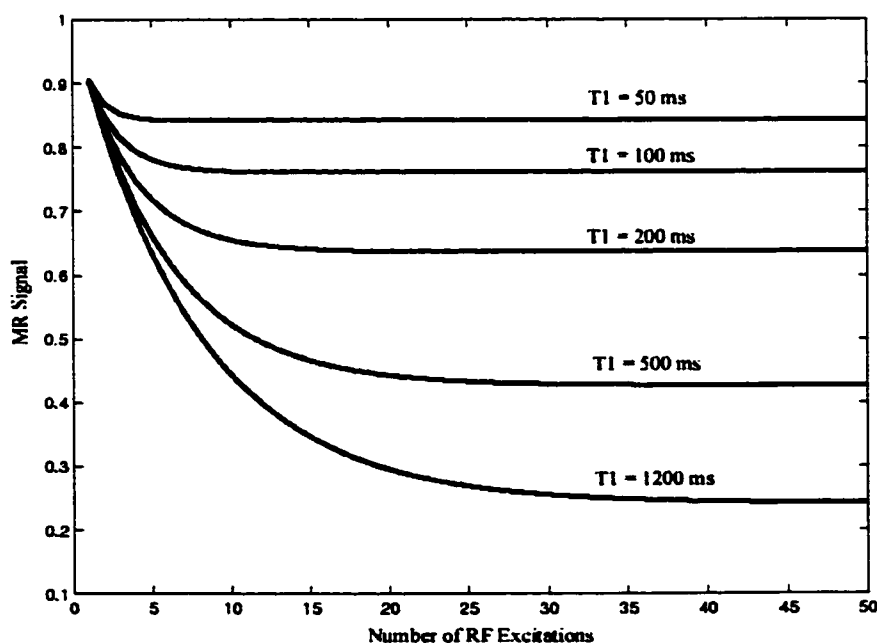


Figure 4-1 Theoretical relative signal amplitude of tissues with different T1 values as a function of number of RF excitations for gradient echo sequence (TR/flip angle = 40/25°). Decreasing T1 increases the MR signal and decreases the number of excitations to reach the steady state.

The use of an extrinsic contrast agent to decrease the T1 of blood has shown that the saturation effect can be dramatically reduced in 3D TOF MRA [5], and the steady state is reached rapidly for shorter T1. The blood contrast is proportional to the T1 value, contrast concentration, and is not affected by flow velocity. Therefore, both fast flowing and slow flowing blood can be visualized, regardless of the applied image orientation.

The steady state signal as a function of flip angle for different T1 values is shown in Fig. 4-2. As the T1 decreases the MR signal at the steady state increases. Note that the optimal flip angle, the Ernst angle, is shifted to a higher value. The increase in the optimal flip angle will saturate the static tissue and improve vessel contrast [6].

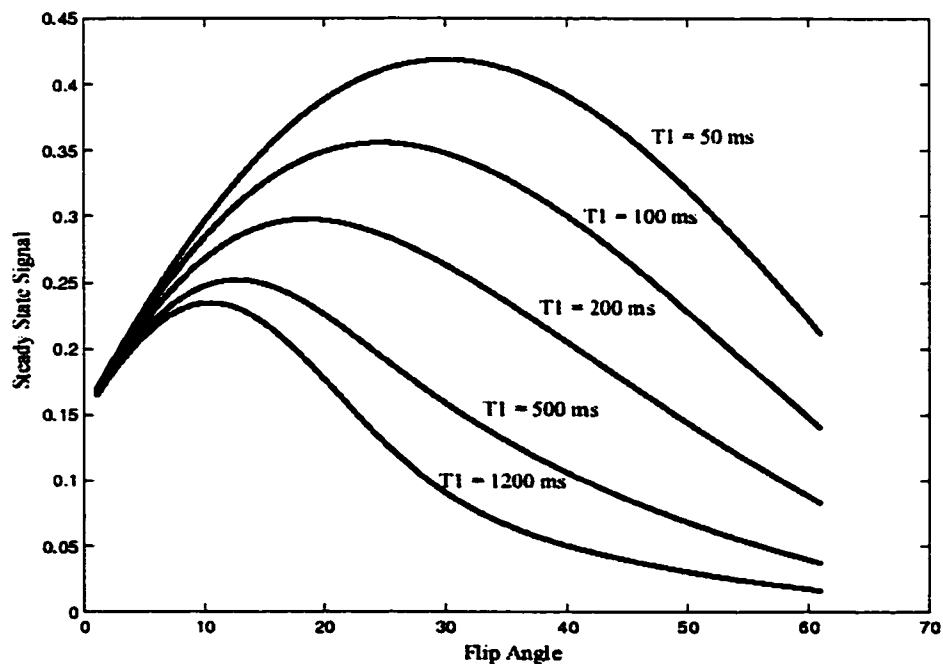


Figure 4-2 Theoretical MR signal at steady state as a function of the flip angle for gradient echo sequence with different T1 values, different contrast agent doses (TR = 40). Note the significant signal increase for the short T1.

The effect of the repetition time on the steady state signal is shown in Fig. 4-3 for several T1 values for a gradient echo sequence with flip angle 30° . As expected, decreasing the T1 value increases the steady state significantly, for a given TR value. In CE MRA sequences the very short TR (5 ~ 8 ms) reduces the acquisition time significantly (25 ~ 60 sec) while still maintaining high blood signal, and increasing suppression of the static tissue at shorter TR.

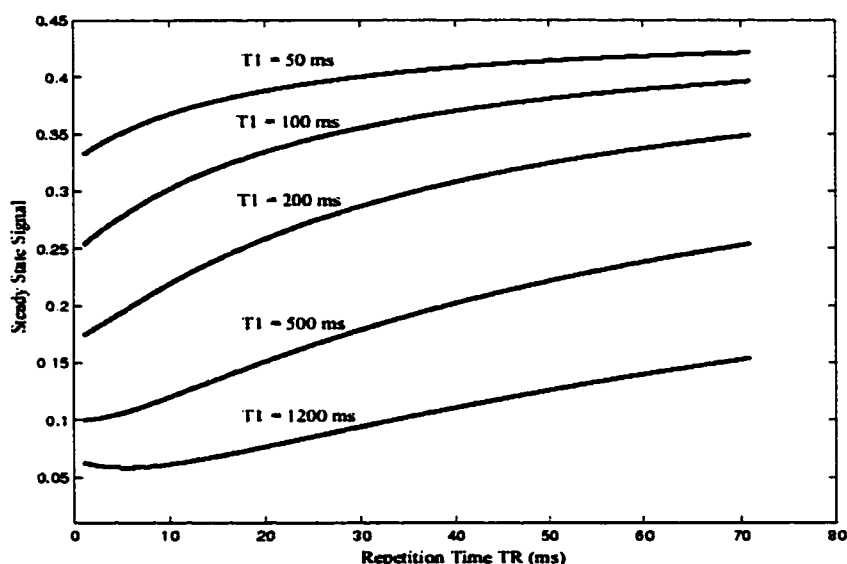


Figure 4-3 Theoretical MR signal at steady state as a function of repetition time with different T1 values. Note that as T1 decreases the signal intensity increases dramatically for a given TR.

4.3. Measurement of T1 Reduction by Contrast Agent at 1.5 and 3 T:

4.3.1. Pulse Sequence Design:

The purpose of this experiment was to demonstrate the difference in T1 values for different concentrations of the contrast agent (Gd-DTPA) under different field strengths,

namely 1.5 and 3T. The 2D gradient echo inversion recovery (IR) pulse sequence, Fig. 4-4, is used to measure T1 by changing the inversion time (TI).

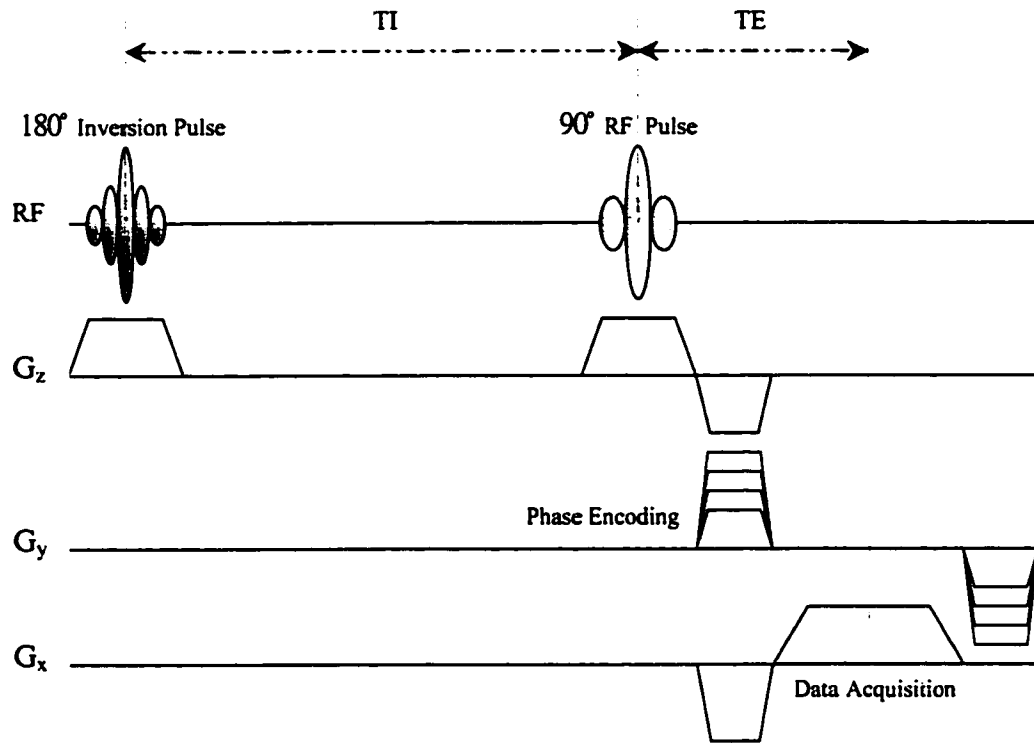


Figure 4-4 The 2D GE inversion recovery pulse sequence used to measure T1 values. The inversion time is defined as the time between the 180° and 90° pulses, and varied during the experiment.

The longitudinal magnetization regrows to its equilibrium value, assuming TR infinite, in the interval between the pulses according to:

$$M_z(t) = M_0(1 - 2e^{-t/T1}) , \quad 0 < t < TI \quad (4-1)$$

When the longitudinal magnetization is flipped into the transverse plane to provide the initial signal, the magnitude of the transverse magnetization calculated as:

$$M_{xy}(t) = |M_o(1 - 2e^{-t/T1})| e^{-(t-TI)/T2^*}, \quad t > TI \quad (4-2)$$

Since an identical echo time is used for all images, the $T2^*$ contribution is constant and ignored in the calculation [7]. The accurate way to determine the T1 is to change the TI so that the signal vanishes when:

$$TI_{null} = T1 * \ln 2 \quad (4-3)$$

This shows that the signal is a sensitive function of T1, as shown in Fig. 4-5. The TI is varied until a signal zero is located. Since the signal zero can be accurately determined, so that T1, especially for a uniform sample.

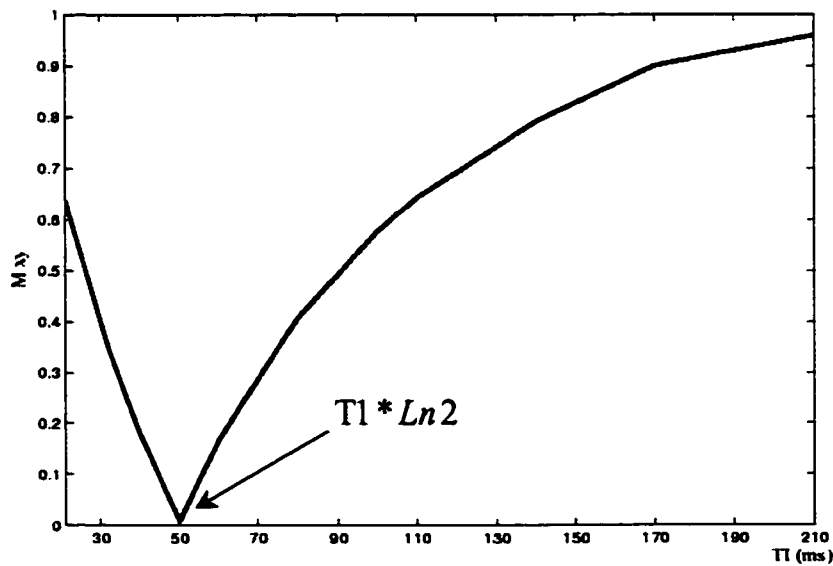


Figure 4-5 The magnitude of the signal as a function of TI for a 2D GE inversion recovery sequence. Note that the signal vanishes at $(T1 * \ln 2)$ which matches the point where the longitudinal magnetization has recovered from M_o to zero.

4.3.2. Experiments and Results:

The experiments were performed on a 1.5 Siemens Magnetom and a 3T SMIS whole body magnet. The same sample, which consists of 10 circular tubes 1.5cm in diameter filled with different concentrations of gadolinium (Magnevist) was used, as shown in Fig. 4-6.

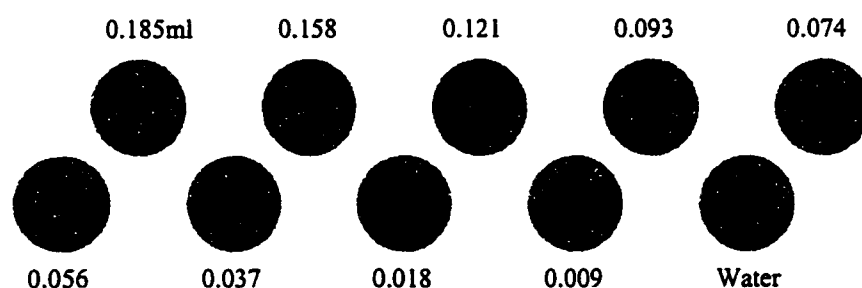


Figure 4-6 The sample used to measure T1 values with different gadolinium concentrations (ml Gd per 16ml water). Note that the water is considered to be reference in this experiment.

The same parameters were used at both field strengths TR/TE= 4000/5.7 ms, flip angle 90°, 512×192 resolution, FOV 200mm. TI was varied according to the following values (11, 22, 30, 40, 50, 70, 90, 100, 130, 160, 200, 300, 400, 500, 700, 1000 ms), and slice thickness 5mm. After data were collected for both field strengths, the Siemens images were transferred into SMIS format for choosing the ROIs using the same software, to have a fair comparison. In the SMIS image display the same ROIs in the 10 tubes for 16 different inversion time were determined accurately to measure the signal intensity. The data were processed using MATLAB™ program to fit the curves in Eq. (4-2) and calculate T1 values. The final results were tabulated in Table 4-1 for the both field strengths, and Fig. 4-6 shows a graphical plot for these values.

Gd-DTPA Concentration		T1 measurement (ms)	T1 measurement (ms)
(ml per 16ml water)	$10^{-3} \times \text{mmol/ml}$	(at 1.5 T)	(at 3 T)
0.0 (Water)	0.00	1549	2024
0.009	0.28	385	461
0.018	0.56	208	247
0.037	1.15	98	114
0.056	1.75	72	81
0.074	2.31	54	67
0.093	2.90	47	57
0.121	3.75	34	39
0.158	4.88	29	35
0.185	5.71	25	29

Table 4-1 The experimental T1 values for different Gadolinium concentrations at both field strengths. Note that T1 value increases as the field strength increases.

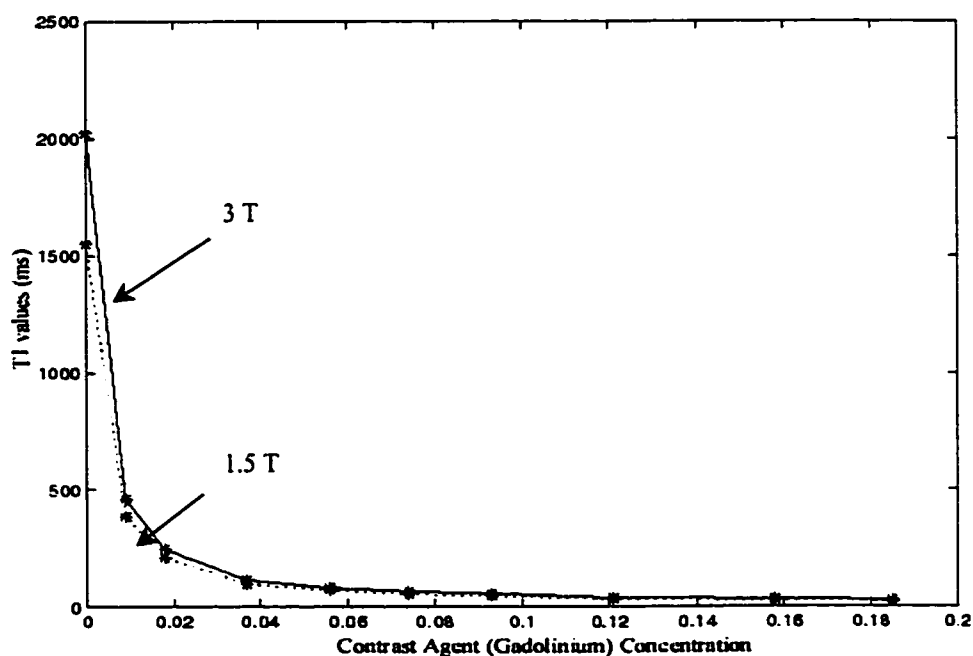


Figure 4-7 Graphical plot for the experimental T1 values from table 4-1.

Fig. 4-8 shows the source images of the samples used at different TI intervals; note how the signal zeros for different tubes when TI is changed in the experiment. This technique for measuring T1 is reliable and accurate since the signal zeros can be accurately determined.

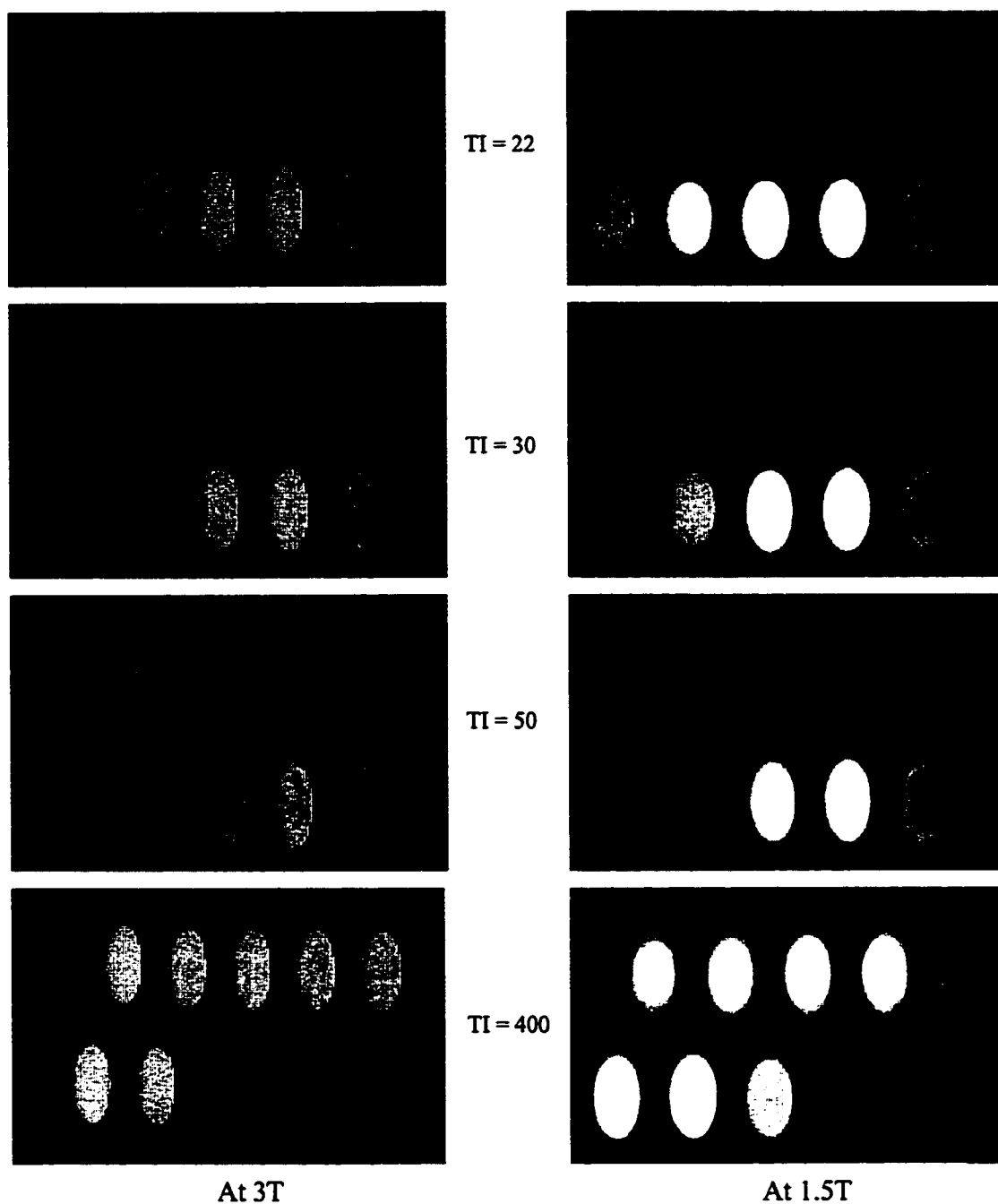


Figure 4-8 The source images of the used sample acquired by 2D GE inversion recovery pulse sequence at different TI intervals on 3T. It is clear how the signal zeros at certain TI values.

Table 4-2 shows different values of the relaxation time T1 at 1.5 and 3T (some of the T1 values are estimated at 3T). The increase in T1 values gives the 3T the advantage of suppressing the background signal more easily from fat and muscle. Fig. 4-9 shows a theoretical plot for the blood signal and background, assuming a first pass concentration of $2.90 \times 10^{-3} \times \text{mmol/ml}$ and a flip angle of 40° , at different field strengths.

Tissue	T1 (ms) at 1.5 T	T1 (ms) at 3 T
Blood	1200	1500
Fat	260	380
Muscle	870	1280

Table 4-2 Representative values of the relaxation time T1 at 1.5 and 3T. Note increasing T1 values as the field strength increases.

To find out the contrast difference between 1.5 and 3T for both the fat and muscle the following equation was used:

$$\text{Contrast Difference} = \left[\frac{\text{Blood} - \text{Background}}{\text{Background}} \right]^{3T} - \left[\frac{\text{Blood} - \text{Background}}{\text{Background}} \right]^{1.5T} \quad (4-4)$$

From Fig. 4-10 it is clear how the 3T field can produce better blood-to-background contrast than 1.5T by using the contrast agent.

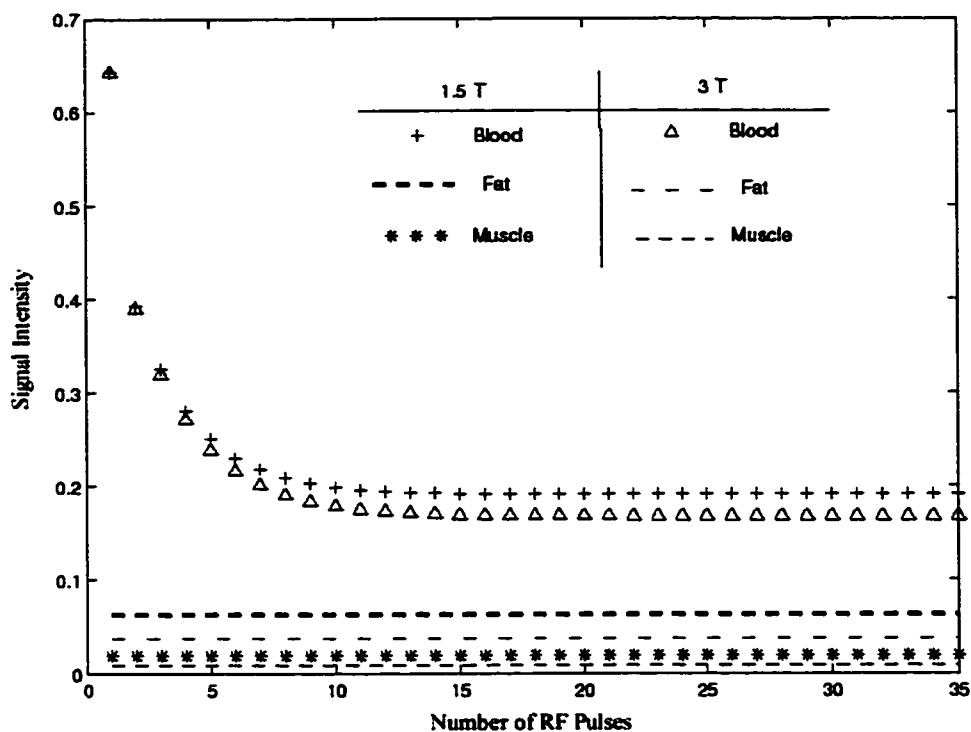


Figure 4-9 A theoretical plot for blood and background signals at different field strengths, assuming the first pass of the contrast agent T1 47ms at 1.5T and 57ms at 3T. Note the high blood signal which produced from the first pass. FA 40° and TR 6.5ms.

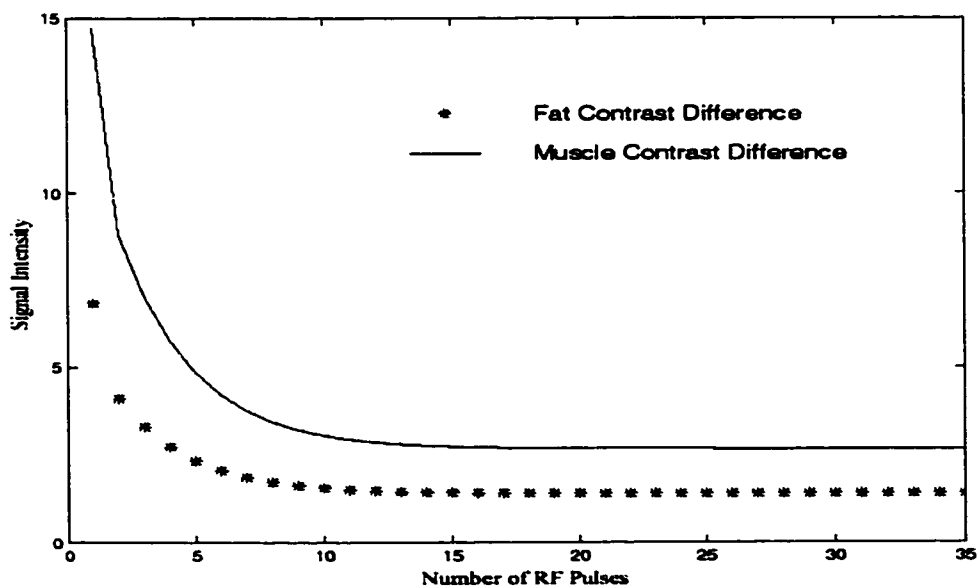


Figure 4-10 The contrast difference between the 1.5 and 3T for both the fat and muscle. Above the zero line is the advantage of 3T in having better contrast. FA 25° and TR 6.5ms.

4.4. 3D Contrast Enhanced MRA Pulse Sequence:

To implement the 3D CE sequence substantial technical obstacles must first overcome. These challenges include minimizing the acquisition time to catch the first pass of the contrast agent with less vein enhancement. In general the acquisition time depends on the number of phase encoding steps, in both directions, and the repetition time of the sequence as:

$$T_{acq} = TR * N_z * N_y \quad (4-5)$$

From Eq. (4-5) it is clear that reducing the acquisition time can be achieved by reducing the spatial resolution, but this is not acceptable. However, the repetition time could be reduced yielding a proportionate reduction in acquisition time. The penalty with this is that the overall SNR of the image becomes degraded due to a more limited degree of T1 recovery which is acceptable since the contrast agent will ensure high SNR in the blood vessels [2].

Another approach used to reduce TR involves increasing the rate at which data are collected [8]. With an increased rate, the same amount of data can be acquired in a reduced time. This increase in sampling rate is achieved by increasing the bandwidth of the MR signal. However, since the bandwidth is proportional to the gradient strength, this approach requires an increase in gradient strength and a loss of SNR. Nevertheless it does come with a decreased TE time.

Fig. 4-11 shows the 3D CE pulse sequence design used. This sequence is derived from a 3D TOF sequence, where $TE = 2.2\text{ms}$ by using truncated RF pulse [9], 50% fractional echo [10], and removing the flow compensation gradients.

The value of TR is 6.5ms achieved by increasing the receiver bandwidth (200 KHz), removing the saturation pulse, and minimizing dead time by implementing most of the calculations during gradients play out time.

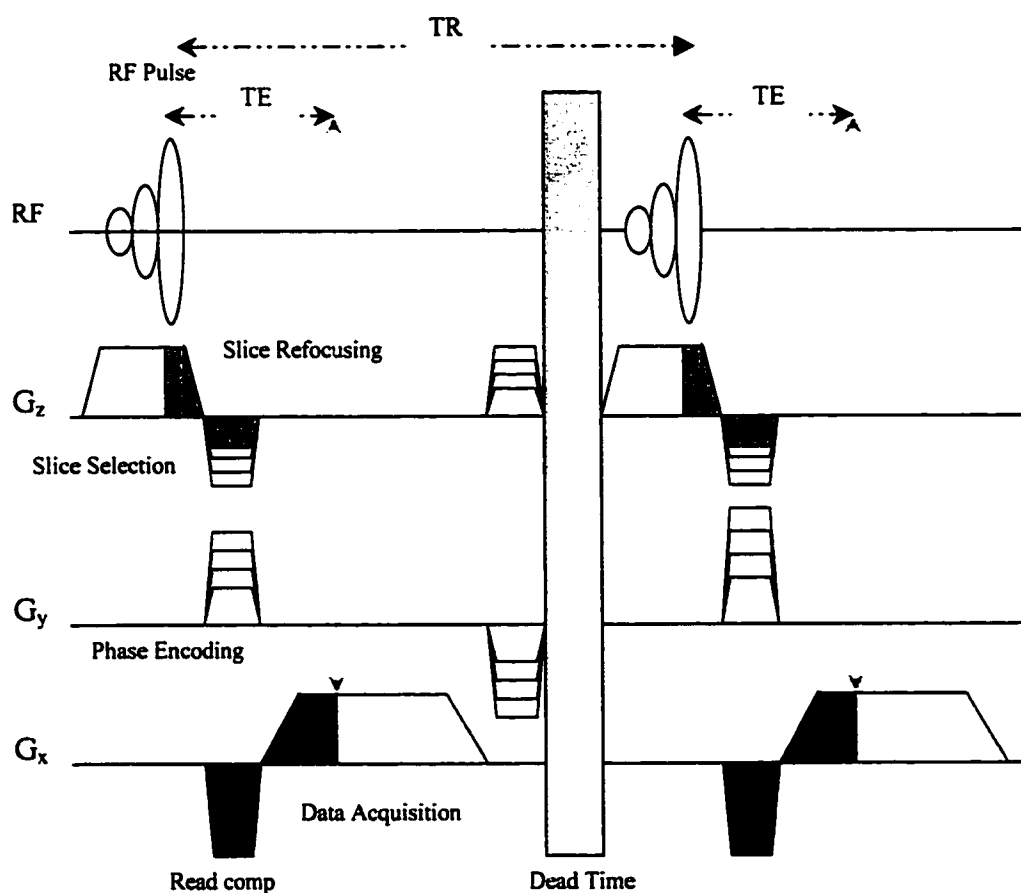


Figure 4-11 3D CE MRA with short TE 2.2ms and TR 6.5ms to encode the arterial signal with the first pass of the contrast agent. The dead time is used for implementing some calculations to update the gradient values. Note that the majority of the calculations are hidden inside the phase encoding gradient in order to reduce the TR.

Since the centric encoding technique is used in this sequence, a number of dummy scans are used before data acquisition to enable the MR signal to reach the steady state [11] and remove the ringing effects in the images.

4.4.1. Timing the Contrast Agent Arrival (Test Bolus):

Synchronizing the acquisition with the arrival of the contrast agent is critical to image quality [12]. From chapter 3 it was clear how important is the start of data acquisition and the type of phase encoding in the 3D CE MRA, as shown in Fig. 4-12.

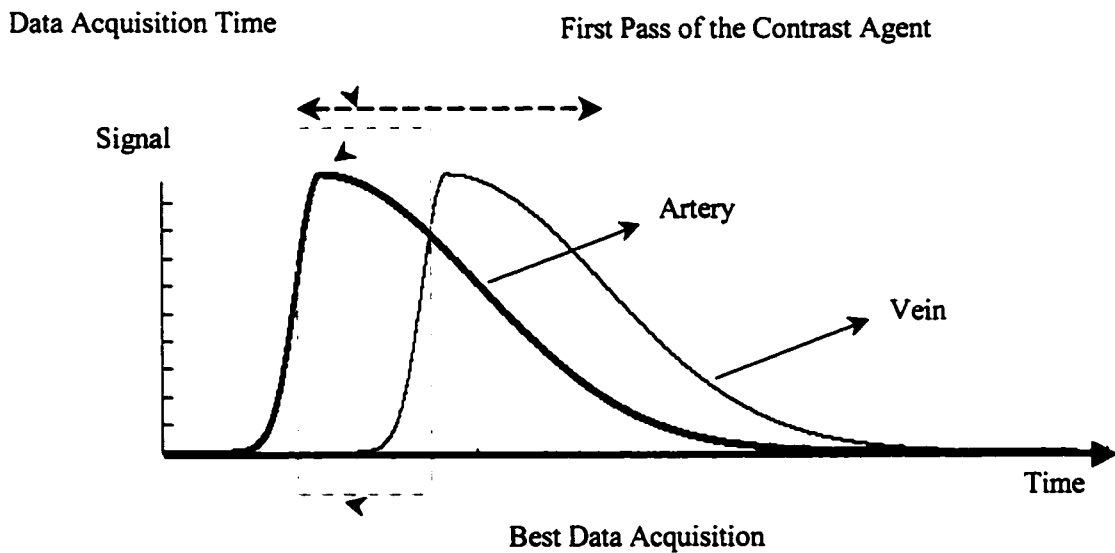


Figure 4-12 Producing high signal from the first pass of the contrast agent. Note the vein enhancement after the blood returns back to the region of interest. The dashed box indicates the best area to be encoded in the center of k -space, where the vein enhancement is not exist.

In vivo, several methods have been developed to ensure proper timing of data acquisition relative to the arrival of the contrast agent to the targeted vessels. Because of

large patient to patient difference in bolus transit times it is not practical to reliably predict when to start the data acquisition for a certain patient [13].

It was noted that the acquisition of the central phase encoding views of the MR data must match to the desired arterial signal [14]. Therefore, starting the acquisition before the arrival of the contrast agent results in low signal and severe edge enhancement, while starting after the arrival again results in low signal with some blurring and venous enhancement (as shown in Chapter 3).

One of these methods to estimate the correct timing for contrast arrival into the ROI is test bolus [15] consists of two steps. First, a small dose, 1ml as illustrated in Fig. 4-13, of the contrast agent is injected intravenously. By monitoring the contrast agent arrival either with a real time line scan [16] or by real time 2D imaging [17] the correct timing can be measured. The second step is to inject the rest of the dose and wait the measured time to start the 3D CE imaging sequence.

This method is successful to some degree and the most widely used, since it does not require any additional software or hardware, such as a power injector [18]. Other methods can detect the contrast curve arrival by simply turning the phase encoding off for a 3D CE sequence in both directions and monitoring on real time the signal increment, which is contrast arrival to the ROI.

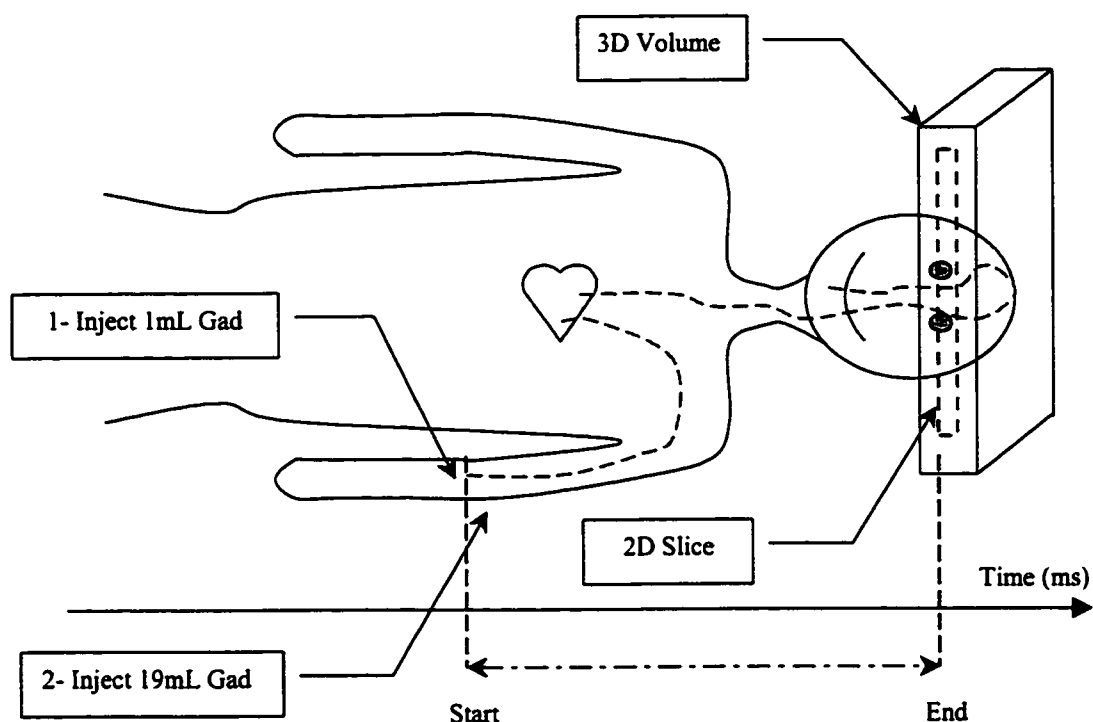


Figure 4-13 Test bolus trail, where a small dose is injected first to measure the correct timing of the contrast agent arrival to the ROI before running the 3D CE sequence.

4.4.2. 3D CE Experimental Protocol:

The general parameters used in the 3D CE sequence include: $256 \times 128 \times 32$ spatial resolution with oversampling at 200 KHz, FOV 240mm to cover larger vasculature of interest, 50% fractional echo to reduce TE, $TR/TE = 6.5/2.2\text{ms}$, FA 15° , and rectangular FOV [19]. A research scanner with a 3T field strength (Magnex 20mT/m, UK) was used in this experiment.

The flow phantom as shown in Fig. 4-14 is used to simulate the blood vessels in the body. The container is filled with Agar to match the tissue around the vessels and it represents the ROI in our study. Two tubes are crossing this ROI, the one coming from

the pump represents the artery, while the other returning back to the water tank is the vein. Note that two water containers are used to ensure that the water and Gd mixture will never return back into the ROI.

Gadolinium is injected as a contrast agent through the artery using a needle. The 3D CE protocol is started by taking scout images (sagittal images in Fig. 4-16 for the patient study) using a 2D sequence for accurate determination of the ROI, which includes in this case the container and the two tubes. Shimming is performed to maximize the signal intensity over the entire ROI, then the RF pulse is optimized to the correct value. The receiver gain is adjusted to a low value, since the arrival of the contrast agent will increase the MR signal significantly.

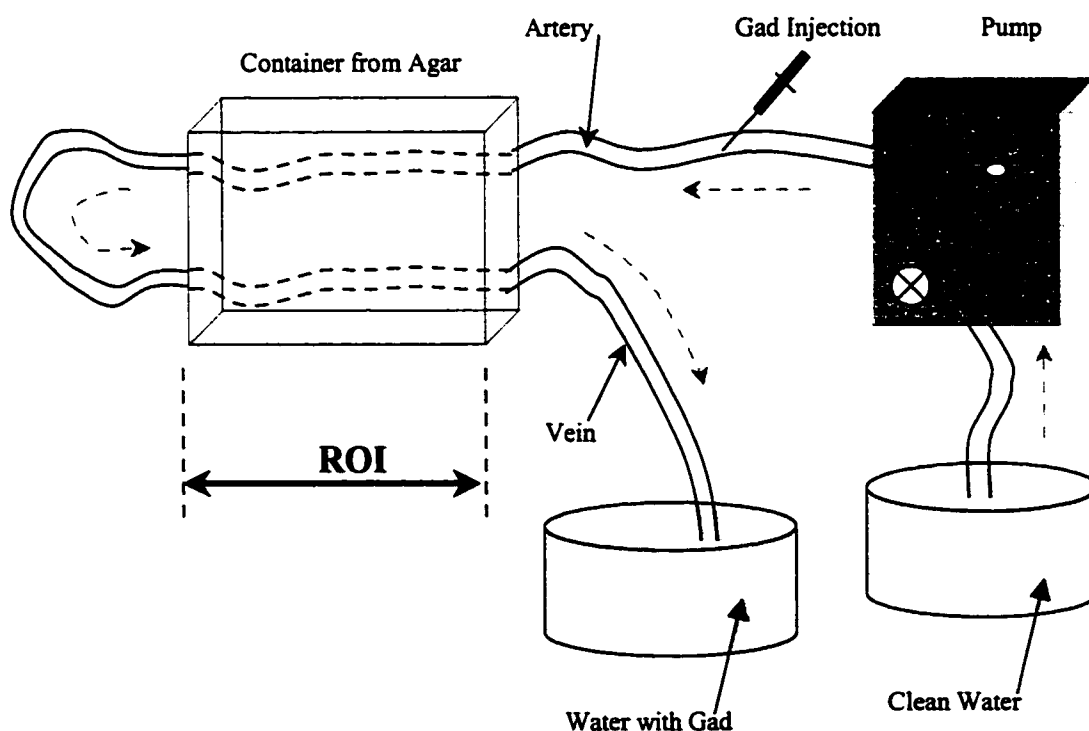


Figure 4-14 Simulating the blood vessels through the flow phantom; the pump speed can be adjusted to reasonable values to match in-vivo blood speeds. The water and Gd mixture is thrown into separate container to ensure that the Gd will never return back into the ROI.

Test bolus is done through taking fast 2D GE coronal images for the ROI and watching the image reconstruction at real time to see when the Gd enters the ROI and calculate the correct timing for contrast arrival. In this case, 1ml was injected into the tube that represents the artery. After 4 seconds the Gd started passing through ROI as shown in Fig. 4-15, where the MR signal at the SMIS monitor started increasing as the Gd flew into the targeted artery in the ROI.

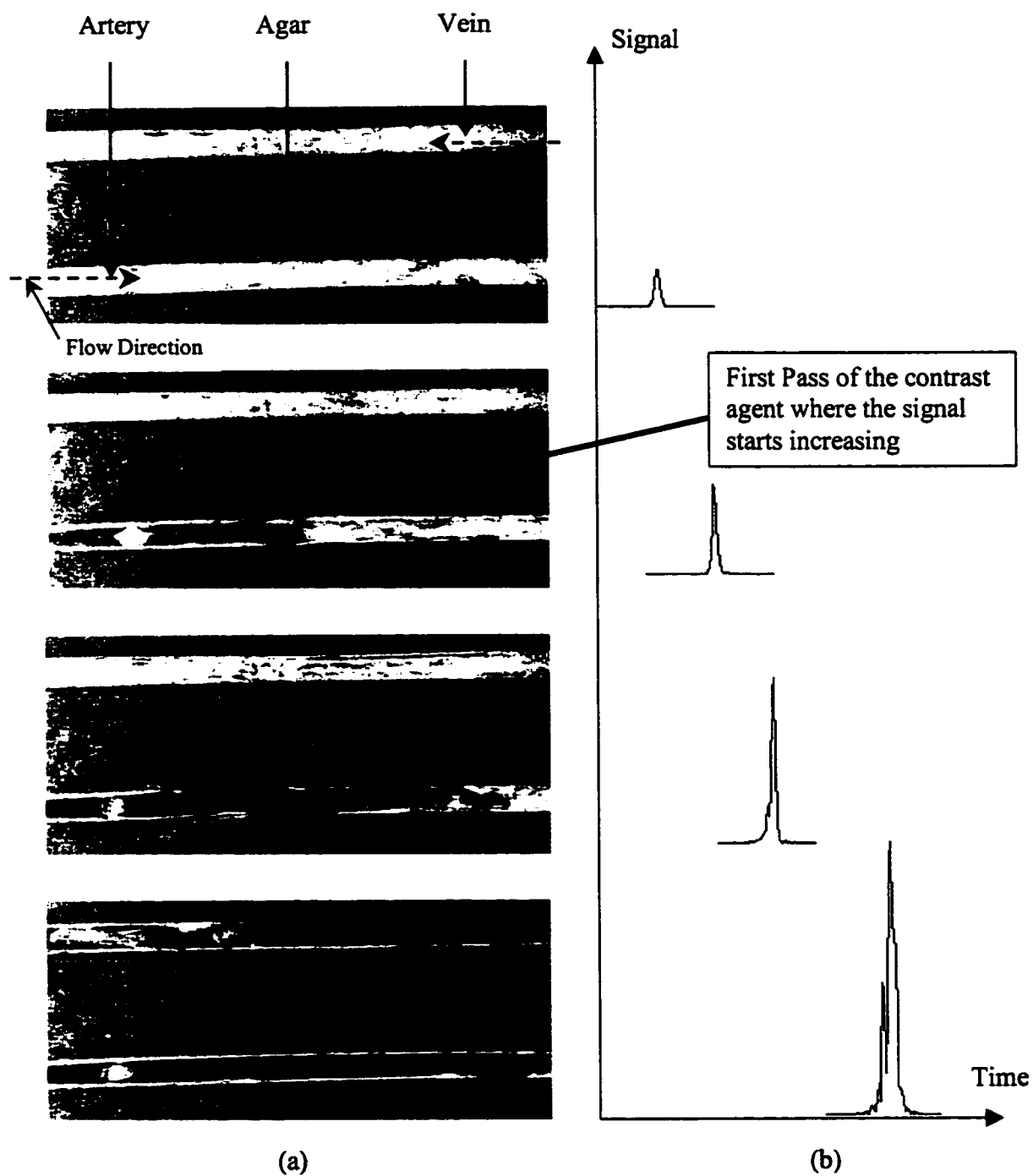


Figure 4-15 Test bolus on the flow phantom to determine the correct timing for the Gd arrival into the ROI, where fast 2D images were taken in the same location to mark the Gd arrival. (a) Coronal images for the ROI (b) The corresponding signal intensity on the Output Signal Display, which can determine the Gd arrival into the ROI.

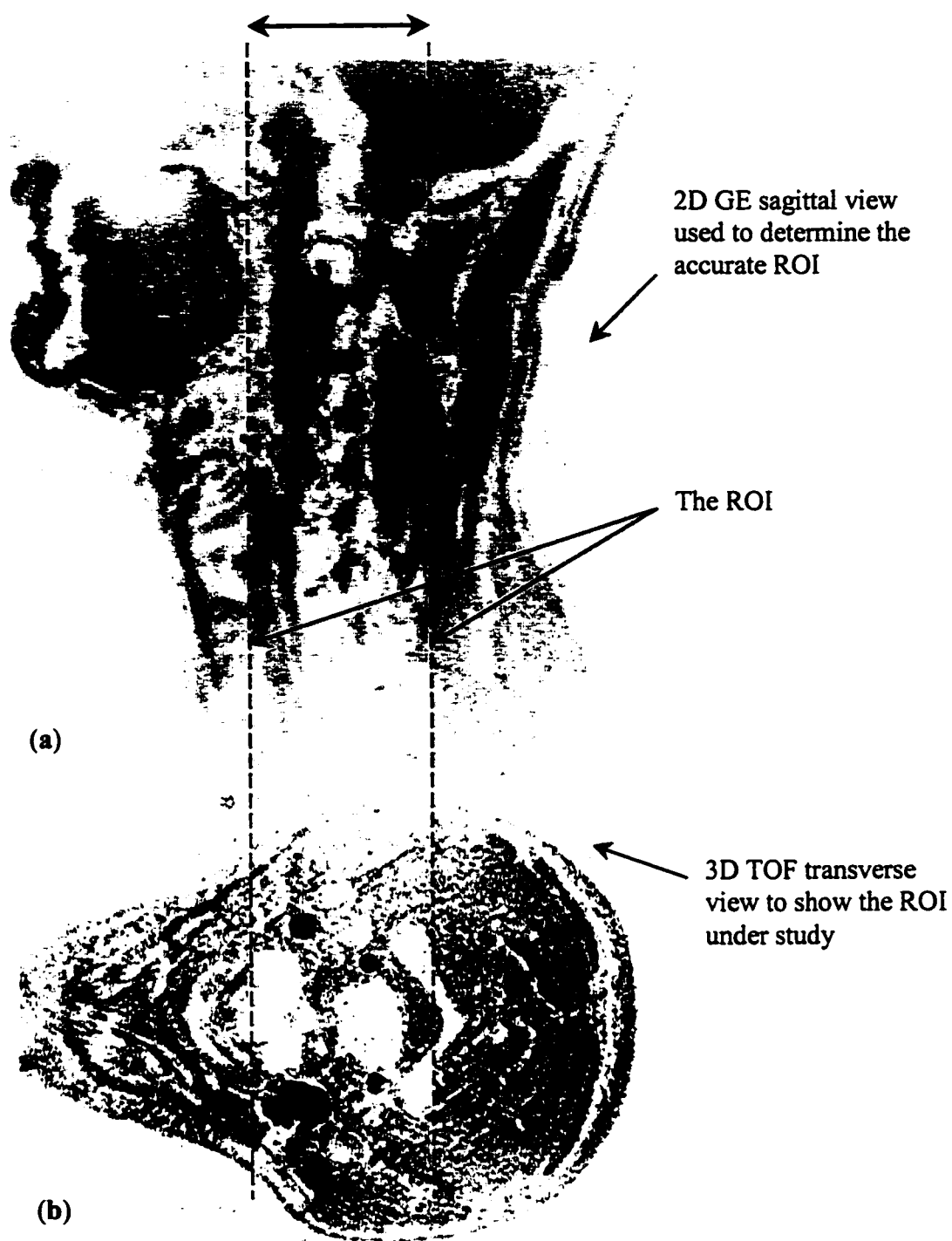


Figure 4-16 (a) Scout image for the neck for accurate determination of the ROI before injecting the contrast agent and running the 3D CE MRA sequence. (b) 3D TOF to show the arteries under study. Note the wide coverage for the blood vessels that 3D CE can have.

4.5. Conclusion:

The decrease in T1 achieved by contrast agents decreases the signal loss caused by spin saturation, and that helps in imaging a large FOV to visualize larger vascular areas in a short acquisition time. Because of a short echo time, the large blood signal is minimally affected by dephasing which is caused by complex flow and susceptibility variations.

Since contrast enhanced MRA is less sensitive to RF saturation, it can provide higher quality images with fewer artifacts than the non-contrast enhanced techniques. Acquisition starting time and choice of the phase encoding technique play a large role in enhancing the arterial signal and suppressing the venous signal.

Measuring T1 values, using GE inversion recovery sequence, at 1.5 and 3T field strengths showed the effect of the higher field in increasing T1 value. The theoretical results show that the contrast agent has a big impact on the blood-to-background contrast in both fields, but the higher the field the better the contrast will be.

The 3D CE sequence with centric phase encoding, which exhibits a high degree of compactness for the center of k -space, was fully developed and tested on the flow phantom. A test bolus technique was also developed to measure the correct timing for the contrast arrival into the ROI to produce superior artery-to-vein contrast.

4.6. References:

1. Potchen, E., *et al.*, *Magnetic Resonance Angiography: Concepts and Applications*. 1993, St. Louis: Mosby.
2. Prince, M.R., *et al.*, *Dynamic gadolinium-enhanced 3D abdominal MR arteriography*. J. Magn. Reson. Img., 1993. 3: p. 877-881.
3. Prince, M.R., *Gadolinium-enhanced MR aortography*. Radiology, 1994. 191: p. 155-164.
4. Parker, D.L., C. Yuan, and D.D. Blatter, *MR angiography by multiple thin slab 3D acquisition*. Magn Reson in Med, 1991. 17: p. 434-451.
5. Marchal, G., *et al.*, *Contrast-enhanced MRA of the brain*. J Comp Assist Tomog, 1992. 16: p. 25-29.
6. Haacke, E.M., *Magnetic Resonance Imaging, physical principles and sequence design*. 1999: John Willey & Sons.
7. Kim, S.G., *Accurate T1 determination from inversion recovery imaging: application to human brain at 4 Tesla*. Magn Reson Med, 1994. 31: p. 445-449.
8. Vinitsky, S., *et al.*, *Effect of sampling rate on magnetic resonance imaging*. Magn Reson in Med, 1987. 5: p. 278-282.
9. Frederickson, J. and N. Pelc, *Time-resolved MR imaging by automatic data segmentation*. J Magn Reson Img, 1994. 4: p. 189-196.
10. MacFall, J.R., N.J. Pelc, and R.M. Vavrek, *Correction of spatially dependent phase shifts for partial Fourier imaging*. Magn Reson Imaging, 1988. 6: p. 143-155.

11. Bronskill, M.J., *The physics of MRI 1992 AAPM summer school proceeding*. 1993, Woodbury: American Institute of Physics, Inc.
12. Prince, M.R., et al., *Contrast-enhanced abdominal MR angiography: optimization of imaging delay time by automating the detection of contrast material arrival in the aorta*. Radiology, 1997. **203**: p. 109-114.
13. Kim, J., R. Farb, and G. Wright, *Test bolus examination in the carotid artery at dynamic gadolinium-enhanced MR angiography*. Radiology, 1998. **206**: p. 283-289.
14. Maki, J.H., et al., *The effects of time varying intravascular signal intensity and k-space acquisition order on three-dimensional MR angiography image quality*. J. Magn. Reson. Img., 1996. **6**: p. 642-651.
15. Earls, J.P., et al., *Breath-hold single-dose gadolinium-enhanced three-dimensional MR aortography: usefulness of a timing examination and MR power injector*. Radiology, 1996. **201**: p. 705 - 710.
16. Foo, T.K.F., et al., *Automated detection of bolus arrival and initiation of data acquisition in fast, three-dimensional, gadolinium-enhanced MR angiography*. Radiology, 1997. **203**: p. 275-280.
17. Wilman, A.H., et al., *Fluoroscopically-triggered contrast-enhanced 3D MR angiography with elliptical centric view order: application to the renal arteries*. Radiology, 1997. **205**: p. 137-146.
18. Earls, J.P., et al., *Hepatic arterial-phase dynamic gadolinium-enhanced MR imaging: optimization with a test examination and a power injector*. Radiology, 1997. **202**: p. 268 - 273.

19. Xiaoping, H. and P. Todd, *Reduction of field of view for dynamic imaging*. Magn Reson Med, 1994. **31**: p. 691-694.

CHAPTER 5

Conclusion

5.1. Conclusion:

The focus of this thesis was to develop 3D MRA pulse sequences at a 3T field strength. During this work detailed consideration was given to the widely used TOF and CE MRA sequences supported with flow phantom and in-vivo experimental results.

In chapter one, a brief overview of the MR fundamentals was explained, on which all this work was built. Understanding these fundamentals creates a solid base for improving and enhancing MR imaging of blood vessels.

In chapter two, a detailed description was given for designing 2D and 3D TOF pulse sequences to enhance their performance. Using flow compensation, special RF pulses, optimal flip angles, optimal echo times, and oversampling have all contributed to the MR signal optimization, and provided less artifacts. 3D TOF MRA is a powerful tool in providing good inflow contrast, good spatial resolution, and high SNR. It provides higher SNR and thinner slices than 2D TOF. 3D TOF provides the best resolution to see small vessels with relatively fast flow, and is preferable for cranial application.

A comparison study was made on seven healthy volunteers to study the effect of using higher field to improve blood contrast. The experimental results (Table 2-6), as

well as the theoretical calculations, showed a big improvement in producing higher blood to background contrast, 5.6 ± 1.0 at 3T compare to 2.4 ± 0.4 at 1.5T, and also higher SNR, 68 ± 11 at 3T to 48 ± 7 at 1.5T. This improvement can enhance the visibility of the small blood vessels, which can open new areas to investigate the vascular pathology at the high field strength.

As shown in chapter three, phase encoding orders play a big role in producing high quality images in 3D CE MRA, because of the contrast agent passage through the ROI. Some of these techniques can suppress venous signal to a high degree, but the correct timing for contrast agent arrival should be determined accurately. A new method was introduced to produce the contrast enhancement curve through changing the flip angle during data acquisition in real time. This method was used to compare three different phase encoding techniques. The results indicate that the elliptical technique provides the superior artery-to-vein contrast for an ideal start time, 0.88 comparing to 0.73 for centric encoding technique.

The use of contrast agent for MRA can increase the level of the steady state magnetization because of the T1 shortening of the blood, leading to a higher vascular signal. T1 measurements were performed, using an inversion recovery sequence, on the same sample at 1.5 and 3T field strengths to study the difference in T1 values at different fields (Table 4-1). Three Tesla can provide higher blood to background contrast when the first pass of the contrast agent is used because the higher background T1 values at the higher field lead to minimal background signal.

The 3D CE sequence with centric phase encoding was fully developed and tested on the flow phantom. The test bolus was made to measure the correct timing for the contrast arrival into the ROI. Although contrast enhanced imaging offers new advantages for high resolution MRA at high field strength, the patient study was not possible due to technical difficulties with the neck RF coil and acquisition of appropriate patient safety devices.

5.2. Future Directions:

Three Tesla MRA is only just beginning to be explored. The work here on intracranial TOF MRA could be extended by including magnetization transfer pulses while attempting to avoid the increased patient heating. The 3D TOF sequence could be applied to both head and neck MRA and studies on the diagnostic potential of these techniques could be performed.

From the work performed here, it is clear that 3T MRA has higher SNR, this can be exploited to determine the ultimate limit of spatial resolution at 3T. An advantage of smaller voxel size is further lessening of intravoxel dephasing which can improve the depiction of turbulent flow in diseased blood vessels.

The contrast enhanced technique has been well developed here and awaits patient testing. With the recent addition of a whole body RF coil, essentially all major blood vessels in the body can be examined with the techniques developed here.